Dynamic Cell Model with Cellular Signaling Network and Mechanical Forces for Tissue Pattern Formation

BY

JIELING ZHAO
B.S., Beijing Normal University, 2008

THESIS
Submitted as partial fulfillment of the requirements
for the degree of Doctor of Philosophy in Bioinformatcis
in the Graduate College of the
University of Illinois at Chicago, 2016

Chicago, Illinois

Defense Committee:
Jie Liang, Chair and Advisor
Thomas Royston
Ao Ma
Luisa A. DiPietro, Periodontics
Hammad Naveed, Toyota Technological Institute

To my parents,

Xiaoyun Zhao, and Keyan Yang.

ACKNOWLEDGMENT

I am grateful to my advisor, Dr. Jie Liang, for his kind inspiration, continuous encouragement, and financial support for my study and research. This thesis would not be possible without his patient guidance and unbreakable trust. I am thankful to have him as my mentor and role model. His immense knowledge enabled me to develop an understanding of research and to work on diverse interesting projects. His enthusiasm and motivation allowed me to build critical thinking skills and also help me regain my passions on those difficult days. I could not have imagined having a advisor better than him.

In addition, I would like to thank rest of my thesis committee: Dr. Thomas Royston, Dr. Ao Ma, Dr. Luisa A. DiPietro, and Dr. Hammad Naveed, for their encouragement, insightfull comments, and interests in this project.

I would like to thank lab alumni: Dr. Youfang Cao, Dr. Zheng Ouyang Dr. Joe Dundas, Sema Kachalo, Dr. Hsio-Mei Lu, Dr. Marco Maggioni, Dr. David Jimenez Morales, Dr. Yun Xu, and Dr. Ke Tang. It has been a great pleasure working with you all. Also I would like to thank my fellow colleagues: Gamze Gursoy, Meishan Lin, Wei Tian, Anna Terebus, Alan Perez-Rathke, and Boshen Wang for the stimulating discussions and all the fun we had. My sincere thanks also goes to my friends and all of those who supported me in any respect during the completion of the degree.

Contribution of Authors

Chapter 1 is a literature review that places questions addressed in my dissertation in the broad context of the larger field and highlights the significance of these questions. Chapter 2 represents a published manuscript and another manuscript for both of which I was the first author. Chapter 3 represents a submitted manuscript for which I was the first author. Chapter 4 represents a manuscript for which I was the second author. I designed the method of modeling cell behavior and tissue patterning with dynamic changes in cell shape and mechanics and assisted first author Dr. Youfang Cao to implement the algorithms of modeling intracellular signaling network. I also generated Figure 26 and played a large role in the writing of the manuscript with Dr. Youfang Cao and my research advisor, Dr. Jie Liang. Chapter 5 represents a manuscript for which I was the first author. The second author Guillermina Juan contributed to prepare the cell culture and perform the experiments. She also generated Figure 34a, Figure 35a and c, and Figure 36a.

TABLE OF CONTENTS

TABLE OF CONTENTS (Continued)

CHAPTER **PAGE**

TABLE OF CONTENTS (Continued)

CHAPTER **PAGE**

LIST OF TABLES

LIST OF FIGURES

LIST OF FIGURES (Continued)

LIST OF FIGURES (Continued)

LIST OF FIGURES (Continued)

LIST OF FIGURES (Continued)

LIST OF FIGURES (Continued)

LIST OF FIGURES (Continued)

FIGURE **PAGE**

LIST OF ABBREVIATIONS

dyCelFEM	Dynamic Cellular Finite Element Modeling
ECM	Extracellular Matrix
EGF	Epidermal Growth Factor
EMT	Epithelial-mesenchymal Transition
FA	Focal Adhesion
FEM	Finite Element Method
KGF	Keratinocyte Growth Factor
MMP	Matrix Metalloproteinase
PDGF	Platelet-derived Growth Factor
ROCK	Rho-associated Protein Kinase
TGF-β	Transforming Growth Factor-β

SUMMARY

Cells are the basic functional elements of living bodies. Cell-cell and cell-environment interactions largely maintain and regulate the processes of tissue formation and tissue regeneration, which involve collective cell migration and proliferation at large scale. Understanding the mechanisms behind cellular physiological processes such as embryo development, wound healing, and tumor metastasis requires study of cell-cell and cell-environment interactions, and their effects on cellular behaviors. As many underlying subcellular processes such as the generation of physical forces by cytoskeleton and transmitted mechanical forces through intercellular adhesion are difficult to access through direct experiments, computational cell model is useful for gaining insight into the mechanisms of cellular processes and aid in design of further investigations. A number of computational cell models have been developed to study cellular processes (9; 10; 11; 12; 13; 14; 15; 16; 17; 19; 20). However, all have limitations. They either lack accurate descriptions of cell shapes or cell mechanics, or have limited flexibility in modeling cell movements. These limitations prevent effective modeling of dynamic changes in cell shapes and mechanics in biological processes involving large scale cell migration. Here I develop a novel computational cell model called dyCelFEM. It accounts for detailed changes in cellular shapes and mechanics of individual cells in a large population of interacting cells. In addition, it can model the full range of cell motions, from free movement of individual cells to large scale collective cell migration. Furthermore, the transmission of mechanical forces via intercellular adhesion and its rupture is also modeled. With the intercellular protein signaling networks

embedded in individual cells, biochemical control of cell behaviors can also be modeled. The dyCelFEM model is then employed to study two cellular processes, namely, the wound healing and cell movement on ECM (extracellular matrix). Wound healing is a complex process to repair the injured tissue through the communication and collaboration of multiple different types of cells and multiple growth factors and cytokines. Due to its complexity, the underlying cellular mechanisms, such as how the large scale collective cell motions during wound healing are regulated by different type of signals, are still not fully understood. Here I studied the effects of both biochemical and mechanical cues in regulating human skin wound healing and explored their roles in determining the tissue patterns. The cell movement under the effect of cell-ECM interaction is a process of environment sensing of living cell through cellular interaction. In the past decade, it has been found that cell behaves in response to a variety of physical cues from environment through the cell-ECM adhesions. Here I studied the specific role of the ECM geometry on regulating cell elongation and directing cell migration. The overall findings from this study establishes quantitative biological relevance of biochemical and mechanical effects on wound healing and effect of cell-ECM interaction on cell movement. It leads to a better understanding of the mechanisms behind complex processes of wound healing and cell movement on ECM.

CHAPTER 1

INTRODUCTION

1.1 Cell structure and functions

Cell is the basic functional unit of many living organisms. The spatial organization of many living systems is the consequence of the behavior of individual cell and interaction between cells and between cells and their environment (1). The eukaryotic cell consists of three main parts: the membrane, the nucleus, and the cytoplasm. Cell membrane is the boundary between the cell interior and their outside environment. It is composed of lipid bilayer along with many types of protein complexes responsible for regulating and maintaining mechanical support and chemical gradients between the cytoplasm and the outside environment. These protein complexes include cadherin/catenin protein complex, which forms adherent junctions between cells (2) and integrin/fibronectin protein complex, which forms attachment of focal adhesions between cell and ECM (3). Cell nucleus is the organelle which confines the genetic material of the cell. It mediates the gene expression and DNA translation during the cell cycle to ensure protein synthesis occurs in the cell cytoplasm (4). The cell cytoplasm is the medium within the cell, which occupies the space excluding the cell nucleus. It contains cytoskeleton and other cell organelles such as the Golgi apparatus and mitochondrion. It is the place where most of the cellular activities occur, including energy production, protein synthesis and protein transport (5). The cytoskeleton is the main structure for maintaining the shape of the cell. It

consists of three types of cytoskeletal filaments: actin filaments, microtubules, and intermediate filaments (6). Actin filaments form a network connecting both the networks of microtubules and endoplasmic reticulum. In addition, actin filaments also play important role in generating protrusive force for cell migration through the polymerization of G-actin (7). Actin filaments form a planar unipolar mesh-work through actin polymerization at the plasma membrane and actin depolymerization within the cytoplasm. The cycle of polymerization and depolymerization of actin pushes the plasma membrane forward, which leads to cell migration.

1.2 Physiological process of cellular tissue

Many important physiological processes of living systems such as morphogenesis, wound healing, tumor metastasis, and embryonic development are the dynamic processes characterized by large scale cell motions along with formation of protein matrices secreted by the cells. During the past decade, the advancement in microscopy and micro-fabrication, as well as the ability in quantification of the spatio-temporal pattern of movement of cells within monolayers have showed that both biochemical and mechanical cues in the cellular micro-environment can provide guidance for the cell motion (8). In addition to individual cell motion under the direction of these cues, cells can also sense the presence of their neighbors, and modify their behaviors accordingly (81). However, it is unclear how mechanical and biochemical cues can be processed by a cell to reach a consensus decision that directs the cell behavior. Identifying the contribution of biochemical and mechanical cues and the manner in which they interact with each other to regulate collective cell motions can aid in the development of novel strategies to

modulate specific physiological processes such as accelerated wound healing or retarded tumor metastasis.

1.3 A novel computational model to study dynamics of cellular physiological process

There are advantages in using simple models and approaches to understand complex processes. Computational models can help us to rewrite the large complex biological system which are difficult to analyze through direct experiments into small problems obeying fundamental physical and biological principles with solution calculated numerically and efficiently. Computational models are playing more important roles in the advancement of understanding mechanisms behind cellular physiological processes. These models can be broadly categorized into continuum and discrete models. Continuum models are based on differential equations to model the spatial-temporal changes of protein density in cells, and changes of cell populations in a tissue. In these models, individual cells and interactions are not modeled explicitly (9; 10; 11). Discrete models such as cellular potts model (12; 13), vertex model (14; 15), centric model (16), subcellular element model (17), immersed boundary model (18), and finite element model (19; 20) are based on discretized elementary units to model cell morphology and motility. These models can describe cell shape and intercellular interactions explicitly. However, there are many limitations. Cellular potts model represents cell as a set of lattice sites (21). Any shape change is modeled indirectly using metropolis moves of boundary lattice sites (12), which may require many iterations of energy refinement to ensure such moves are not trapped in local minimum. In addition, the underlying physical forces and cellular mechanics are difficult to recover from

spatial changes of lattice sites. Vertex model describes the changes in cell shape based on minimizing energy under forces acting on cell boundary junctions (14). The mechanical energy of the cell in cell interior is usually not considered or is simplified as a general term controlled by total cell area, without considering the shape of the cell (14). Centric model can only describe the shape of a cell as one or two simple spheres (16). Subcellular element model can describe cell shape in high resolution. However, the distances between intra/intercellular elements are artificially maintained through an arbitrarily imposed Morse potential (17), which is not physically realistic (22). As a result, many iterations of refinement of the potential at local position may be required to eliminate geometric collisions. Immersed boundary model can also describe cell shapes in detail. However, the physical boundary of the cell body may not fully conform to the underneath grid (23), which lead to irregular boundary points in the solution. High cost of iterative refinements of the grid and bilinear interpolations of the solutions have to be carried out to eliminate these irregular boundary points (24). Finite element cell model can describe both cell shape and cell mechanics accurately (25; 26; 19). However, this method permits only limited changes in cell shapes and allows limited flexibility of cell movement, and therefore are restricted to cellular and tissue processes that do not involve free movement of individual cells. Due to these limitations, accurate modeling of physiological processes involving large scale and collective cell migration at detailed cellular level remains a challenging task.

A novel computational cellular model using dynamic finite element method (dyCelFEM) is developed in this thesis. This model has a number of advantages over existing discrete cell models. It can accurately describe the full span of cell movement, from the free movement

of individual cells to large scale collective cell migration. In addition, changes in cell shapes under the control of cell mechanics while in movement are fully accounted for. Furthermore, the transmission of mechanical force regulated by intercellular adhesion and its rupture are also explicitly modeled. As biochemical signals strongly influence cell behavior and tissue patterning (27; 28), intracellular networks of protein signaling are also embedded inside individual cells in our model. Our dyCelFEM model is therefore well suited to study biological processes involving large scale collective cell motions under the regulation of biochemical signals and mechanical forces, with accurate description of cell shapes and cell mechanics. In this thesis, we apply dyCelFEM to study the wound healing process and the cell elongation process on ECM. We briefly describe below how the model is implemented to study these processes.

1.3.1 Effects of biochemical and mechanical cues in re-epithelialization

In this study, I apply the dyCelFEM model to specify the different roles of biochemical signaling and mechanical forces in regulating cell migration during the re-epithelialization process of skin would healing. We focus on the effects of three different guidance mechanisms of cell migration: chemotaxis, chemokinesis, and cohesotaxis. Our simulation correctly reproduces the overall cellular behavior observed in experimental studies, including the physiological timeline of re-epithelialization and the overall patterns of cell proliferation and cell migration. Our results also suggest different roles of biochemical and mechanical cues in re-epithelialization: biochemical cues are better at guiding keratinocytes migration with improved directionality and persistence, while mechanical cues are better at coordinating keratinocytes migration with improved collective movement. In addition, our results show that the decrease

of E-cadherin regulated cell-cell adhesion significantly perturbed the cell-cell coordination and reduced the migration directionality; inhibition of mechanical force transmission through E-cadherin significantly reduced the migration directionality and persistence and prolonged the re-epithelialization process. These findings will be helpful to gain further understanding of the full mechanism of wound healing.

1.3.2 Effects of TGF-β in tissue regeneration

In this study, we apply the DYCELFEM model to simulate the healing process of an excisional wound created *in silico* on the skin. By dynamically tracking behaviors, positions, spatial configurations of cells, and spatial distributions of different molecular mediators over time, we are able to correctly reproduce the formation of granulation tissue and re-epithelialization during wound healing. We then studied the effect of TGF-β on dermal and epidermal pattern formation during wound healing. Combining computational simulations and experimental observations, our results suggest a novel mechanism for the inhibition of keratinocyte proliferation and epidermal re-epithelialization by TGF-β. Specifically, our results suggest that TGF-β can attenuate the strengths of PDGF and KGF signals that fibroblasts and keratinocytes receive by promoting ECM synthesis and deposition in the wound space. In analogy to electrical circuits, the ECM acts as a resistor for PDGF and KGF signals, and the TGF-β act as a potentiometer that can change the resistivity of the resistor, therefore indirectly regulate the signal patterns and cell behavior. This study shows that our method has the potential to facilitate new understanding of the control mechanisms of important multi-cellular processes.

1.3.3 Effects of ECM geometry on cell migration

Focal adhesions play essential role in many cellular behaviors and physiological processes such as cell migration, cell proliferation, wound healing, and tumor invasion. Focal adhesion is also found to be the hub of both protein signaling and mechanical sensing between cell and the ECM. However, the mechanism of how cells sense and respond to the changes in the ECM geometry at subcellular level and how these geometry cues is translated into cellular scale behaviors are not well understood. In this study, we model an *in vitro* experiment study, which investigates the effect of geometric cues of ECM on cell morphological change and migration orientation. We also incorporate viscoelastic properties to our cell model and dynamics of focal adhesion between cell and ECM. Our computational model can quantitatively captures the spatial pattern of cell elongated morphology and oriented migration on ECM-mimicking substrate with increased spacing. Together with the experiment and computational simulations, we suggest that the interaction between the spatial distribution of focal adhesion and cell polarization in protrusion is the key regulator of the morphology and migration of cells in response to geometric cues of the ECM.

CHAPTER 2

CELLULAR DYNAMIC FINITE ELEMENT MODEL

2.1 Introduction

Finite element method (29) has been widely used in the field of biomechanics to study the cellular tissue formation and regeneration processes such as neurulation and epithelial mechanics (26; 19), due to its accurate description of changes in tissue mechanics. However, the majority of current finite element models are only restricted to tissues where cells are required to be connected, disallowing free movement of individual cells. In addition, during the simulation, cells are only allowed restricted scale of motility and tissue is only allowed limited changes in its shape. These limitations prevent the conventional finite element methods from being effectively used to model changes in cellular shapes and mechanics of moving cells in important physiological processes involving large scale collective cell migration and proliferation, including morphogenesis, tumor metastasis, and cancer invasion. To overcome the limitation of conventional finite element method, dynamic finite element methods such as PFEM (particle finite element method (30)) has been developed to extend traditional FEM to study mechanics of materials with more flexibility, enabling the undergoing larger scale cell motility to be modeled. Using the dynamic finite element method, the object domain of the target material (either fluid or solid) is represented as nodes tessellated by triangular mesh. Then the mathematical equations governing the physical rules of the mechanical property of the discretized

domain defined by the mesh are subsequentially solved using standard FEM. With dynamic finite element method, the sub-domain of the object can move freely and even separate from the main domain (30). However, there has no dynamic finite element model developed before to study the cellular process with the specific cell mechanics and geometric and topologic change of cell shape. In this study, we developed the dynamic cellular finite element model (dyCelFEM) (31; 32). It can provide accurate description of the object mechanics as well as the geometric and topologic changes of the shape of modeled cells. It is suitable to simulate physiological processes involving large scale of collective cell motions. The next three chapters describe case studies of physiological processes using dyCelFEM.

2.2 Geometric model of cell

In our model, a two-dimensional cell Ω is defined by its boundary $\partial\Omega$, which is represented by an oriented polygon connecting a set of boundary vertices $V_{\partial\Omega} \equiv \{\boldsymbol{\nu}_i \in \partial\Omega \subset \mathbb{R}^2\}$ (Figure 1a). We denote the location of a vertex $\boldsymbol{\nu}_i$ as $\boldsymbol{x}_i$. The cell boundary $\partial\Omega$ is a closed chain of oriented edges $(\boldsymbol{e}_{1,2}, \boldsymbol{e}_{2,3}, \cdots, \boldsymbol{e}_{n,1})$, where edge $\boldsymbol{e}_{i,i+1}$ connects modulus n consecutive boundary vertices $\boldsymbol{\nu}_i$ and $\boldsymbol{\nu}_{i+1}$ in the counter-clock wise orientation. In this study, a perfectly circular cell has a radius $R_\Omega = 10\ \mu m$, and $n = 20$ vertices are used to define $\partial\Omega$. This gives the default edge length $\boldsymbol{e}_{i,i+1} = 3.14\ \mu m$. We first compute the Delaunay triangulation D_Ω of the cell Ω using only boundary vertices $V_{\partial\Omega}$. We follow the *farthest point sampling* method (33) to test if the radius of circumsphere of any triangle in D_Ω is larger than $|\boldsymbol{e}_\theta| = 3.14\ \mu m$. If so, a new vertex is inserted at the circumcenter of this triangle and D_Ω is updated using the 1-to-3 edge flip and 2-to-2 edge flip, upon examination of all edges in the star of the newly inserted vertex (see (34)

for details). This is repeated until all new triangles have their circumsphere radius shorter than $|\boldsymbol{e}_\theta|$. The cell Ω is therefore tessellated by a set of triangles $\mathsf{T}_\Omega = \{\boldsymbol{\tau}_{\mathsf{i},\mathsf{j},\mathsf{k}}\}$, with vertices i, j and k of a triangle $\boldsymbol{\tau}_{\mathsf{i},\mathsf{j},\mathsf{k}}$ drawn from the set of boundary vertices $\mathsf{V}_{\partial\Omega}$ and the set of newly inserted interior vertices $\mathsf{V}_{\mathrm{Int}\Omega}$ (Figure 1b). The vertices $\mathsf{V}_\Omega = \mathsf{V}_{\partial\Omega} \cup \mathsf{V}_{\mathrm{Int}}$, edges $\mathsf{E}_\Omega = \{\boldsymbol{e}_{\mathsf{i},\mathsf{j}} | \boldsymbol{\nu}_\mathsf{i}, \boldsymbol{\nu}_\mathsf{j} \in \mathsf{V}\}$, and the triangles T_Ω form a simplicial complex K_Ω.

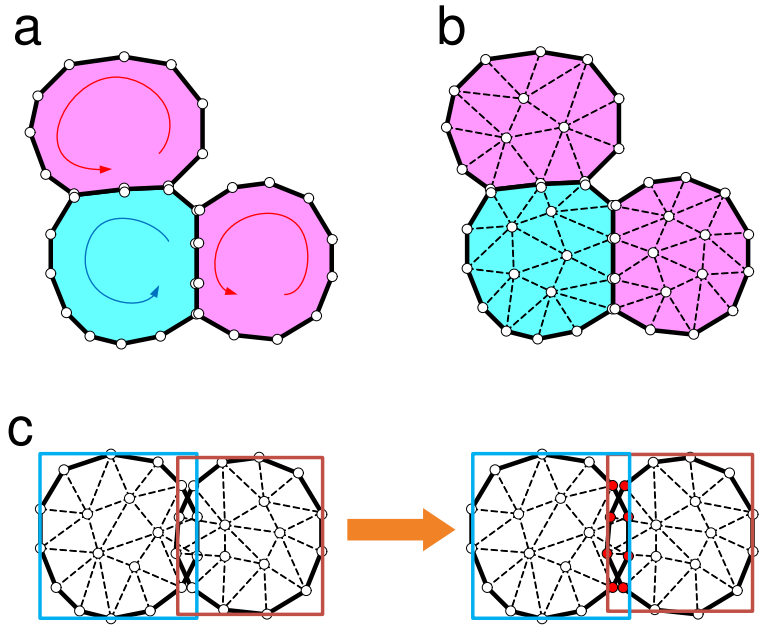

Figure 1. **Discretization and bounding boxes of cells for collision detection.** (a) An example of a toy tissue consisting of three cells. The boundary of each cell is defined by a counter-clock wise oriented polygon containing a number of boundary vertices. (b) Triangular mesh tiling up each cell is generated using the farthest point sampling method based on Delaunay triangulations. (c) Intersection of two bounding boxes of cells fro collision detection: the overlapping surfaces of the two colliding cells are identified upon examining the intersection of the two bounding boxes.

2.3 Deformation energy of elastic cell model

In this thesis, for the studies of wound healing (chapters 3 and 4), we assume that linear elasticity can adequately describe cell deformation under both external and internal forces. For the study of cell elongation on ECM, we assume that linear viscoelasticity can adequately describe the local deformation of the cell under both external and internal forces (see 3.2 and 5.2.2 for reason why these two mechanical properties are chosen for each of these processes). In this section, we first describe how the deformation energy is derived under linear elastic model. And in chapter 5, we will describe how the derivation of deformation energy is adapted under linear viscoelastic model. We use the strain tensor $\boldsymbol{\epsilon}(\mathbf{x})$ to describe the local deformation of the cell at $\mathbf{x}$ (35). The displacement of a vertex at $\mathbf{x}$ is denoted as $\mathbf{u}(\mathbf{x}) = (u_1(\mathbf{x}), u_2(\mathbf{x}))^T \in \mathbb{R}^2$. According to linear elastic theory, the square distance ds^2 between two neighboring points $\mathbf{x}$ and $\mathbf{x}+d\mathbf{x}$ becomes $ds'^2 = |\mathbf{x}'-(\mathbf{x}'+d\mathbf{x}')|^2$ after deformation and is given by the strain tensor $\boldsymbol{\epsilon}(\mathbf{x})$: $ds'^2 = ds^2 + 2\sum_{i,j} \epsilon_{i,j} dx_i dx_j$. Under the assumption of linear elasticity, the strain tensor $\boldsymbol{\epsilon}(\mathbf{x})$ takes the form of $\epsilon_{1,1} = \partial u_1/\partial x_1$, $\epsilon_{2,2} = \partial u_2/\partial x_2$, and $\epsilon_{1,2} = \epsilon_{2,1} = \frac{1}{2}(\partial u_1/\partial x_2 + \partial u_2/\partial x_1)$.

We use the stress tensor $\boldsymbol{\sigma}$ to represent the forces. $\boldsymbol{\sigma}$ is related to the strain tensor $\boldsymbol{\epsilon}$ through the Hooke's law $\boldsymbol{\sigma} = \mathbf{D}\boldsymbol{\epsilon}$, where $\mathbf{D} = \begin{pmatrix} \lambda+2\mu & \lambda & 0 \\ \lambda & \lambda+2\mu & 0 \\ 0 & 0 & \mu \end{pmatrix}$ is determined by two Lam$\acute{e}$ constants λ and μ calculated from the Poisson ratio ν and the Young's modulus E: $\lambda = \frac{E\nu}{(1+\nu)(1-2\nu)}$, $\mu = \frac{E}{2(1+\nu)}$, which characterize the elasticity of the cell.

The strain energy E_Ω associated with the deformation $\mathbf{x} \in \Omega$ is given by $E_\Omega = \frac{1}{2}\int_\Omega \boldsymbol{\epsilon}^T(\mathbf{x}) D \boldsymbol{\epsilon}(\mathbf{x}) d\mathbf{x}$. In addition, the force $\mathbf{f}(\mathbf{x})$, such as the protrusion force driving cell migrate or pressure force driving cell grow and proliferate (see 2.4.1 and 2.4.3 for more details of derivation of these

forces), may also do work on a cell Ω, which can be written as $-\int_\Omega \mathbf{f}(\mathbf{x})\mathbf{u}(\mathbf{x})d\mathbf{x}$. Furthermore, the energy due to the interaction between cell and the environment can be included relatively following previous study as $\frac{Y}{2}\int_\Omega \mathbf{u}(\mathbf{x})^2 d\mathbf{x}$ (36) where Y is a constant coefficient. As the strain tensor $\boldsymbol{\epsilon}(\mathbf{x})$ is related to the displacement vector $\mathbf{u}(\mathbf{x})$ through the relationship of $\boldsymbol{\epsilon}(\mathbf{x}) = \mathbf{B}\mathbf{u}(\mathbf{x})$ (37), where

$$\mathbf{B} = \begin{pmatrix} \partial/\partial x_1 & 0 \\ 0 & \partial/\partial x_2 \\ \partial/\partial x_2 & \partial/\partial x_1 \end{pmatrix}. \tag{2.1}$$

The overall free energy E_Ω of the cell can be written as

$$E_\Omega = \frac{1}{2}\int_\Omega \mathbf{u}(\mathbf{x})^T \mathbf{B}^T \mathbf{D}\mathbf{B}\mathbf{u}(\mathbf{x})d\mathbf{x} + \frac{Y}{2}\int_\Omega \mathbf{u}(\mathbf{x})^2 d\mathbf{x} - \int_\Omega \mathbf{f}(\mathbf{x})^T \mathbf{u}(\mathbf{x})d\mathbf{x}. \tag{2.2}$$

The deformed cell under exerted force reaches its balance state when the strain energy of the cell E_Ω reaches minimum, at which we have $\partial E_\Omega(\mathbf{u})/\partial \mathbf{u} = 0$.

To calculate the displacement $\mathbf{u}(\mathbf{x})$ of a location $\mathbf{x} = (x_1, x_2)$ in a triangular element $\boldsymbol{\tau}_{i,j,k} \in T_\Omega$ from Eqn (Equation 2.2), we applied the stiffness matrix method to $\boldsymbol{\tau}_{i,j,k}$. The displacement vector $\mathbf{u}(\mathbf{x})$ can be interpolated from the displacement vectors of the three vertices $\mathbf{x}_i = (x_{i,1}, x_{i,2})$, $\mathbf{x}_j = (x_{j,1}, x_{j,2})$, and $\mathbf{x}_k = (x_{k,1}, x_{k,2})$ of $\boldsymbol{\tau}_{i,j,k}$ and the barycentric coordinates $\boldsymbol{\lambda} \equiv (\lambda_i(\mathbf{x}), \lambda_j(\mathbf{x}), \lambda_k(\mathbf{x}))$ of $\mathbf{x}$:

$$\mathbf{u}(\mathbf{x}) = \sum_{l\in\{i,j,k\}} \lambda_l(\mathbf{x})\mathbf{u}_l(\mathbf{x}), \tag{2.3}$$

where $\boldsymbol{\lambda}$ is determined by $\boldsymbol{\lambda} = \begin{pmatrix} 1 & 1 & 1 \\ x_{i,1} & x_{j,1} & x_{k,1} \\ x_{i,2} & x_{j,2} & x_{k,2} \end{pmatrix}^{-1} \begin{pmatrix} 1 \\ x_1 \\ x_2 \end{pmatrix}$, which can be rewritten as

$$\boldsymbol{\lambda} = \frac{1}{2|\boldsymbol{\tau}_{i,j,k}|} \begin{pmatrix} a_i & b_i & c_i \\ a_j & b_j & c_j \\ a_k & b_k & c_k \end{pmatrix} \begin{pmatrix} 1 \\ x_1 \\ x_2 \end{pmatrix}, \tag{2.4}$$

where $|\boldsymbol{\tau}_{i,j,k}|$ is the area of the triangle $\boldsymbol{\tau}_{i,j,k}$, $a_i = x_{j,1}x_{k,2} - x_{k,1}x_{j,2}$, $a_j = x_{i,1}x_{k,2} - x_{k,1}x_{i,2}$, $a_k = x_{i,1}x_{j,2} - x_{i,1}x_{j,2}$, $b_i = x_{j,2} - x_{k,2}$, $b_j = x_{k,2} - x_{i,2}$, $b_k = x_{i,2} - x_{j,2}$, $c_i = x_{j,1} - x_{k,1}$, $c_j = x_{k,1} - x_{i,1}$, and $c_k = x_{i,1} - x_{j,1}$. From Eqn (Equation 2.3) and Eqn (Equation 2.4), $\frac{\partial \mathbf{u}(\mathbf{x})}{\partial x_1}$ can be written as

$$\frac{\partial \mathbf{u}(\mathbf{x})}{\partial x_1} = \frac{\partial \sum_{l \in \{i,j,k\}} \lambda_l u_l(\mathbf{x})}{\partial x_1} = \sum_{l \in \{i,j,k\}} \frac{b_l}{2|\tau_{i,j,k}|} u_l(\mathbf{x}).$$

Similarly $\frac{\partial \mathbf{u}(\mathbf{x})}{\partial x_2}$ can be written as

$$\frac{\partial \mathbf{u}(\mathbf{x})}{\partial x_2} = \sum_{l \in \{i,j,k\}} \frac{c_l}{2|\tau_{i,j,k}|} u_l(\mathbf{x}).$$

The strain-displacement matrix $\mathbf{B}_\tau$ for $\boldsymbol{\tau}_{i,j,k}$ corresponds to the continuous version of $\mathbf{B} = \begin{pmatrix} \partial/\partial x_1 & 0 \\ 0 & \partial/\partial x_2 \\ \partial/\partial x_2 & \partial/\partial x_1 \end{pmatrix}$ of Eqn (Equation 2.2) of $\mathbf{u}_\tau = (\mathbf{u}_i, \mathbf{u}_j, \mathbf{u}_k)^T$ takes the form of $\mathbf{B}_\tau = \frac{1}{2|\boldsymbol{\tau}_{i,j,k}|} \begin{pmatrix} b_i & 0 & b_j & 0 & b_k & 0 \\ 0 & c_i & 0 & c_j & 0 & c_k \\ c_i & b_i & c_j & b_j & c_k & b_k \end{pmatrix}$.
The free energy E_τ of $\boldsymbol{\tau}_{i,j,k}$ can be rewritten following Eqn (Equation 2.2) as

$$E_\tau = \frac{1}{2} \int_\tau \mathbf{u}_\tau(\mathbf{x})^T \mathbf{B}_\tau^T \mathbf{D} \mathbf{B}_\tau \mathbf{u}_\tau(\mathbf{x}) d\mathbf{x} + \frac{Y}{2} \int_\tau \mathbf{u}_\tau(\mathbf{x})^2 d\mathbf{x} - \int_\tau \mathbf{f}(\mathbf{x})^T \mathbf{u}_\tau(\mathbf{x}) d\mathbf{x}, \tag{2.5}$$

where $\mathbf{f}(\mathbf{x}) = (\lambda_i \mathbf{f}_i(\mathbf{x}), \lambda_j \mathbf{f}_j(\mathbf{x}), \lambda_k \mathbf{f}_k(\mathbf{x}))$, with $\mathbf{f}_i(\mathbf{x}), \mathbf{f}_j(\mathbf{x}), \mathbf{f}_k(\mathbf{x})$ the external force vectors applied to the three vertices of $\boldsymbol{\tau}_{i,j,k}$.

We can find the solution to the problem of deformation under external forces with the assumption that the free energy of $\boldsymbol{\tau}_{i,j,k}$ reaches its minimum at stationary state, which happens when $\partial E_\tau / \partial \mathbf{u}_\tau(\mathbf{x}) = 0$. After taking the derivative, we can rewrite the equilibrium equation for the element $\tau_{i,j,k}$ as

$$\int_\tau \mathbf{B}_\tau^T \mathbf{D} \mathbf{B}_\tau \mathbf{u}_\tau(\mathbf{x}) d\mathbf{x} + Y \int_\tau \mathbf{u}_\tau(\mathbf{x}) d\mathbf{x} - \int_\tau \mathbf{f}(\mathbf{x})^T d\mathbf{x} = 0. \tag{2.6}$$

Assuming the element $\boldsymbol{\tau}_{i,j,k}$ is of unit thickness t_τ, the element stiffness matrix $\mathbf{K}_\tau$ of $\tau_{i,j,k}$ is

$$\mathbf{K}_\tau \equiv \int_\tau \mathbf{B}_\tau^T \mathbf{D} \mathbf{B}_\tau d\mathbf{x} + Y \int_\tau d\mathbf{x} = t_\tau |\boldsymbol{\tau}_{i,j,k}| \mathbf{B}_\tau^T \mathbf{D} \mathbf{B}_\tau + Y |\boldsymbol{\tau}_{i,j,k}| \mathbf{I},$$

where $\mathbf{I}$ is identity matrix and

$$\mathbf{f}_\tau \equiv \int_\tau \mathbf{f}(\mathbf{x})^T d\mathbf{x} = t_\tau \frac{|\boldsymbol{\tau}_{i,j,k}|}{3} (\mathbf{f}_i, \mathbf{f}_j, \mathbf{f}_k)^T.$$

From Eqn (Equation 2.6), we obtain the linear equation

$$\mathbf{K}_\tau \mathbf{u}_\tau = \mathbf{f}_\tau$$

for element $\boldsymbol{\tau}_{i,j,k}$.

We can then gather the element stiffness matrices of all elements in all cells and assemble them into one global stiffness matrix $\mathbf{K}$. The linear relationship between the concatenated

vector $\mathbf{u}$ of all vertices in the mesh and the external force vector $\mathbf{f}$ on all vertices is then given by:

$$\mathbf{K}\mathbf{u} = \mathbf{f}. \tag{2.7}$$

The behavior of the whole tissue in stationary state at a specific time step then can be obtained by solving this linear equation. For vertex $\boldsymbol{v}_i$ at $\mathbf{x}_i$, its new location is then updated as $\mathbf{x}_i' = \mathbf{x}_i + \mathbf{u}(\boldsymbol{v}_i)$.

2.4 Geometric model of dynamic changes in cell motion

During cell growth, proliferation and migration, the positions of discretized vertices in cells change with time. We treat the internal pressure force driving cell growth and proliferation, and protrusion force driving cell migration as external forces applied onto the tissue system. We discretized these external forces onto the vertices of cells. The displacement vectors of the vertices capturing the dynamic changes of cells can be then obtained by solving Eqn (Equation 2.7). We now discuss how geometric changes are related to forces associated with cell growth, proliferation and cell migration.

2.4.1 Cell growth

To model cell growth, we follow the approach of (38). For the given cell volume increment $\Delta|\Omega|$, we evenly distribute a fraction $\Delta|\Omega_i|$ of $\Delta|\Omega|$ onto cell boundary vertex $\boldsymbol{v}_i$ so $\sum_i \Delta|\Omega_i| = \Delta|\Omega|$ (Figure 2a). This gives the displacement $\mathbf{u}_i = \Delta\boldsymbol{v}_i$ of vertex $\boldsymbol{v}_i$ where $\Delta\boldsymbol{v}_i$ is along the direction of the normal vector of $\boldsymbol{v}_i$:

$$\Delta|\Omega_i| = \frac{1}{2}|\Delta\boldsymbol{v}_i \times (\boldsymbol{e}_{i-1,\,i} + \boldsymbol{e}_{i,\,i+1})|, \tag{2.8}$$

where $\boldsymbol{e}_{i-1,i}$ and $\boldsymbol{e}_{i,i+1}$ are edges connected to $\boldsymbol{v}_i$. The internal pressure force $\mathbf{f}_i$ exerted on vertex $\boldsymbol{v}_i$ necessary for cell growth with the increment volume of $\Delta|\Omega_i|$ is calculated as

$$\mathbf{f}_i = \mathbf{K}_i \mathbf{u}_i, \tag{2.9}$$

where $\mathbf{K}_i$ is the sub-matrix of the stiffness matrix $\mathbf{K}$ involving vertex $\boldsymbol{v}_i$.

2.4.2 Cell proliferation

Cell proliferation occurs when the volume of the mother cell Ω is doubled. We divide Ω into two daughter cells Ω_1 and Ω_2 by adding a set of paired vertices along the shortest axis of Ω.

2.4.3 Cell migration

To model cell migration, we distribute the protrusion forces onto the vertices on the leading edges. Here leading edges are defined as edges whose outward normal $\boldsymbol{n}$ and the unit vector of migration direction $\boldsymbol{\nu}$ has positive inner product: $\boldsymbol{n} \cdot \boldsymbol{\nu} > 0$. For each boundary vertex $\boldsymbol{v}_i$ on a leading edge, the protrusion force driving $\boldsymbol{v}_i$ to migrate is calculated as

$$\mathbf{f}_i = \frac{1}{2} f_{af}(|\boldsymbol{e}_{i-1,i}| + |\boldsymbol{e}_{i,i+1}|)(\boldsymbol{n} \cdot \boldsymbol{\nu})\boldsymbol{\nu},$$

where f_{af} is the parameter of protrusion force per unit length per time step, $\boldsymbol{e}_{i-1,i}$ and $\boldsymbol{e}_{i,i+1}$ are edges connected to $\boldsymbol{v}_i$ (Figure 2b).

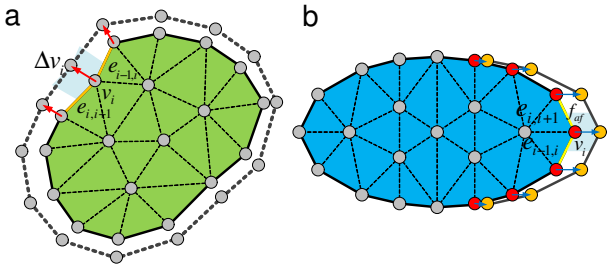

Figure 2. **Model of cell proliferation and migration.** (a) Cell proliferation from time step t to $t + \Delta t$. The incremental cell volume $\Delta|\Omega|$ is evenly distributed to individual boundary vertex $\boldsymbol{\nu}_i$ as $\Delta|\Omega_i|$ (in cyan) satisfying $\sum_i \Delta|\Omega_i| = \Delta|\Omega|$. $\Delta\boldsymbol{\nu}_i$ is the displacement vector of $\boldsymbol{\nu}_i$ such that after proliferation. (b) Cell migration from time step t to $t + 1$. The protrusion force driving cell migration due to actin polymerization on each boundary vertex $\boldsymbol{\nu}_i$ on leading edge is calculated following ref. f_{af} is the parameter of protrusion force per unit length per time step.

2.4.4 Mechanical cell-cell interaction and cell adhesions in cell migration

The formation and rupture of cell-cell adhesions are explicitly considered in our model. When a cell migrates, the protrusion force on a leading edge produces contraction force in the adhesion complex formed with its contacting cells against the adhesions between them through the function of myosin II (39; 40). Here we assume that the contraction force results from cell elasticity. Once the contraction exerted on an adhesive linkage between two vertices on two contacting cells surpasses a threshold f_θ, the attachment of adhesiveness between these vertices is removed. In our model, there is a prefixed cell thickness $t_\tau = 1\ \mu m$. Parameters associated with cell surface area in 3D are then converted to be associated with cell boundary length in

2D by multiplying the value of cell thickness. For example, the rupture stress of E-cadherin mediated cell-cell adhesion changes from 4.1 $nN/\mu m^2$ (41) to 4.1 $nN/\mu m$.

In our finite element model, we can compute the contraction forces at each vertex in the contacting surface of a cell in response to cell motion. For vertex $\boldsymbol{v}_{1,i}$ from cell Ω_1 on the contacting surface with cell Ω_2, we can recover the contraction force vector using the stiffness matrix associated with $\boldsymbol{v}_{1,i}$ (Figure 3a):

$$\mathbf{f}_{1,i} = \mathbf{K}_{1,i}\mathbf{u}_{1,i}, \tag{2.10}$$

where $\mathbf{K}_{1,i}$ is the sub-stiffness matrix associated with vertex $\boldsymbol{v}_{1,i}$, $\mathbf{u}_{1,i}$ is the displacement vector of $\boldsymbol{v}_{1,i}$. For vertex $\boldsymbol{v}_{2,j}$ on cell Ω_2 attached to Ω_1, we recover the contraction force similarly. If $\max(|\mathbf{f}_{1,i}\mathbf{n}_{1,i}|, |\mathbf{f}_{2,j}\mathbf{n}_{2,j}|) > f_\theta \cdot l$ where $\mathbf{n}_{1,i}$ and $\mathbf{n}_{2,j}$ are normal vector of $\boldsymbol{v}_{1,i}$ and $\boldsymbol{v}_{2,j}$, we eliminate the attachment between vertices $\boldsymbol{v}_{1,i}$ and $\boldsymbol{v}_{2,j}$ (Figure 3b). Here f_θ is rupture force per unit length, l is the half-length of the shared edge(s) between $\boldsymbol{v}_{1,i}$ and $\boldsymbol{v}_{2,j}$. When both $\boldsymbol{e}_{i-1,i}$ and $\boldsymbol{e}_{i,i+1}$ are in the contacting surface, $l = (|\boldsymbol{e}_{i-1,i}| + |\boldsymbol{e}_{i,i+1}|)/2$; when only $\boldsymbol{e}_{i-1,i}$ or only $\boldsymbol{e}_{i,i+1}$ is in the contacting surface, $l = |\boldsymbol{e}_{i-1,i}|/2$ and $l = |\boldsymbol{e}_{i,i+1}|/2$, respectively.

2.4.5 Geometric collision of cells and its resolution

It is important to detect collision when the bodies of two cells start to overlap and to compute the contacting surface of cells properly.

Cell collision detection. We use the technique of Bounded Deformation Tree (BD-Tree) to identify potential collision between a pair of cells (42). Each node of the BD-Tree represents

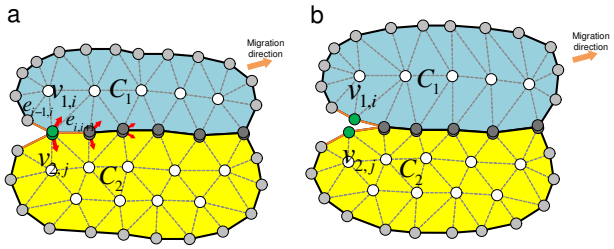

Figure 3. **Model of cell adhesion.** (a) Contraction forces resulting from cell elasticity are generated in response to protrusion force on leading edge. (b) The attached vertices from two contacting cells are separated if the generated contraction force is larger than the threshold of adhesion rupture force.

a bounding box that encloses a group of cells. The root node, n_{root}, of the BD-Tree contains all cells. A node n_i below the root level in the BD-Tree contains a group of neighboring cells according to their distances to each other. This group of cells are then divided into two sub-groups, each containing roughly half of the size of the group of cells in n_i. These two sub-groups of cells are then assigned to the two children nodes of n_i at the next level. The division is terminated until only one individual cell is left, which is then assigned to a leaf node, n_l, at the bottom level of the BD-Tree. For each cell, we use its bounding box to identify potentially colliding cells. We start at the root of the BD-Tree and examine if box-intersection occurs at the next level. This is repeated until we have reached the leaf nodes and identified all potentially colliding cell pairs.

Resolving cell collision. Once a pair of potentially colliding cells Ω_1 and Ω_2 are identified, axis-aligned bounding boxes (43) are generated, and a 4-level quad-tree data structure is

constructed to represent each cell. The locations of edge intersections between the two cells are then identified by testing $(n_1-1)\times(n_2-1)$ pairs of edges, with n_1 and n_2 the number of vertices of Ω_1 and Ω_2 inside the aligned bounding boxes, respectively. There are two intersecting edge-pairs, with the fractions of the overlapping cell boundaries $\partial\Omega_1\cap\partial\Omega_2$ between them (Figure 1c). Once the overlapping portions are identified, they are repaired using the *Cell-merge* primitive described below, which generates a new contacting surface between previously colliding cells. This initiated contacting surface is subject to relaxation from the elasticity of Ω_1 and Ω_2 in the next time step.

2.5 Primitives for topologic and geometric changes

There are five Primitives we use to model topologic and geometric changes during cell growth, proliferation and migration.

- P1. *Cell-separation*: When a pair of attachment vertices on the contacting surfaces of two cells express contraction force beyond the threshold f_θ, we remove the attachment between them and they become free to move apart (Figure 4a).
- P2. *Cell-merge*: When two cells in collision are identified, the spatial locations of vertices in each cell in the intersecting surfaces are updated so the overlaps between cells are repaired. The new contacting surfaces from the two cells are defined by a set of vertices where both surfaces are attached. The attachment vertices from the two cells are paired as adhesive vertices sharing the same coordinates (Figure 4b; see 2.5.1 for more details).
- P3. *Edge-subdivision*: When an edge becomes longer than a predefined threshold of $2|\boldsymbol{e}_\theta|$, we subdivide this edge by adding a new vertex at its midpoint (Figure 4c).

- P4. *Edge-simplification*: When an edge becomes shorter than a predefined threshold of $|e_\theta|/2$, we remove this edge, its preceding edge, and its succeeding edge. We then directly connect the preceding and the succeeding vertices with a new edge (Figure 4d).
- P5. *Sliver-removal*: When a skinny triangle with an angle smaller than a predefined threshold $\theta_S = 19^\circ$ (44) appears, the high aspect ratio of its longest edge and its shortest edge is detrimental to the numerical stability of finite element calculation (44). We therefore remove this skinny triangle, two of its edges, and one of its vertices. A new edge is then added to connect the two remaining vertices (Figure 4e; see 2.5.2 for details).

2.5.1 Details of the *Cell-merge* primitive

For a potentially colliding pair of cells Ω_1 and Ω_2, the sets of candidates of colliding vertices V_1 from Ω_1 and V_2 from the Ω_2 are collected from quad-tree constructed using the AABB method (43). Let $|V_1| = n_1$ and $|V_2| = n_2$. The locations of edge intersections between the two cells are then identified by testing $(n_1 - 1) \times (n_2 - 1)$ pairs of edges connecting vertices in V_1 and V_2, respectively. For a pair of crossing-edges $e_{i,i+1}$ and $e_{j,j+1}$, we select the pair of vertices, one from (v_i, v_{i+1}) and another from (v_j, v_{j+1}) that has the shortest distance to the crossing point. We update the coordinates of these two vertices using their averaged position, denoted as x_1 (Figure 5a). We repeat this for the other pair of crossing-edges and obtain the other averaged position x_2. Assuming $n_1 > n_2$, we replace the coordinates of the remaining $(n_1 - 2)$ vertices in V_1 with $(n_1 - 2)$ coordinates equally distributed between x_1 and x_2. We then add $n_1 - n_2$ vertices to V_2 so V_2 also has n_1 vertices. These $n_1 - 2$ vertices for Ω_2 are assigned with the same equally distributed $n_1 - 2$ coordinates as those of V_1 (Figure 5a).

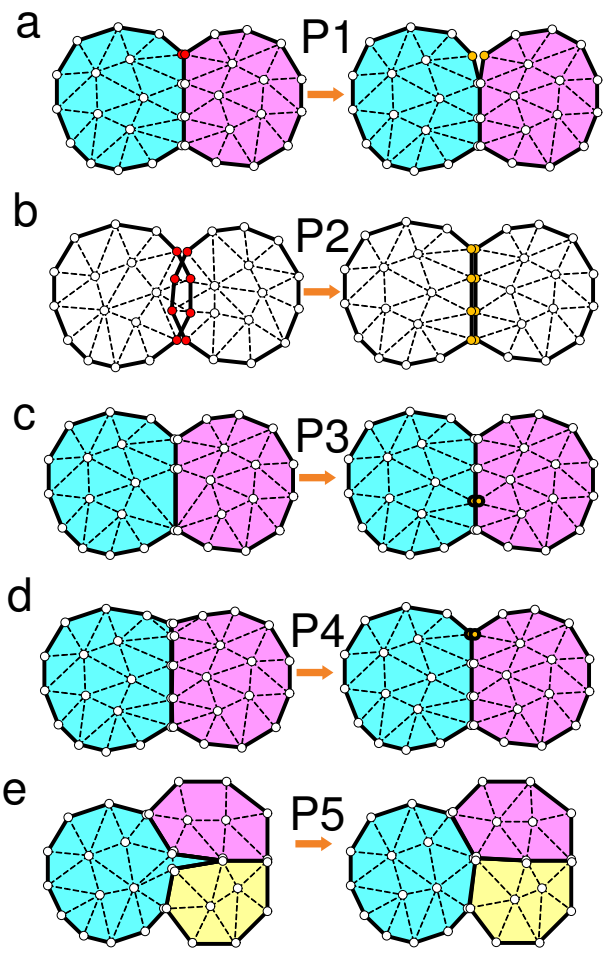

Figure 4. **Primitives for cell geometric changes.** (a) P1. *Cell-separation*: Previously attached vertices on the contacting surfaces of two different cells are separated from each other. (b) P2. *Cell-merge*: Collision between two cells is detected and repaired by constructing the initial contacting surface. (c) P3. *Edge-subdivision*: When an edge becomes longer than a predefined threshold of $2|\boldsymbol{e}_0|$, it is subdivided by adding a new vertex at the midpoint. (d) P4. *Edge-simplification*: when an edge becomes shorter than a predefined threshold of $|\boldsymbol{e}_0|/2$, it is removed from the cell. (e) P5. *Sliver-removal*: When a skinny triangle with an angle smaller than a predefined threshold $\theta_S = 19^\circ$ appears, the high aspect ratio of the longest edge and the shortest edge is detrimental to the numerical stability of finite element calculation. We therefore remove this skinny triangle, two of its edges, and one of its vertices. A new edge is then added to connect the two remaining vertices.

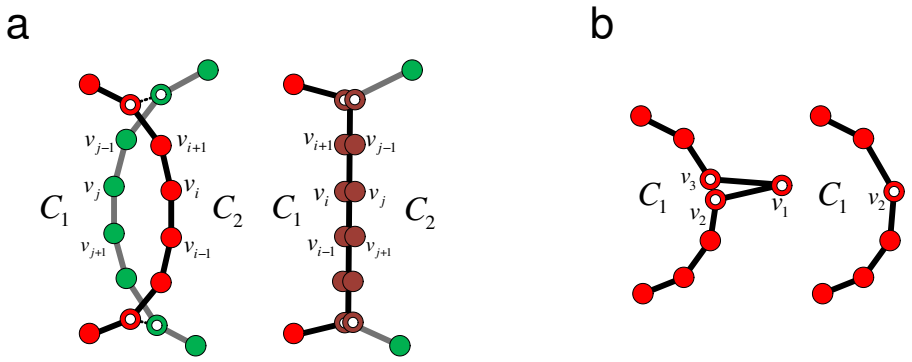

Figure 5. **The primitives of *Cell-merge* and *Sliver-removal*.**: (a) Cell-merge: cell vertices detected to be in collision are aligned and repaired. (b). Sliver-removal: vertices associated with skinny angle are removed from the model.

2.5.2 Details of the *Sliver-removal* primitive

Finite element with high aspect ratio, namely, the ratio between the largest and smallest dimension of the element, introduces numerical instability (44). If a skinny triangle has an angle formed by vertices v_1, v_2 and $v_3 < 19°$ (corresponding to an aspect ration of > 3) (Figure 5b), we remove vertices v_1 and v_3 from the triangulation and update the coordinates of v_2 to the averaged position of v_2 and v_3.

2.5.3 Compatibility of geometric changes with the vertex model

In vertex cell model, three elementary moves can exhaust all possible topological changes. These are recombination (T1), disappearance (T2), and adhesion (T3) (14). These three moves can be realized using primitives P1–P5 described in this study (Figure 6a–Figure 6c). In addition to topological changes of T1–T3, we introduced one new change called *Cell-separation* (P1), which separates one pair of contacting cells (Figure 6d).

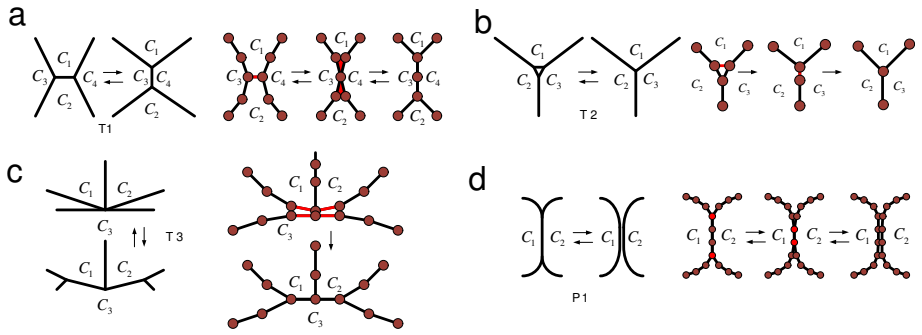

Figure 6. **Combination of primitives in this study can realize all cell topologic changes in vertex cell model and introduction of a new type of cell topologic change.** (a) Recombination (T1) move is realized by one *edge-simplification* primitive of the edge connecting C_1 and C_2, followed by two *sliver-removal* primitives for C_1 and C_2 each. (b) Disappearance (T2) move is realized by three *edge-simplification* primitives for C_1, C_2, and C_3 each. (c) Adhesion (T3) move is realized by two *cell-merge* primitives for C_1-C_3 pair and C_2-C_3 pair. (d) A new type of topological change called *Cell-separation* (P1) which separates one pair of cells is introduced in our model. One *cell-separation* primitive between neighboring cells C_1 and C_2 is shown.

2.6 Implementation

The implemented software of DYCELFEM (Figure 7) is a computationally efficient user-friendly and easily deployable software of simulating cellular tissue problems involving large scale of cell motions. It provides a general and powerful tool with the workflow which can be performed easily in a completely automated way using predefined process (see more details in A.2).

2.7 Conclusion

As there is growing interests in studying tissue physiological processes such as wound healing, cancer invasion, efficient computational models of cells and tissues will play important

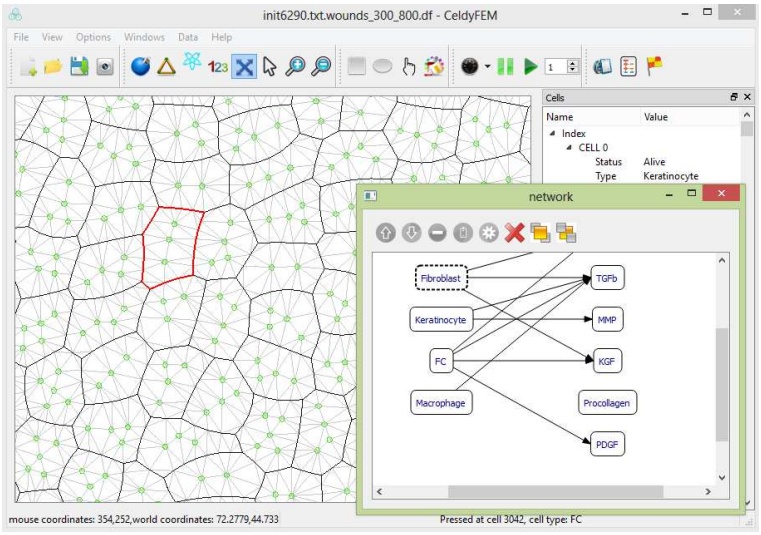

Figure 7. **Demo of dyCelFEM.** dyCelFEM provides a graphical user interface for the specification and simulation of cellular tissue phenomenas. The main window shows the data visualization of the geometry of the cellular tissue. Each cell is represented as triangular mesh. The cell behavior and intracellular signaling network can be predefined in another user interface window interactively.

roles. However, current cell models have limitations. They either lack accurate descriptions of cell shapes (54; 10; 11; 16) and cell mechanics (21; 12; 13; 17; 14), or have limited flexibility in modeling cell movement (25; 26; 19; 20). These limitations prevent effective modeling of dynamic changes in cell shapes and mechanics in biological processes involving large scale cell migration. In this study, the dyCelFEM model is developed. It accounts for detailed changes in cellular shapes and mechanics of a large population of interacting cells. In addition, it can model the full range of cell motion, from free movement of individual cells to large scale of collective cell migration. Furthermore, the transmission of mechanical forces via intercellular adhesion and its rupture is also modeled. The intracellular protein signaling networks could also

be embedded in individual cells to control of cell behaviors (see details of embedding signaling network in individual cell in the following three chapters). Overall, the dyCelFEM model is well-suited to study biological processes where migrating cells with dynamic changes in shape and mechanics at large scale are involved.

CHAPTER 3

THE EFFECTS OF BIOCHEMICAL AND MECHANICAL CUES ON CELL MOTION DURING RE-EPITHELIALIZATION

3.1 Introduction

To restore skin integrity rapidly and effectively after injury, keratinocytes are activated shortly upon the growth factors released from the wound site during the re-epithelialization process (46). Growth factors such as keratinocyte growth factor (KGF) and epidermal growth factor (EGF) promote the proliferation and migration of keratinocytes (27; 28). As keratinocytes at the wound boundary are actively migrating towards the wound bed, keratinocytes behind them proliferate to supply new cells to the moving sheets of cells at the wound edge (47).

In addition to the control of growth factor signaling, mechanical forces at the wound site also exert profound influences on cell behavior and tissue patterning. Cyclical mechanical stretch is found to increase DNA synthesis and cell division in human keratinocytes (48). Cells in the connective tissue of the wound bed actively create tension to draw the wound edges together (49). These observations suggested that cells can sense the changes in mechanical forces and transform them into physiological responses. However, the exact roles of biochemical and mechanical cues in guiding cell migration and in influencing cell proliferation during wound healing are still unclear.

Understanding the detailed effects of cellular mechanics during wound healing is challenging. Mechanical properties such as physical forces generated from cytoskeleton (50), mechanical stress exerted at cell-cell junctions (51), and mechanical force transmission from cell to cell are not easy to access through direct measurements of experiments (52). Little is known about how mechanical cues affect and regulate the collective cell migration during re-epithelialization.

We can benefit from applying simple approaches to understand complex processes. Computational models can help us to simplify the large complex system into small problems following fundamentally physical and biological rules and solve them numerically. Computational models are continuously evolving as they play more important roles in the advancement of understanding cell mechanics. In the past decade, computational models have been developed to aid in studying the roles of the machinery of mechano-driven cell migration during wound healing. Using a vertex model, Nagai, *et al.* explored the roles of cell-basal-lamina adhesion in wound closure (14); Brugues, *et al.* studied the wound closure through cell-substrate compressing force (50). Hutson, *et al.* used a finite element model to study cell-level epithelial mechanics in tissue with punched wound (19). Vitorino, *et al.* used a vertex model to show how different steering terms maintain the endothelial sheet migration (15). Monine, *et al.* used a hybrid model to study the effects of intracellular signaling on cell adhesion and migration during wound healing (53). Xu, *et al.* used a cellular potts model to study the clot formation in the blood vessel by considering the vortical flow generated by the clot (13). Vermolen, *et al.* used a semi-stochastic model to study the contractures in burns and cyclic loading (20); Basan, *et al.* used a particle-based model to investigate the relationship between cellular motility force and

tissue flow in wound healing (16). Ziraldo, *et al.* used an agent-based model to study the relationship between pressure and ulcer formation during diabetic foot ulcer wound healing (54). Lee, *et al.* used a model of moving boundary node to show that wound healing might not need biochemical signaling (10). Arciero, *et al.* used a continuum model to explore the relationship between enterocyte contraction and cell layer motion during wound healing (9). Cochet, *et al.* used a continuum model to study the role of border force in wound closure (11). Although these studies have revealed important insight into the influence of mechanical forces on wound healing, there are a number of limitations: the wound size modeled is unrealistically small (*e.g.*, only around 20 cells compared to the size visible to the naked eye) (14; 19; 50); cells are represented as simple spheres (15; 53; 16). These models neglect the facts that migrating cells dynamically adapts their shapes (55); direct cell-cell interaction, the basis of the intercellular mechanical transmission, is often not considered (54; 10; 9; 11; 20).

To gain further understanding of the influence of mechanical interactions such as intercellular adhesions and transmission of mechanical forces on the collective migration of cells during re-epithelialization, it is important to take into account changes in cell shapes, in mechanical interaction, and in force transmissions. However, to study these dynamic changes in a population of large number of cells during re-epithelialization is challenging for existed computational models as such dynamic changes have not been considered by previous computational studies.

In this study, we apply the dyCelFEM model to investigate the effects of biochemical and mechanical cues on migration and proliferation of a population of cells during re-epithelialization. Furthermore, we also apply dyCelFEM to study the roles of E-cadherin

regulated cell-cell adhesion on collective cell migration during re-epithelialization. The advancement of dyCelFEM model in studying the biochemical and mechanical signals within collective cell migration during re-epithelialization includes: First, it describes the cell-cell adhesions with more details as polylines (curved edges) but not as monoline (straight-edge). A recent theoretical study (56) has demonstrated that monoline cell model affects the cell motion in cell engulfment and cell invasion due to restricted cell deformation modes while these restriction are not faced by using polyline cell model. Considering that a moving cell often dynamically changes its adhesive structures during migration (55), it is more appropriate to use polyline cell model but not monoline cell model (15; 16; 50) to study the re-epithelialization process. Second, it belongs to the group of finite element cell models (57; 58; 59; 26; 19; 60; 50) which provides realistic descriptions of cell shapes and mechanics. But these finite element method based model focused more on simulating tissue dynamics with small scale of geometric changes. The wound size of re-epithelialization studied by these models is relatively at the same magnitude of the cell diameter (19; 50). Re-epithelialization achieved in these cases are mainly through the line tension at the wound boundary. dyCelFEM model follows the scheme of particle finite element method (30) which can model individual cell moving freely or separate from the main analysis tissue domain. This feature make it more suitable to model re-epithelialization with large wound size which requires large scale of dynamic cell migration and proliferation to achieve wound closure.

Our results suggest biochemical and mechanical cues play different roles in guiding migration of keratinocyte during re-epithelialization. The influence of biochemical cues are restricted

to areas close to the wound bed, while mechanical cues influence the skin tissue globally. Furthermore, biochemical cues are better at guiding keratinocyte migration with improved directionality and persistence, while mechanical cues are better at coordinating keratinocyte migration, with improved collective cell migration so keratinocyte can follow their moving neighbors efficiently towards the wound bed. In addition, our results show that the decrease of E-cadherin regulated cell-cell adhesion significantly perturbed the cell-cell coordination and reduced the migration directionality; inhibition of mechanical force transmission through E-cadherin significantly reduced the migration directionality and persistence and prolonged the re-epithelialization process. These findings will help us to gain understanding of the full mechanism of wound healing under regulation of intercellular mechanical forces through E-cadherin. These findings will help us to gain understanding of the full mechanism of wound healing.

3.2 Re-epithelialization model

We model the re-epithelialization process of the top layer of skin by simulating the behavior of keratinocytes and wound elements (Figure 8a). Here the wound elements include implicitly both fibrin clots and fibroblasts underneath the clot surface, with its elastic properties determined mostly by the fibrin clot, as it is the major component of the wound site (61). Both keratinocyte and wound element are discretized by triangular meshes. Parameters of the elastic properties of keratinocytes and wound element are taken from previous experimental and computational studies (62; 63; 61) (see Table II for the parameter values).

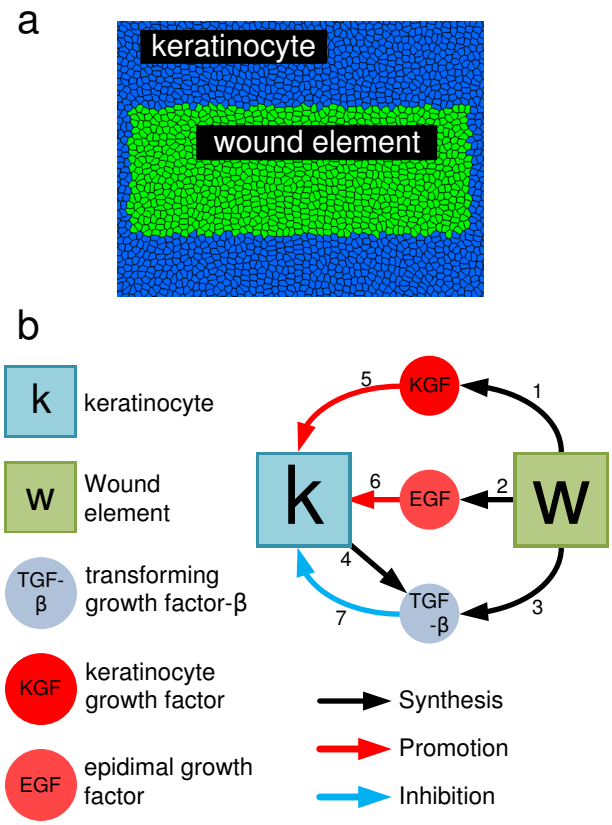

Figure 8. **Tissue model and inter-cellular signaling network embedded in each cell.** (a) Top view of the skin wound tissue. Blue: Keratinocytes; Green: Wound element units for both fibrin clots and fibroblasts. (b) Schematic of the intracellular signaling network. The synthesis and regulation relationship between the cell elements and the growth factors are represented by arrows. See Table I for more details.

TABLE I

Relationships between cells and growth factors in our model. Details of each branch of the schematic diagram of the intracellular paracrine signaling network in our model are given, including the relevant references.

Species	Acts on	Activity	Branch number	Ref.
wound	KGF	Synthesis	1	(174)
	EGF	Synthesis	2	(175)
	TGF-β	Synthesis	3	(28)
keratinocyte	TGF-β	Synthesis	4	(28)
KGF	keratinocyte	Promotes proliferation	5	(28; 27)
EGF	keratinocyte	Promotes proliferation and migration	6	(28; 27)
TGF-β	keratinocyte	Inhibits proliferation	7	(28)

3.2.1 Linear elastic model for deformation energy

Following previous study (171), we assume that linear elasticity can adequately describe cell deformation under both external and internal forces during a time interval. Here we further show that why linear viscoelastic is unnecessary. A model of linear viscoelasticity can be expressed as a Prony series expansion of the stress relaxation as a function of time step Δt (172)

$$E(\Delta t) = E_\infty + \sum_{j=1}^{N} E_j e^{-\frac{\Delta t}{\tau_j}},$$

where E_∞ is the long-term elastic modulus, E_j is the elastic coefficient of viscoelastic element j among the total N elements, $\tau_j = \eta_j / E_\infty$ is the relaxation time of the element j, η_j is the

viscous coefficient of element j. The value of τ_j is usually 1 to 10 seconds (173). In our wound healing model, the time step Δt is fixed as 30 minutes. Therefore, the term $\sum_{j=1}^{N} E_j e^{-\frac{\Delta t}{\tau_j}}$ can be treated as zero. Hence the effect of viscosity can be neglected. That is, the stress in our wound healing model in each time step of 30 minutes is only related to the long term elastic coefficient of the cell. We can therefore assume that linear elasticity is adequate in describing cell deformation in our wound healing model.

3.2.2 Inter-cellular signaling network

Upon the initiation of the re-epithelialization process, keratinocytes at the wound edge are stimulated by EGF and KGF, and begin to proliferate and migrate into the wound site (28; 27). This process is known to be controlled by an intracellular signaling network. The network in our model is taken from the model of Menon *et al.* (64). There are three growth factors in this network, namely, keratinocyte growth factor (KGF), epidermal growth factor (EGF), and the transforming growth factor-β (TGF-β). These growth factors are considered to be the most important growth factors for the re-epithelialization process (28). Overall, there are two types of cells, three types of growth factors, and seven relationships between them in our signaling network (Figure 8b).

3.2.3 Diffusion, synthesis, and degradation of growth factors

Following the model of Menon *et al.* (64), the change in local concentration $\mathbf{y}_i$ of a growth factor i is determined by its diffusion, the synthesis reaction, and the degradation reaction.

$$\frac{\partial \mathbf{y}_i}{\partial t} = D_i \Delta \mathbf{y}_i + \lambda_{s,i} - \lambda_{d,i} \mathbf{y}_i, \tag{3.1}$$

where D_i is the diffusion coefficient, $\lambda_{s,i}$ is the synthesis rate of i and $\lambda_{d,i}$ is the degradation rate of i. See Table II for parameter values. In our model, diffusion of each growth factor in the tissue is modeled with the assumption that cells are compartments with well-mixed growth factors. We have the following diffusion equation:

$$\frac{d\mathbf{x}(s,t)}{dt} = \mathbf{D}\Delta\mathbf{x}_k(s,t), \tag{3.2}$$

where s is the spatial coordinates, $\mathbf{x}(s,t)$ is the concentration vector of different growth factors at s, and $\mathbf{D}$ is the vector of diffusion coefficients of growth factors.

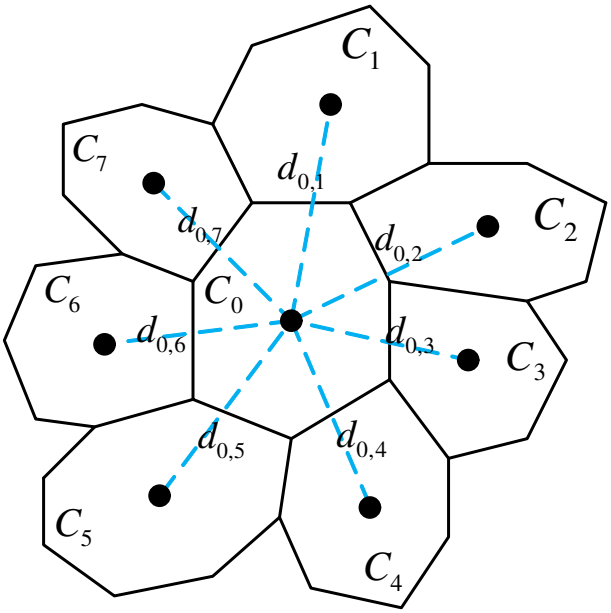

Figure 9. **Diffusion of growth factors through in tissue.** Diffusion of each growth factor in tissue is modeled using cells as elements of homogeneous concentration, and the distance $d_{i,j}$ between centers of two neighboring cells as the diffusion distance.

We then discretize Eqn (Equation 3.2) by cell elements as shown in Figure 9:

$$\frac{d\mathbf{x}(i,t)}{dt} = \mathbf{D} \sum_{j,\, C_i \bigcap C_j \neq \emptyset} \frac{\mathbf{x}(j,t) - \mathbf{x}(i,t)}{d_{i,j}^2}, \tag{3.3}$$

where $\mathbf{x}(i,t)$ is the state vector of growth factor concentrations in cell i at time t, $d_{i,j}$ is the center-to-center distance between cell i and a neighboring cell j. Eqn (Equation 3.3) can be expressed equivalently for growth factor k in cell i as:

$$\frac{dx_k(i,t)}{dt} = \sum_{j, C_i \bigcap C_j \neq \emptyset} A_{k,i,j} x_k(j,t), \tag{3.4}$$

where $A_{k,i,j} = \frac{D_k}{d_{i,j}^2}$ for all $i \neq j$, and $A_{k,i,j} = -\sum_{i,\, C_i \bigcap C_j \neq \emptyset} \frac{D_k}{d_{i,j}^2}$ for $i = j$, with D_k being the diffusion coefficient of growth factor k. This can be re-written in the matrix form as

$$\frac{d\mathbf{x}_k(t)}{dt} = \mathbf{A}_k \mathbf{x}_k(t), \tag{3.5}$$

where $\mathbf{x}_k(t)$ is the concatenated vector of $x_k(i,t)$ for each cell i, $\mathbf{A}_k$ is the matrix whose element is $A_{k,j,i}$. The vector of growth factor concentration in each cell i, namely, $\mathbf{x}(i,t)$ is then updated by solving Eqn (Equation 3.5).

Stochastic model of cellular behavior of keratinocytes. In our model, keratinocytes can proliferate, migrate, apoptosize, or become quiescent. The probability π_i of each of these four types of behavior is determined by the concentrations of the growth factors (65):

$$\pi_i = \frac{B_i}{\sum_k B_k}, \tag{3.6}$$

where $B_i = \alpha_i \frac{\prod_j (1+\beta_j^i d_{s_j})}{\prod_k (1+\beta_k^i d_{s_k})}$, with the index $i = 1, 2, 3,$ and 4 representing proliferation, migration, apoptosis and quiescence, respectively. Here α_i is the scaling factor for the i-th behavior, β_j^i is the coefficient for the effects of growth factors j on type i behavior (see Table III for coefficient values). Growth factors with activating effects appear in the numerator, and growth factors with inhibitive effects appear in the denominator (64). $d_{s_{j,k}}$ are the concentrations of corresponding growth factors. The probability of type-i behavior of a keratinocyte at a particular time instance is then sampled according to the probability of π_i.

3.2.4 Cell growth

A cell accumulates proteins and other molecules and grows during one cell cycle. It then divides into two daughter cells (1). The duration of the cell cycle is cell-type specific, but is also influenced by growth factors such as KGF and EGF (66; 67). We follow ref (68) to regard cell growth as a process driven by the increase in interstitial fluid pressure resulting from the accumulation of soluble material inside the cell body. In our model, the interstitial fluid pressure is simplified as the internal pressure due to the accumulation of mass within the cell body accompanying the incremental changes in cell volume according to the elasticity of

the cell (68). The growth rate r_Ω of a cell Ω, namely, its volume increment per unit time, is modeled as (69; 70; 71):

$$r_\Omega = \frac{|\Omega|(1 + k_{KGF} \log(y_{KGF}))(1 + k_{EGF} \log(y_{EGF}))}{\Delta T_\Omega}, \tag{3.7}$$

where $|\Omega|$ is the volume of the cell before growth, ΔT_Ω the time duration of a full cell cycle of cell Ω, k_{KGF} and k_{EGF} are coefficients, y_{KGF} and y_{EGF} are the concentrations of KGF and EGF, respectively. For cell Ω growing from time t to $t + \Delta t$, the incremental volume $\Delta|\Omega|$ is calculated as $\Delta|\Omega| = r_\Omega \Delta t$.

3.2.5 Cell proliferation

Once the volume of cell Ω is doubled, we add a set of vertices along the shortest diagonal of Ω to divide it into two daughter cells.

3.2.6 Cell migration

When a cell migrates, actin filaments at the cell periphery polymerize to produce protrusion force that push the cell edges outward and drive cell migration (72; 73). The magnitude of the protrusion force generated by actin polymerization depends on the density of active actin filament. To estimate the value of protrusion force driving cell migration in one time step (30 minutes in our model), we take account the time length of maturation of focal complex. During cell migration, cell forms the new focal complex on the leading edge to increase the concentration of actin filaments to generate the protrusion force (188). Since the maturation time of focal complex formation on the leading edge is approximately 60 seconds (178), we

assume that the protrusion force is only activated after every 60 seconds. Therefore, there are approximately 30 rounds of activated protrusion force per unit length during one time step of one hour. We then sum them over the one hour period to obtain the accumulated protrusion force $|f_{af}| = 6$ nN/μm per unit length within one time step. Each actin filament on leading edge generates protrusion force ~2 pN (74) and there are about 100 active filament per 1 μm on the leading edge (75).

3.2.7 Cell apoptosis and wound element removal

Upon the initiation of the re-epithelialization process, keratinocytes regulated by EGF and KGF migrate into the wound bed and clear up the fibrin clot (76). To model the degradation of wound element by a keratinocyte, we remove the site of wound element when a migrating keratinocyte overlaps with it. In addition, if a keratinocyte in the tissue apoptosizes, it is removed from the system. Details are described in ref (38).

3.2.8 Geometry of wound bed and tissue regions

We study a wound bed of size 800 μm × 300 μm (Figure 10a). For ease of discussion, we follow a previous study (77) to divide the locations of keratinocytes into four regions based on their distance to the wound edge. Cells in Regions I, II, III, and IV have distance 0–80 μm, 80–160 μm, 160–240 μm, and >240 μm to the wound edge, respectively (Figure 10a). Experimental studies on normal re-epithelialization showed that the wound closure rate is around 300 μm/day (78; 79). It would take 1~2 days to achieve complete wound closure for the wound size we used in this study.

3.2.9 Measuring efficiencies of re-epithelialization

We introduce two new measures, *wound closure ratio* $\rho(t_n)$ and *migration direction angle* $\alpha(t_n)$, to quantify the efficiency of re-epithelialization. These are used along with *migration persistence* $p(t_n)$ and *normalized separation distance* $d_{i,j}(t_n)$ introduced by previous studies (80; 77). The *wound closure ratio* $\rho(t_n)$ measures the degree of closure of the wound bed:

$$\rho(t_n) = \frac{n_w(t_0) - n_w(t_n)}{n_w(t_0)}, \tag{3.8}$$

where $n_w(t_n)$ is the number of remaining discrete wound element units in the wound bed at time t_n, $n_w(t_0)$ is the total number of discrete wound element units in the wound bed before re-epithelialization (Figure 10b). Initially, $\rho(t_n) = 0$ and $\rho(t_n) = 1$ when re-epithelialization is completed. The *migration direction angle* $\alpha(t_n)$ measures the directionality of migrating cell towards the wound bed (Figure 10c). It is defined as the angle between the direction of a migrating cell and its direction to the nearest wound edge at time t_n:

$$\alpha(t_n) = \arccos(\mathbf{u}_c \cdot \mathbf{u}_w) \cdot \mathrm{sgn}(\| \mathbf{u}_c \times \mathbf{u}_w \|), \tag{3.9}$$

where $\mathbf{u}_c$ is the unit vector of the direction of cell migration, $\mathbf{u}_w$ is the unit vector of direction from the cell mass center to its nearest wound edge, $\mathrm{sgn}(x)$ is the sign of x (Figure 10c). The smaller $\alpha(t_n)$ is, the more accurate the migration direction is. The *migration persistence* $p(t_n)$

measures the ratio of the distance between the start and the end points over the length of the traversed path at time t_n (77) (Figure 10d):

$$p(t_n) = \frac{|\mathbf{x}(t_n) - \mathbf{x}(t_0)|}{\sum_{k=0}^{n-1} |\mathbf{x}(t_{k+1}) - \mathbf{x}(t_k)|}, \tag{3.10}$$

where t_0 is the initial time, $\mathbf{x}(t_i)$ is the position of cell at time step t_i. The higher $p(t_n)$ is, the more persistent the cell migration is. The *normalized separation distance* between (i, j) cell pair $d_{i,j}(t_n)$ measures the diverging distance of the initially neighboring cell pair (i, j) at time t_n (80) (Figure 10e):

$$d_{i,j}(t_n) = \frac{||\mathbf{x}_i(t_n) - \mathbf{x}_j(t_n)| - |\mathbf{x}_i(t_0) - \mathbf{x}_j(t_0)||}{\frac{1}{2}(\sum_{k=0}^{n-1} |\mathbf{x}_i(t_{k+1}) - \mathbf{x}_i(t_k)| + \sum_{k=0}^{n-1} |\mathbf{x}_j(t_{k+1}) - \mathbf{x}_j(t_k)|)}. \tag{3.11}$$

The numerator measures the separation distance between cells i and j at time t_n, and the denominator measures the averaged path length of cells i and j at time t_n. The smaller $d_{i,j}(t_n)$ is, the better collective cell-cell coordination for this pair of cells is achieved during cell migration.

3.2.10 Guidance mechanisms of cell migration

The success of wound healing depends on the ability of cells to follow directional cues to cover the wound bed, but how cells navigate in a dynamically changing and noisy environment remains a puzzling question (81). Experimental studies revealed that there exist three guidance mechanisms for a cell to determine its migrating direction. Under *chemokinesis*, biochemical soluble factors stimulate a cell and initiate the migration process but does not

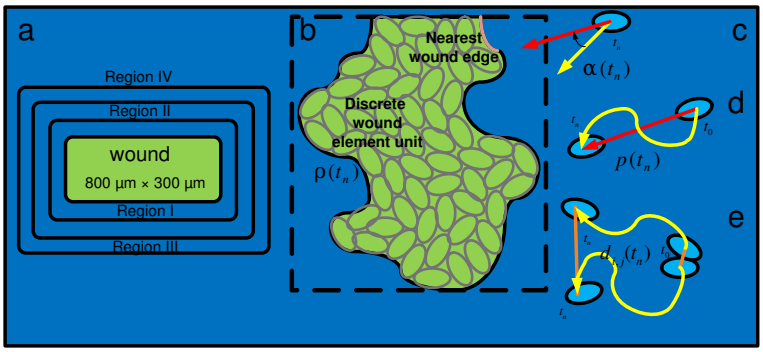

Figure 10. **Geometry of wound bed and quantifying re-epithelialization efficiency.** (a) The size of the wound in our model is 800 μm × 300 μm. The locations of keratinocytes are divided into four regions according to their distances to the wound edge: 0~80 μm for Region I, 80~160 μm for Region II, 160~240 μm for Region III, >240 μm for Region IV. (b) Wound closure ratio $\rho(t_n)$ is given by the number of remaining discrete wound element units in the wound bed at time t_n divided by the total number of discrete wound element units before re-epithelialization. (c) Migration direction angle $\alpha(t_n)$ is the angle between the direction of migration (yellow arrow) and the direction of the cell to the nearest wound edge (red arrow). (d) Migration persistence $p(t_n)$ is the ratio of the distance from the current position of the cell at time t_n to its original position (red line segment), divided by the length of the traversed path (yellow curve). (e) Normalized pair separation distance $d_{i,j}(t_n)$ is the separation distance between a pair of cells at time t_n which were initially neighbors (orange line), normalized by the average length of cell traversed path (yellow curve).

provide the direction of migration (82). Under *chemotaxis*, the direction of cell migration is dictated by the biochemical gradient of soluble factors (82). Under *cohesotaxis*, the direction of cell migration is determined by the intercellular force gradients (81). While all these different guidance mechanisms may contribute to the complex process of collective cell migration during re-epithelialization, the exact roles of each individual control mechanism in regulating wound healing is not well understood. In previous studies, the type of molecules triggering cell migration varies, depending on cell type and biological phenomena. The motility of *Bacillus subtilis* is triggered by the activation of histidine kinase CheA (83); The migration of fibroblast is triggered by PDGF during wound healing (53). For simplicity, we assume EGF as the trigging molecule for cell migration under both chemokinesis and chemotaxis in our model. In our chemokinesis model, each keratinocyte begins to migrate upon activation triggered by a local EGF gradient between this cell and any of its neighbors. The direction of the migration is randomly chosen from a uniform distribution $\mathcal{U}(0, 360)$ of angles. In our chemotaxis model, each keratinocyte begins to migrate if there exists a local EGF gradient between a cell and any of its neighboring cells. The migrating direction is chosen along that of the highest EGF gradient, plus a random deviation angle sampled from a normal distribution $\mathcal{N}(0, 33)$ of angles (84) (Figure 11a). In our cohesotaxis model, the migrating cell generates contraction force at its rear edge due to cell elasticity in the opposite direction against the protrusion force on its leading edge. A keratinocyte begins to migrate if there exists a gradient of local contraction force with its neighboring cells. The migrating direction is along the vector sum of the contraction force

gradients from its neighbors, plus a random deviation angle sampled from a normal distribution $\mathcal{N}(0, 33)$ of angles (Figure 11b). Simulation for each model is repeated three times.

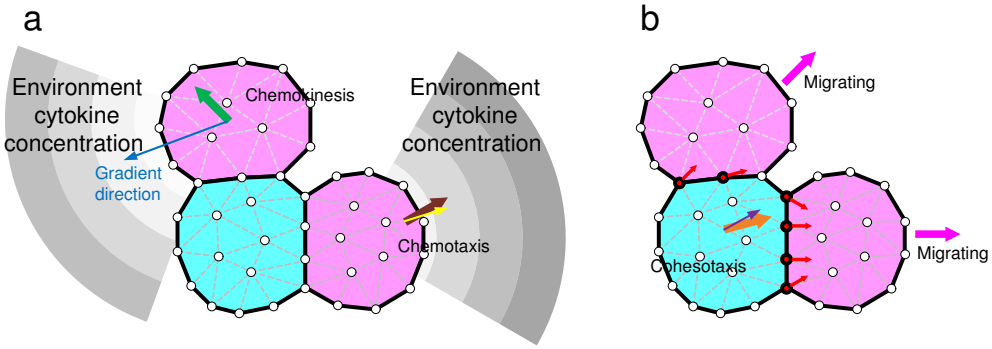

Figure 11. **Guides mechanisms of cell migration.** (a) In chemokinesis, growth factor gradient (blue arrow) activates cell migration but cells move in random directions (green arrow). In chemotaxis, the migration direction is taken as the largest growth factor gradient (brown arrow), plus a random deviating angle sampled from the normal distribution of $\mathcal{N}(0, 33)$ of angles (yellow arrow). (b) In cohesotaxis, a cell migrates along the direction of the vectors of local intercellular contraction force. The contraction force vectors (red arrows) on each vertex (red vertices) of the cell boundary with a neighboring cell are summed, and the overall vector (orange arrow), plus a random deviating vector whose angle is sampled from the normal distribution $\mathcal{N}(0, 33)$ of angles (purple arrow), gives the migration direction.

3.3 Results

3.3.1 Efficiencies of re-epithelialization under different guidance mechanisms

We first compare the efficiency of re-epithelialization under the three different guidance mechanisms of cell migration.

Directional cue is required for in-time re-epithelialization. The time duration for re-epithelialization varies for the different guidance mechanisms. For full wound closure in which the wound closure ratio $\rho(t_n)$ increased from 0.0 to 1.0, the full time duration was 57±1 hours, 52±1 hours, and 186±6 hours for chemotaxis, cohesotaxis, and chemokinesis, respectively (Figure 12a–Figure 12c). The wound closure time for both chemotaxis and cohesotaxis were within the range of physiological time. However, the closure time under chemokinesis was 4~5 times longer than the observed physiological time (Figure 14a). These results indicated that directional cue guiding cell migration is required for in-time wound closure. We also measured the migration speed $s(t_n)$ during the re-epithelialization process, which is defined as the total length of the cell migrating trajectory over migrating time. Keratinocytes under cohesotaxis mechanism exhibited the highest migration speed in Region I, with $s(t_n) = 3.3 \pm 0.1\ \mu m/h$. In contrast, the migration speed in Region I was only $s(t_n) = 2.8 \pm 0.1\ \mu m/h$ under chemotaxis mechanism. Under both chemotaxis and cohesotaxis, the migration speed in Region I is within the physiological range of observed single keratinocyte migration speed, $\sim 5 \mu m/h$ (85). Under chemokinesis, the migration speed was only $s(t_n) = 0.9 \pm 0.1\ \mu m/h$, which was much slower than that of other mechanisms with guidance of directional cue (Figure 14b).

Chemotaxis increases directional accuracy of cell migration. We next examined the direction angle $\alpha(t_n)$ of keratinocyte migration under different guidance mechanisms and measured the fractions of cells with $\alpha(t_n) \leq 30^\circ$ and $\alpha(t_n) \leq 60^\circ$ (Figure 15a). Cells under chemotaxis achieved the most accurate directionality: $38 \pm 1\%$ and $66 \pm 3\%$ of the total migrating keratinocytes had $\alpha(t_n) \leq 30^\circ$ and $\alpha(t_n) \leq 60^\circ$, respectively (Figure 15a). Cells

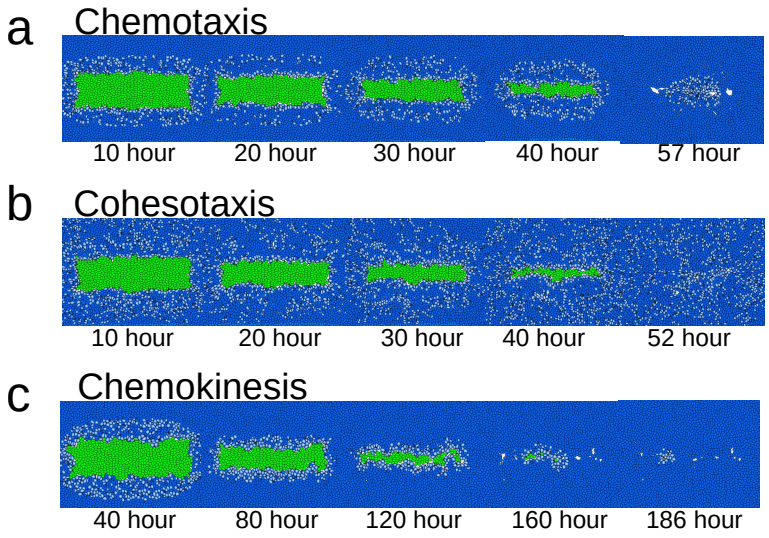

Figure 12. **Tissue snapshots under different guidance mechanisms of cell migration.** (a–c) Snapshots of tissue during re-epithelialization at different time under the three different guidance mechanisms. Blue: keratinocytes; Green: wound elements. Light blue: migrating keratinocytes at a specific time step.

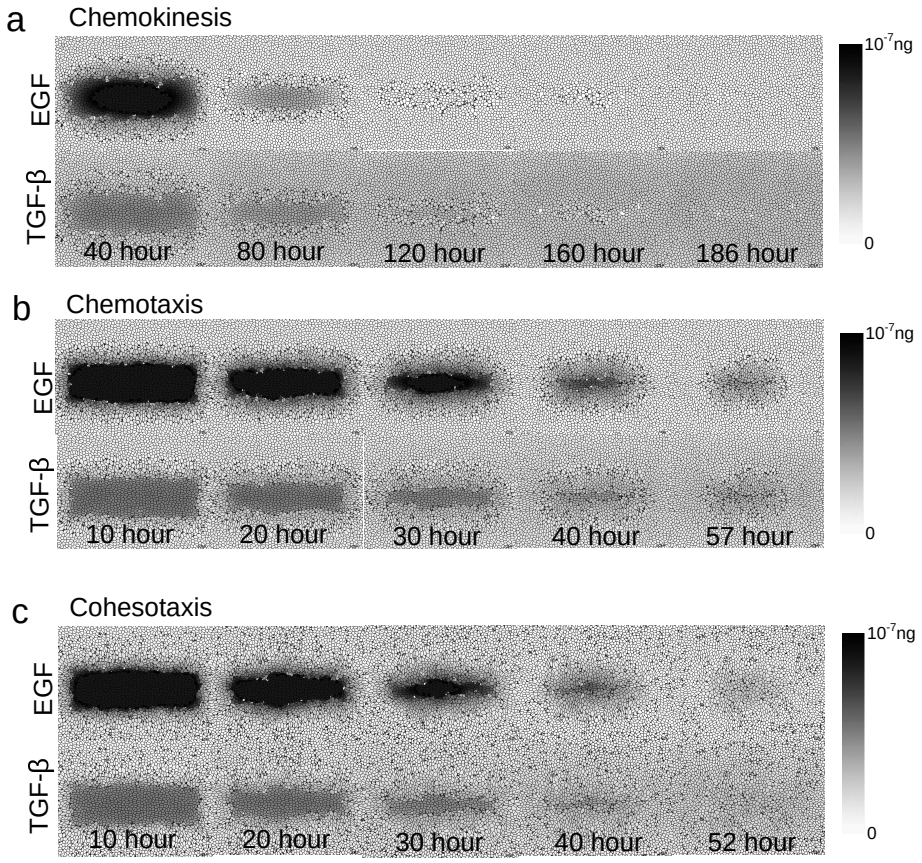

Figure 13. **Concentration of growth factors under three different guidance mechanisms of cell migration.** (a) The concentrations of EGF and TGF-β under chemokinesis. (b) The concentrations of EGF and TGF-β under chemotaxis. (c) The concentrations of EGF and TGF-β under cohesotaxis.

under cohesotaxis had less accurate directionality: $27 \pm 2\%$ and $50 \pm 3\%$ of the total migrating keratinocytes had $\alpha(t_n) \leq 30^\circ$ and $\alpha(t_n) \leq 60^\circ$, respectively (Figure 15a). As expected, cells under chemokinesis migrated in random direction, with only $16 \pm 1\%$, and $33 \pm 1\%$ of the total migrating keratinocytes with $\alpha(t_n) \leq 30^\circ$ and $\alpha(t_n) \leq 60^\circ$, respectively. Both were the levels expected for cells with random directionality uniformly distributed between $0 \sim 360^\circ$

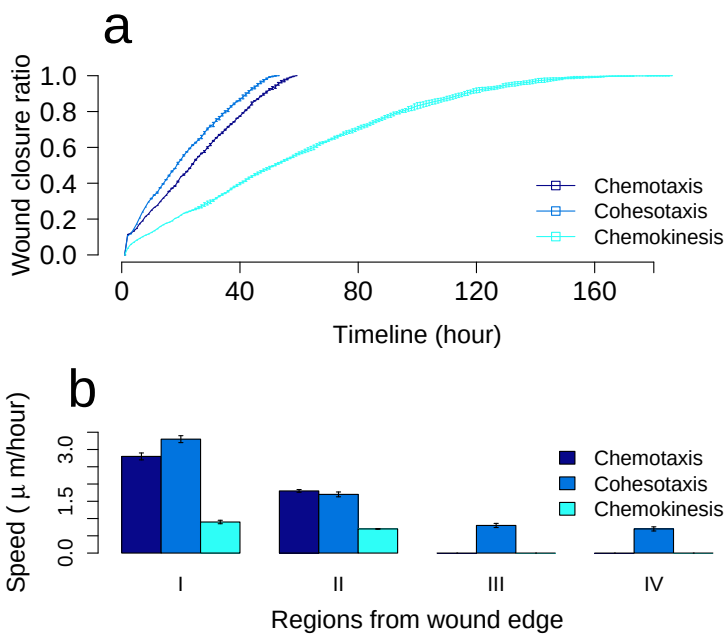

Figure 14. **Wound closure and cell migration speed under different guidance mechanisms of cell migration.** (a) Wound closure ratio $\rho(t_n)$ over time under the three different guidance mechanisms. (b) Average migration speed of migrating keratinocytes $s(t_n)$ during re-epithelialization. The error bars depict the standard deviations of three simulation runs.

(Figure 15a). Overall, cells under biochemical guidance migrated with better directionality towards the wound bed.

Chemotaxis guides cell migration with higher persistence. We then examined the migration persistence $p(t_n)$ of keratinocyte under different guidance mechanisms. Due to the limited range of growth factor diffusion, biochemical signaling molecules only reached to Region II of the wound tissue (see Figure 13). Therefore, migrating cells under chemotaxis and chemokinesis triggered by EGF, reached only as far as Region II (Figure 12a and Figure 12c). Under both chemotaxis and cohesotaxis, keratinocytes close to the wound edge migrated with higher persistence than keratinocytes far from the wound edge. Under chemotaxis, the persistences decreased from $p(t_n) = 79 \pm 1\%$ in Region I to $p(t_n) = 73 \pm 1\%$ in Region II, with the overall high persistence ($p(t_n) > 70\%$) maintained throughout Region I and Region II where biochemical signal were present (Figure 15b). Under cohesotaxis, the persistence decreased from $p(t_n) = 73 \pm 2\%$ in Region I to $p(t_n) = 66 \pm 2\%$ in Region II, and then significantly to only $p(t_n) = 52 \pm 3\%$ in Region IV as the distance of cells from the wound edge increased (Figure 15b). Chemokinesis differed from both chemotaxis and cohesotaxis, as keratinocytes migrated with very low persistence ($p(t_n) \leq 50\%$ in both Region I and Region II) because of the random nature of the migrating direction. The value of $p(t_N)$ measured from the *in vitro* study of Ng, et al (77) is also plotted to show that our simulation results are in the same order of magnitude (Figure 15b). Overall, cells under guidance of biochemical cue migrated with highest persistence.

Cohesotaxis improves coordination of collective cell migration. We then measured the normalized cell pair separation distance $d_{i,j}(t_n)$ under different guidance mechanisms. Under both chemotaxis and chemokinesis, the separation distance $d_{i,j}(t_n)$ became larger as the distance to wound edge increased. Under chemotaxis, the separation distance $d_{i,j}(t_n)$ increased significantly from 0.14 ± 0.01 in Region I to 0.21 ± 0.01 in Region II (Figure 15c). Under chemokinesis, $d_{i,j}(t)$ increased slightly from 0.08 ± 0.01 in Region I to 0.10 ± 0.01 in Region II (Figure 15c). Under cohesotaxis, however, the separation distance decreased as the distance from wound edge increased: $d_{i,j}(t_n)$ decreased from 0.14 ± 0.01 in Region I to 0.10 ± 0.01 in Region IV (Figure 15c). Our simulation results are in general agreement with experiments of Ng, et al. (77) (Figure 15c). These results demonstrated that mechanical cues can coordinate collective cell migration better, with lower separation distance between migrating cell pairs.

Remark. Our studies on direction angle $\alpha(t_n)$ and migration persistence $p(t_n)$ showed that biochemical cues provide better guidance for directing keratinocytes to migrate into the wound bed with more accurate directionality and higher migration persistence (Figure 15a and Figure 15b). Our studies on normalized separation distance $d_{i,j}(t_n)$ and the migration speed $s(t_n)$ showed that mechanical cues provide better coordination on the collective migration of cells, with lower separation distance and higher migration speed (Figure 14b and Figure 14c).

3.3.2 Efficiency of re-epithelialization under different level of growth factors

Growth factor concentration plays important roles in regulating cell behavior during wound healing. In our model, an intercellular signaling network regulating growth factor synthesis is embedded in each cell. Previous computational study have investigated the effects of different

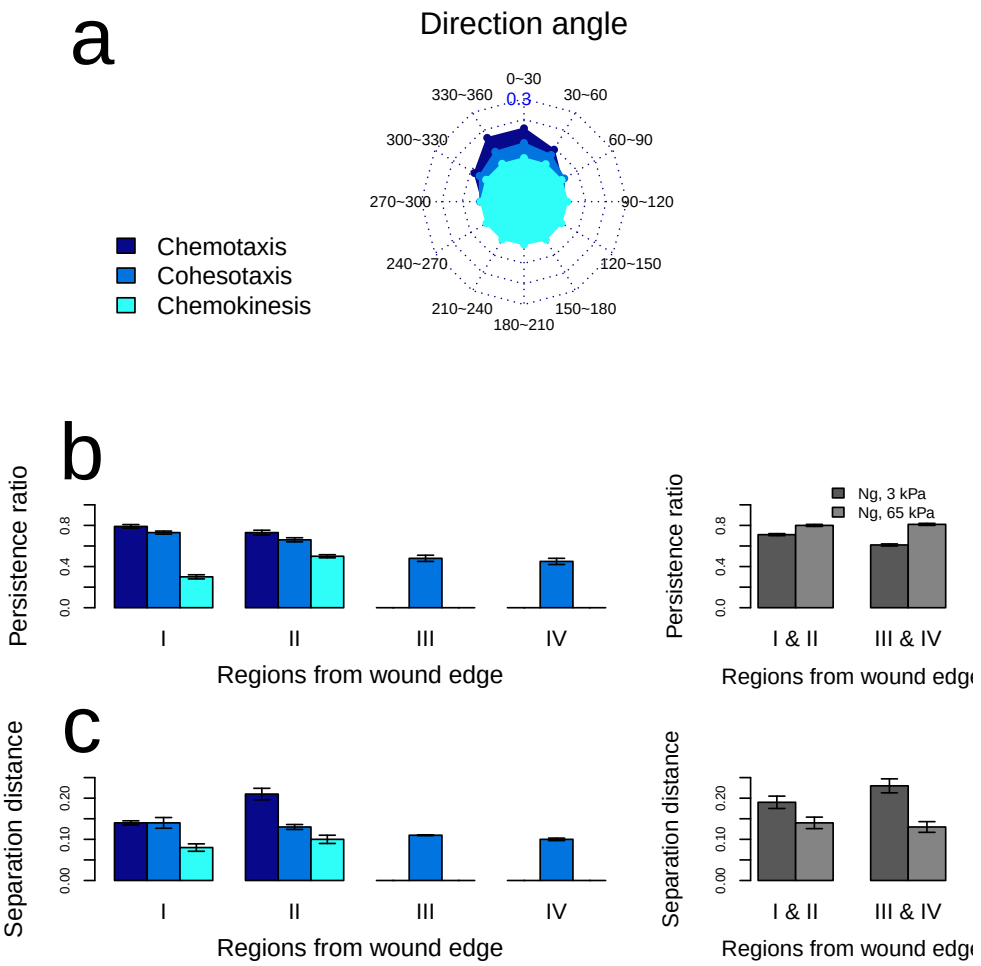

Figure 15. **Efficiency of re-epithelialization under the three different guidance mechanisms of cell migration.** (a) Radar chart of the distribution of direction angle of migrating keratinocyte $\alpha(t_n)$ accumulated during the full process of re-epithelialization. The complete angle range (0°, 360°) is divided into 12 intervals. Each spoke of the radar chart shows the proportion of $\alpha(t_n)$ within that specific interval. (b–c) The persistence ratio $p(t_n)$, and the normalized cell separation distance $d_{i,j}(t_n)$ of migrating keratinocytes under the three guidance mechanisms at varying distances from the wound edge during re-epithelialization. Data of migration persistence and normalized separation distance from *in vitro* study using matrix of different stiffness (3 kPa and 65 kPa) are also plotted. The error bars depict the standard deviations of three simulation runs.

growth factors on wound healing by constructing growth factor network within cells (53; 64). Following these studies, we considered only the three most important growth factors, EGF, KGF and TGF-β in our network for simplicity (28). A previous study showed that there exists pronounced cell proliferation and migration of epithelial cells with the presence of EGF, while modest cell proliferation with the presence of KGF (86). Furthermore, the presence of TGF-β is found to inhibit cell proliferation (86; 87). Based on these studies, we use a simplified scheme to model cell behaviors. The probabilities of migration and proliferation of keratinocytes are stochastically controlled by the growth factor concentration. EGF and KGF elevate while TGF-β lowers the probability of cell proliferation. In addition, EGF elevates the probability of cell migration.

We then examined the influence of growth factor conditions on the re-epithelialization efficiency under the mechanisms of chemotaxis and cohesotaxis by altering the synthesis rate of individual growth factor separately. The efficiency of re-epithelialization in terms of wound closure rate, migration persistence, normalized separation distance, and migrating speed were then compared to those obtained under normal synthesis rates. As EGF and KGF have overlapping function in promoting cell proliferation, and the effectiveness of KGF is far less pronounced than that of EGF (86), we only adjusted the synthesis rates of EGF and TGF-β in our studies.

Effects of TGF-β. With increased TGF-β synthesis rate, there were fewer proliferating keratinocytes in the tissue, and the re-epithelialization process was prolonged with unhealed wound (88) still present at the end of re-epithelialization (see Figure 16a). Under chemotaxis, the average proliferation index $\rho_i(j)$ over re-epithelialization decreased from $14.0 \pm 0.3\%$ to

$11.4 \pm 0.2\%$ as the synthesis rate of TGF-β increased to 4–fold of the normal rate (from $1.3 \times 10^{-7} ng/cell/day$ to $5.2 \times 10^{-7} ng/cell/day$, Figure 17a). Under cohesotaxis, the average proliferation index $\rho_i(j)$ over re-epithelialization decreased from $13.8 \pm 0.3\%$ to $10.8 \pm 0.1\%$ as the synthesis rate of TGF-β increased to 4–fold of the normal rate (Figure 17). Under both chemotaxis and cohesotaxis, it took longer to cover the wound bed (57±1 versus 53±1 hours under chemotaxis and 55±2 versus 48±1 hours under cohesotaxis when TGF-β synthesis rate increased to 4–fold of the normal rate, Figure 17b and Figure 17c).

With decreased TGF-β synthesis rate, there were more proliferating keratinocytes in the tissue. Under chemotaxis, the average proliferation index $\rho_i(j)$ over re-epithelialization increased from $14.0 \pm 0.3\%$ to $19.1 \pm 0.2\%$ as TGF-β synthesis rate decreased to 20% of the normal rate (from $1.3 \times 10^{-7} ng/cell/day$ to $2.6 \times 10^{-8} ng/cell/day$, Figure 17a). Under cohesotaxis, the average proliferation index over re-epithelialization increased from $13.8 \pm 0.3\%$ to $19.9 \pm 0.2\%$ as TGF-β synthesis rate decreased to 20% of the normal rate (Figure 17a). Interestingly, it also took longer to cover the wound bed (66±2 versus 53±1 hours under chemotaxis and 61±2 versus 48±1 hours under cohesotaxis when TGF-β synthesis rate decreased to 20% of the normal rate, Figure 17b and Figure 17c).

Effects of EGF. In contrast to the complex effects of TGF-β, EGF affected re-epithelialization in a straightforward manner. With increased EGF synthesis rate, there were more proliferating keratinocytes in the tissue. The re-epithelialization process was also accelerated (see Figure 16b). Under chemotaxis, the average proliferation index increased from 14.0±0.3% to 17.7± 0.1% as EGF synthesis rate increased to 4-fold of the normal rate (from $5.1 \times 10^{-7} ng/cell/day$

to $2.0 \times 10^{-6} ng/cell/day$, Figure 18a). Under cohesotaxis, the average proliferation index $\rho_i(j)$ increased from $13.8 \pm 0.3\%$ to $15.0 \pm 0.3\%$ as the EGF synthesis rate increased to 4–fold of the normal rate (Figure 18a). Under both chemotaxis and cohesotaxis, it took less time to cover the wound bed (43±1 versus 57±1 hours under chemotaxis and 42±1 versus 52±1 hours under cohesotaxis when EGF synthesis rate increased to 4–fold of the normal rate, Figure 18b and Figure 18c).

With reduced EGF synthesis rate, there were fewer proliferating keratinocytes in the tissue and the re-epithelialization process is prolonged. Under chemotaxis, the average proliferation index decreased from $14.0 \pm 0.3\%$ to $12.6 \pm 0.1\%$ as EGF synthesis rate decreased to 30% of the normal rate (from $5.1 \times 10^{-7} ng/cell/day$ to $1.5 \times 10^{-7} ng/cell/day$, Figure 18a). Under cohesotaxis, the average proliferation index $\rho_i(j)$ also decreased from 13.8±0.3% to 13.2±0.1% as EGF synthesis rate decreased to 30% of the normal rate (Figure 18a). For both chemotaxis and cohesotaxis, it took longer to cover the wound bed (79±3 versus 57±1 hours under chemotaxis and 62±2 versus 52±1 hours under cohesotaxis when EGF synthesis decreased to 30% of the normal rate, Figure 18b and Figure 18c).

3.3.3 Spatio-temporal patterns of proliferation of keratinocyte

Proliferation provides fresh new cells for wound repair. We study how different patterns of cell proliferation of a population of cells may arise from mechanical and biochemical guidance cues of cell migration and how these patterns of cell proliferation under chemotaxis and cohesotaxis affect the process of re-epithelialization (78). We divided the whole tissue of size 1600 μm × 700 μm into 56 blocks, each of size 200 μm × 100 μm. Blocks directly covering

the wound bed belong to the *central region* (12 blocks); blocks immediately neighboring the wound bed belong to the *surrounding region* (18 blocks). The time-course of re-epithelialization is divided into four intervals, 0~12, 13~24, 25~36, and 37~48 hours, after the initiation of re-epithelialization. The proliferation index of keratinocyte $\rho_i(j)$ in region i at time interval j is then calculated as $\rho_i(j) = \frac{n_{d,i}(j)}{n_i(j)}$, where $n_{d,i}(j)$ is the number of keratinocytes that are newly generated inside region i during time interval j, $n_i(j)$ is the average number of keratinocytes inside region i during time interval j.

The spatial pattern of distribution of proliferating keratinocytes differs in tissue under chemotaxis and tissue under cohesotaxis (Figure 19a and Figure 19b). Under chemotaxis, proliferating keratinocytes were highly concentrated in the wound surrounding region (Figure 19a), but were more scattered throughout the tissue under cohesotaxis (Figure 19b). The spatial proliferating pattern under chemotaxis is more consistent with that of a previous experimental study compared to that under cohesotaxis, which showed that there exists a burst of cell proliferation at the wound margin during the early stage of re-epithelialization (89). These different spatial patterns of cell proliferation (Figure 19a and Figure 19b) are due to the different effects of biochemical and mechanical cues on guiding cell migration: under chemotaxis, cell migration only occurs in the regions close to the wound bed, while under cohesotaxis, cell migration occurs in all regions across the wound tissue. This indicates that compared to the tissue under chemotaxis, there is less contact inhibition from neighboring cells in regions far from the wound bed under cohesotaxis. Therefore cells in those regions have relatively more free

space to proliferate. Therefore, the distribution of locations of dividing cell is more scattered under cohesotaxis.

In addition, the temporal patterns of keratinocyte proliferation also differ under chemotaxis and cohesotaxis (Figure 19c and Figure 19d). Under chemotaxis, the proliferation index $\rho_i(j)$ in the central region remained at an elevated level after 24 hours but decreased significantly in the surrounding region after 24 hours (Figure 19c). $\rho_i(j)$ in the central region reached $23.1 \pm 1.1\%$ during the first 24 hours, and remained as $26.1 \pm 1.0\%$ after 24 hours. $\rho_i(j)$ in the surrounding region reached $15.7 \pm 0.9\%$ during the first 24 hours, but decreased to $8.3 \pm 1.0\%$ after 24 hours. Under cohesotaxis, the proliferation index $\rho_i(j)$ in both the central and the surrounding regions had similar patterns (Figure 19d). $\rho_i(j)$ in the central region increased from $5.1 \pm 0.2\%$ to $19.9 \pm 1.0\%$ in the first 24 hours, and then decreased to $13.9 \pm 0.6\%$ after 24 hours. $\rho_i(j)$ in the surrounding region increased from $1.0 \pm 0.1\%$ to $13.2 \pm 0.8\%$ in the first 24 hours, and then decreased to $10.7 \pm 0.6\%$ after 24 hours. These temporal patterns of proliferation were also maintained at accelerated proliferation level (modeled by decreasing the synthesis rate of TGF-β), and at inhibited proliferation level (modeled by increasing the synthesis rate of TGF-β) under either chemotaxis (Figure 19e and Figure 19g) or cohesotaxis (Figure 19f and Figure 19h).

We then asked if this temporal pattern of proliferation was influenced by the level of keratinocyte proliferation. So we next examined the temporal pattern of proliferation with accelerated proliferation level (decreasing the synthesis rate of TGF-β), and with inhibited proliferation level (increasing the synthesis rate of TGF-β). In both cases, the same temporal

pattern of proliferation was maintained under either chemotaxis (Figure 19e and Figure 19g) or cohesotaxis (Figure 19f and Figure 19h).

The temporal pattern of keratinocyte proliferation under chemotaxis (Figure 19c) is consistent with the observation in recent experimental study, in which it was found that the epidermal proliferation index in the wound region remained at a high level, while proliferation in the surrounding region decreased significantly. This pattern was maintained even after more than 80% of re-epithelialization was completed (78). The different temporal patterns of cell proliferation we observed (Figure 19c and Figure 19d) are due to the different effects of biochemical and mechanical cues on guiding cell migration in our model: under chemotaxis, cell migration only occurs in regions close to the wound bed, while under cohesotaxis, cell migration occurs in all regions across the wound tissue. As a consequence of these differences, tissue under cohesotaxis achieves re-epithelialization on average 4 hours faster during the complete re-epithelialization process of 48 hours. There are more unhealed wound elements remained after 24 hours under chemotaxis than that under cohesotaxis. These wound elements release EGF to promote further cell proliferation. Therefore, the proliferation index in the central region inside the wound bed remained elevated after 24 hours under chemotaxis, but is decreased under cohesotaxis.

Overall, our simulation using a simplified re-epithelialization model showed how different guidance cues influence the pattern of cell proliferation. The agreement between our simulation results and experimental observations suggests that biochemical cues are likely the dominant factors dictating the migration of keratinocytes in the wound surrounding region.

3.3.4 Effects of cell-cell boundary shape on signal transmission

Intercellular adhesion has been shown to facilitate transmission of the contraction forces through the E-cadherin complex (77). Since the cell-cell boundary is usually in curved shape (90), we next investigate if the shape of cell-cell boundary influences the cell migration and tissue patterning during re-epithelialization. To address this question, we modified the cohesotaxis model under an alternative mode, called *shape-independent cohesotaxis*.

In regular cohesotaxis, once a cell experiences the contraction force exerted from a neighboring cell, its migration direction is that of the vector of contraction force. When multiple neighboring cells exert contraction forces to the same cell, it migrates along the direction of the summed vector of contraction forces. In this case, the geometry of the cell boundary where adhesion occurs plays important role, as forces exerting on each of the boundary elements collectively determine the migrating direction (Figure 20a). Under the alternative model of shape-independent cohesotaxis, however, the migration direction is that of the vector from the center of the migrating cell to the center of the cell exerting the contraction force, regardless the actual force directions (Figure 20b). When multiple neighboring cells exert contraction forces to the same cell, the vector sum of contraction forces is calculated, and the cell where this vector points to is identified. We then set the migration direction as that of the vector connecting the migrating cell center to this identified cell center. In this alternative model, the geometry of the cell boundaries plays less important role, especially when contraction force comes from only one neighboring cell.

The results showed that, under the control of shape-independent cohesotaxis, the full wound closure time was prolonged to 88±3 hours, compared to 48±1 hours under normal cohesotaxis control (Figure 21a). The direction angle also decreased dramatically: only $20 \pm 2\%$ of total migrating keratinocytes had direction angle less than 30°, compared to $27 \pm 2\%$ under regular cohesotaxis control (Figure 21b). The migration persistence also decreased significantly in each Region under the control of shape-independent cohesotaxis compared to the regular cohesotaxis. For example, in Region I, migration persistence decreased from 73±3% to 50±4% (Figure 21c). However, cells were better coordinated in migration: the normalized separation distance was smaller in each Region under the control of shape-independent cohesotaxis. For example, in Region I, separation distance decreased from 0.14 ± 0.01 to 0.10 ± 0.01 (Figure 21d). Overall, these results indicate that the shape of cell-cell boundary plays important roles in guiding collective cell migration for in-time re-epithelialization.

3.3.5 Effects of disrupted intercellular adhesions on collective cell migration

Cell-cell adhesions are critical in coordinating collective cell migration in both *in vivo* and *in vitro* studies (91; 92; 52). Studies provided evidence that mechanical tension are transmitted through E-cadherin from neighboring cells when responding to external mechanical stimulus. Many factors are known to be regulators of cell-cell adhesions. The inhibition of myosin-II rapidly decreases cadherin-based cell adhesiveness (93), and the depletion of αE-catenin significantly affects the transmission of mechanical force through cell-cell contacts (94). We explored how disruption of cell-cell adhesion affect the re-epithelialization efficiency under the cohesotaxis where cells migrate following the contraction signal transmitted from neighboring

cells. We first studied the effect of inhibition of myosin-II activity by decreasing the adhesion due to cadherin between keratinocytes. We then reduced the levels of αE-catenin depletion by gradually inhibiting the contraction signal transmission between keratinocytes.

Decreased cell-cell adhesion reduces cell-cell coordination during collective cell migration. To study the effects of reduced cell-cell adhesions, we examined the process of re-epithelialization under cohesotaxis at different adhesion intensities of 3.2, 2.2, 1.2, and 0.2nN/μm^2, all less than the normal intensity of 4.1nN/μm^2. As adhesion is reduced, there are more unhealed wound areas present in the tissue after complete wound closure (Figure 22). The corresponding re-epithelialization time for complete wound closure is 49±1, 48±1, 49±1, and 53±1 hours, respectively (Figure 22 and Figure 23a).

Comparing with the complete re-epithelialization time, 52±1 hours under normal cell-cell adhesion of 4.1nN/μm^2, there is no significant difference in the required duration for wound closure due to the decrease in migration persistence, directionality and overall coordination (Figure 23b–Figure 23d). The fraction of migrating cells having direction angle less than 30° decreased from $27 \pm 2\%$ to $21 \pm 3\%$ as cell-cell adhesion decreased (Figure 23b). The migration persistence decreased in each Region as cell-cell adhesion decreased. For example, in Region I, migration persistence decreased from $73 \pm 3\%$ to $69 \pm 2\%$ (Figure 23c). The normalized separation distance in Region also increased as cell-cell adhesion decreased. For example, in Region I (0~80 μm from the wound edge), the separation distance increased from 0.14 ± 0.01 to 0.27 ± 0.01 (Figure 23d).

Our finding of the increased normalized separation distance when adhesion intensity is reduced (Figure 23d) was also observed in the *in vitro* study of epithelial cells where cell-cell coordination was significantly disrupted when myosin-II activity was reduced (Figure 23e (77)). Our simulation suggests that insufficient adhesion intensity for coordinating collective cell migration towards the wound bed may also lead to unhealed wound in the tissue after re-epithelialization (Figure 22).

Inhibition of signal transmission of intercellular contraction reduces persistence of migration. To examine the effects of reduced transmission of contraction signal, we adjust our model with different probability of transmission of contraction forces through the adhesion linkage. Namely, the vertices shared through the mutual edge of two neighboring cells. Three different decreased transmission probabilities, 80%, 50%, and 30% are used.

Compared to the re-epithelialization time of 52±1 hours under normal cohesotaxis, the average re-epithelialization time is prolonged to 53±1 hours, 59±2, and 68±2 hours (Figure 24 and Figure 25a) as the probability of transmission decreased to 80%, 50%, and 30%, respectively. Analysis showed that there is also loss in directionality and persistence upon inhibition of transmission of contraction forces (Figure 25b and Figure 25c). The fraction of migrating cells having direction angle less than 30° decreased from $27 \pm 2\%$ to $20 \pm 2\%$ (Figure 25b). The migrating persistence decreased in each Region. For example, in Region I, migration persistence decreased from $73 \pm 3\%$ to $62 \pm 2\%$ (Figure 25c).

Our results of the decreased migration persistence (Figure 25c) are consistent with the *in vitro* study of epithelial cells where the decrease of migrating persistence was observed when αE-

catenin levels were depleted (95) (Figure 25e). Our result indicates that there are much fewer activated cells migrating towards the wound bed under low transmission probability (Figure 24). The lack of correctly transmitted contraction force lead to failure in generating active flow of migrating cells necessary for efficient re-epithelialization.

Interestingly, both decreasing adhesiveness and inhibiting transmission of contraction forces lead to reduced cell migration directionality and decreased migration persistence. Furthermore, cell-cell coordination was also significantly weakened as cell-cell adhesion intensity is reduced. Together with experimental observations, these results suggest that adhesion intensity plays important roles in the transmission of mechanical forces. Adhesion through E-cadherin with strong intensity between cells is important for coordinating collective cell migration during wound healing, by enabling efficient mechanical force transmission which is important for guiding cells in wound surrounding area to migrate to the wound bed with accurate directionality and high persistence.

3.4 Conclusion and discussion

Skin re-epithelialization during wound healing is a complex process where cell proliferation and cell migration play central roles (89). There exists multiple biochemical and mechanical signaling events to regulate cell proliferation and migration. Therefore, re-epithelialization and tissue formation can be achieved in time (46).

We have applied dyCelFEM to study detailed spatio-temporal patterns of migration and proliferation of a population of cells under different cues of biochemical signaling and mechanical forces. Such detailed multi-scale investigation of geometric, topological, and mechanical changes

of a large population of migrating and proliferating cells has not yet been possible in previous computational studies of wound healing.

Our results help to delineate different roles of biochemical and mechanical cues in re-epithelialization. We found that biochemical cues influence cell behavior locally in the wound-surrounding regions, while mechanical cues influence the whole tissue globally. In addition, biochemical cues are better at guiding cell migration with improved directionality and higher persistence, while mechanical cues are better at coordinating collective migration of cells towards the wound bed.

We also investigated how cell migration influences cell proliferation during re-epithelialization. Our results showed that both spatial and temporal patterns of proliferation of keratinocytes under the control of chemotaxis (Figure 19a and Figure 19c) are consistent with experimental observations (89; 78), while patterns resulting from cohesotaxis deviate significantly from experimental observations (Figure 19b and Figure 19d). It is unlikely either chemotaxis or cohesotaxis alone controls re-epithelialization. Instead, cells migrate following directions upon integration of both biochemical and mechanical cues (81). Our results suggest that biochemical cues may play dominant roles in guiding migration of cells located in the wound surrounding region, while it plays negligible roles for cells located in regions distant from the wound bed.

A likely explanation is that biochemical and mechanical cues have different range of influence: Under chemotaxis, cell migration is initiated and guided by biochemical cues, which are present through intercellular diffusion only in regions near the wound bed. In regions distant from the wound bed, no cell migration is initiated by the biochemical cues and cell proliferation

is not affected. Under cohesotaxis, cell migration is initiated and guided by mechanical cues, which are present in the whole tissue. Cell proliferation in regions distant from the wound bed is also affected by cell migration. These differences result in the different spatio-temporal patterns of cell proliferation under chemotaxis and under cohesotaxis (Figure 19a–Figure 19d).

Our results on the effects of different levels of growth factors demonstrated that either increasing or decreasing the TGF-β synthesis rate from physiological rate can delay the re-epithelialization process (Figure 17b and Figure 17c). Indeed, it is well-known that impaired TGF-β signaling pathway delays the wound healing process (96; 97). Our study offers a mechanistic explanation: when TGF-β concentration in the tissue is reduced, there are more cells proliferating in the tissue to cover the wound. However, this effect was offset by the reduced overall efficiency of cell migration. The decreased TGF-β synthesis results in reduced migration persistence and migration speed, regardless whether the dominant guidance mechanisms is chemotaxis (Figure 17d and Figure 17h) or cohesotaxis (Figure 17e and Figure 17i).

Our results also suggest that EGF can play different roles depending on how fast it is synthesized. Increased EGF synthesis rate accelerates re-epithelialization while decreased EGF synthesis rate delays the re-epithelialization (Figure 18b and Figure 18c). These results are also consistent with experimental observations: When EGF receptor is inhibited, both cell proliferation and migration are reduced, leading to delayed wound healing (98). The following mechanism may explain these observations: When EGF concentration in the tissue is lowered, cell proliferation is reduced, with only a smaller amount of cells available to cover the wound bed. At the same time, the efficiency of cell migration is also reduced, as both migration

persistence and migration speed of cells are deceased, regardless whether chemotaxis (Figure 18d and Figure 18h) or cohesotaxis is at play (Figure 18e and Figure 18i).

Our findings of different roles of biochemical and mechanical cues in guiding collective cell migration also offers an explanation to the experimental observation of higher re-epithelialization efficiency at elevated EGF level (99). As the magnitude of the cellular protrusion force driving cell migration is independent of the growth factor concentration in our model, we are able to separate the effects of cell proliferation from those of cell migration. Our results show that increased EGF concentration enables more cells in the tissue to join the collective cell migration, resulting in overall higher collective migration speed and migration persistence, and eventually higher re-epithelialization efficiency (Figure 18). In this regard, the level of growth factor concentration can be viewed as an important factor regulating the efficiency of cell migration over long distances throughout the tissue.

Our results also suggest that the concentrations of growth factors can serve as a signal that modulates the efficiency of cell migration over long distances throughout the tissue. Tissue with higher degree of signaling (*e.g.*, elevated EGF synthesis rate) would have accelerated re-epithelialization due to the increased migration efficiency, while tissue with lower degree of signaling (*e.g.*, reduced TGF-β synthesis rate) would exhibit a prolonged re-epithelialization process as the migration efficiency is reduced, despite the fact that cell proliferation is elevated.

Moreover, our results showed that the shape of cell-cell boundary plays important roles in guiding collective cell migration for in-time re-epithelialization. Previous theoretical study has shown that the *curve-fit edge* cell model has advancement over *straight edge* cell model in

modeling more detailed cell shape, and more realistic cell motions under influence of mechanics during tissue fusion process (56). Here we reached the similar conclusion in the study of re-epithelialization process. The mechanical cues based on the geometry of the cell-cell boundary (in curve-fit edge) guided efficient re-epithelialization with more accurate directionality, higher persistence and physiological re-epithelialization timeline. In contrast, the mechanical cues whose guidance of cell migration is independent of the geometry of the cell-cell boundary, guided a prolonged re-epithelialization with less accurate directionality, lower persistence and delayed re-epithelialization timeline.

Furthermore, we characterized the effects of E-cadherin cellular adhesion in influencing the spatio-temporal pattern of re-epithelialization. Previous studies have showed that cell-cell contacts played crucial role in mechano transduction (94) and maintenance of tissue organization (100). Previous experimental studies (101; 52) and computational studies (10; 15) have showed the important roles of cell-cell adhesions in signal transmission and coordinating collective cell migration. We also obtained the same result using our cohesotaxis model. In addition, we explored the re-epithelialization process more in detail by taking account the dynamic change of cell shape along with the decreased cell-cell adhesion due to reduced myosin-II activity and inhibited mechanical signal transmission due to depleted αE-catenin to investigate their effects on re-epithelialization efficiency. We showed that the decrease of cell-cell adhesion intensity significantly perturbed the cell-cell coordination and reduced the migration directionality. This is in agreement with recent study showing that E-cadherin adhesions and the cortical F-actin cytoskeleton transduce mechanical force to side and rear cells which promotes direction sensing

during collective cell migration (102). We also showed that the inhibition of mechanical force transmission through cell-cell junctions significantly reduced the migration directionality and persistence of collective cell migration and prolonged the re-epithelialization time which were much similar to that observed in collective cell migration under random migration mechanism, chemokinesis (Figure 12). Chernyavsky, et al. have showed before that activation of some protein complex responsible for signal transmission on keratinocyte ($\alpha 7$ subunits of nAChRs) stimulated directional migration and inhibited random migration of keratinocyte (103). Our simulation along with this observation suggested that the mechanism to switch from cohesotaxis to random migration mechanism may be the result of down-regulation of cell-cell adhesion through the knockdown of adhesion complex such as actomyosin or catenin.

With better understanding of the roles of biochemical and mechanical cues in re-epithelialization, an overall mechanistic model of how these different cues cooperatively regulate cell migration and proliferation emerges. Upon wound infliction, biochemical cues of growth factors released from the wound bed are transmitted to the wound surrounding regions through intercellular diffusion. The increased local concentrations of growth factors in the surrounding regions then initiate cell in these regions to migrate along the correct direction given by the gradients of growth factors towards the wound bed. These cells form the initial migrating cellular sheet to cover the wound bed, where migration occurs with accurate directionality and strong persistence towards the wound bed. As growth factors become degraded, the intensity of biochemical cues declines and eventually becomes negligible in the wound distant region. When this occurs, mechanical cues play more prominent roles in providing the guidance mechanism. Cells in the

wound distant regions follow their neighbors and join the established moving cellular sheet to migrate collectively through well-coordinated cell-cell interactions towards the wound bed. With cell proliferation concomitantly regulated in different regions of the tissue, this cooperative regulation through biochemical and mechanical cues ensures additional supply of fresh cells for re-epithelialization.

TABLE II

Geometric, mechanical, chemical, and biological parameters used in the re-epithelialization model. The first three parameters defined the geometry and time step of our model.

Name	description	value	Ref.
Model setup			
Δt	time step lapse	30 minutes	N/A
t_τ	thickness of cell	1 μm	N/A
$\|e_\theta\|$	edge length threshold	3.14 μm	N/A
R_Ω	radius of normal keratinocyte	~ 10 μm	(176)
θ_S	sliver-removal threshold	19°	(44)
Material properties (1)			
E_K	Young's modulus of keratinocyte	120 kPa	(62)
E_W	Young's modulus of wound type	400 kPa	(63)
ν	Poisson ratio	0.40	(61)
Υ	Friction energy constant	0.9 nN/μm^3	(159)
Cell proliferation			
ΔT_Ω	human cell cycle time	24 hours	(177)
Cell migration and adhesion (2) (3)			
f_θ	rupture force of E-cadherin cell contacts	4.1 nN/μm	(41)
f_{af}	protrusion force	~ 12 nN/μm	(74; 178; 75)
Inter-cellular signaling			
D_{KGF}	diffusion rate of KGF	4.9×10^{-9}cm^2/s	(179)
D_{EGF}	diffusion rate of EGF	5.2×10^{-9}cm^2/s	(180)
$D_{TGF-\beta}$	diffusion rate of TGF-β	2.9×10^{-9}cm^2/s	(181)
$\lambda_{s,KGF}$	synthesis rate of KGF	0.40×10^{-7}ng/cell/day	(182)
$\lambda_{s,EGF}$	synthesis rate of EGF	0.51×10^{-6}ng/cell/day	(183)
$\lambda_{s,TGF-\beta}$	synthesis rate of TGF-β	0.13×10^{-6}ng/cell/day	(184)
$\lambda_{d,KGF}$	degradation rate of KGF	1.1×10^{-4}/min	(185)
$\lambda_{d,EGF}$	degradation rate of EGF	6.1×10^{-4}/min	(186)
$\lambda_{d,TGF-\beta}$	degradation rate of TGF-β	2.5×10^{-4}/min	(187)

TABLE III

Parameters used to control cell behaviors in re-epithelialization model. The unit of cytokine concentration is $1 = 10^{-9}$ng. Any concentration less than 10^{-9}ng is rounded down to 0 to ensure the logarithm term is positive. Since cell migration is a key event for re-epithelialization, the scaling factor α_2 for cell migration is to have the same value as α_1 for cell proliferation such that the behavior of migration occurs as frequently as the behavior of proliferation in our model. We assigned very small value for α_3 for cell apoptosis as behavior of apoptosis rarely occurs for keratinocyte during re-epithelialization.

Name	description	value	Ref.
Stochastic control of cell behaviors			
α_1	scaling factor of stochastic control of cell proliferation	0.11	(86)
α_2	scaling factor of stochastic control of cell migration	0.11	Estimated
α_3	scaling factor of stochastic control of cell apoptosis	0.1×10^{-8}	Estimated
α_4	scaling factor of stochastic control of cell quiescence	0.78	Estimated
β^1_{KGF}	scaling factor of KGF promoting keratinocyte proliferation	0.0015	(86)
β^1_{EGF}	scaling factor of EGF promoting keratinocyte proliferation	0.035	(86)
$\beta^1_{TGF-\beta}$	scaling factor of TGF-β inhibiting keratinocyte proliferation	0.075	(87)
β^2_{EGF}	scaling factor of EGF promoting keratinocyte migration	0.05	(86)
Cell proliferation			
k_{EGF}	scaling factor of EGF decreasing cell cycle time	0.54	(189; 190)
k_{KGF}	scaling factor of KGF decreasing cell cycle time	0.14	(70; 71)

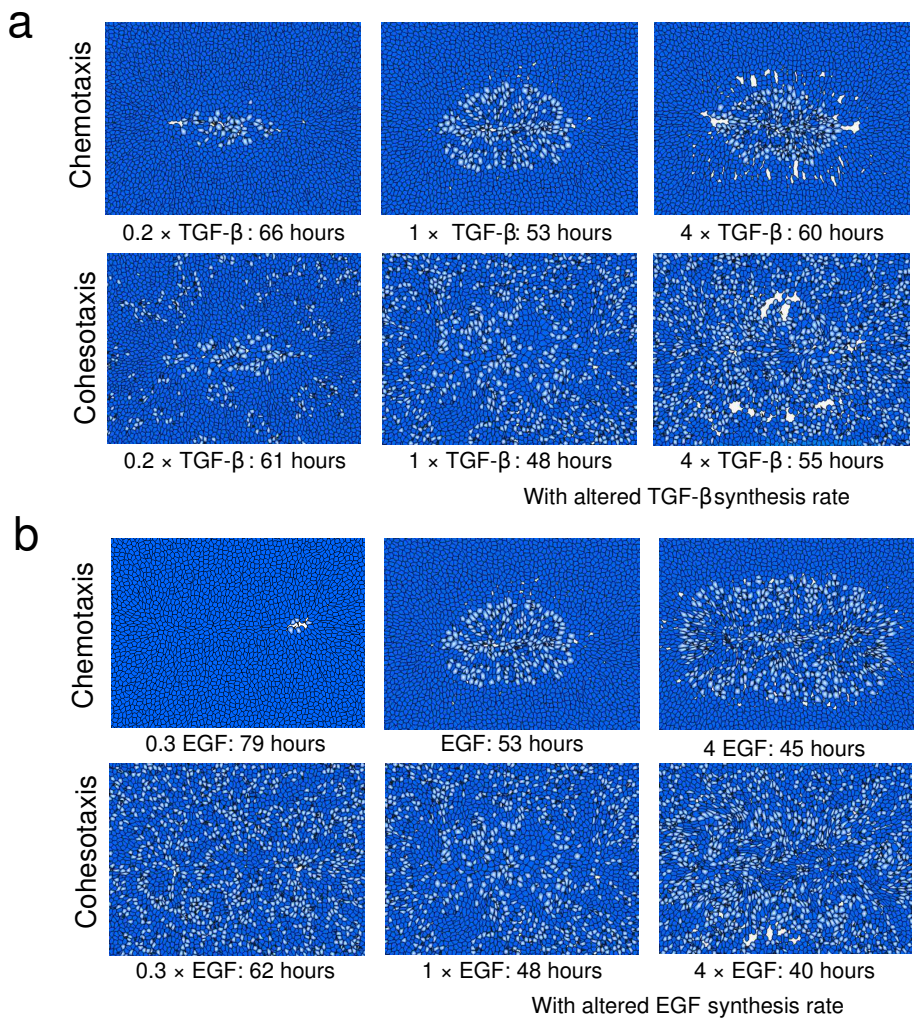

Figure 16. **Snapshots of tissue patterns under chemotaxis and cohesotaxis with altered growth factor synthesis rates.** (a) Snapshots of the wound tissue with different TGF-β synthesis rates at the end of re-epithelialization under chemotaxis and cohesotaxis with corresponding re-epithelialization time. (b) Snapshots of wound tissue with different EGF synthesis rates at the end of re-epithelialization under chemotaxis and cohesotaxis with corresponding re-epithelialization time. Blue: keratinocyte; Green: wound elements; Light blue: migrating keratinocyte at a specific time step.

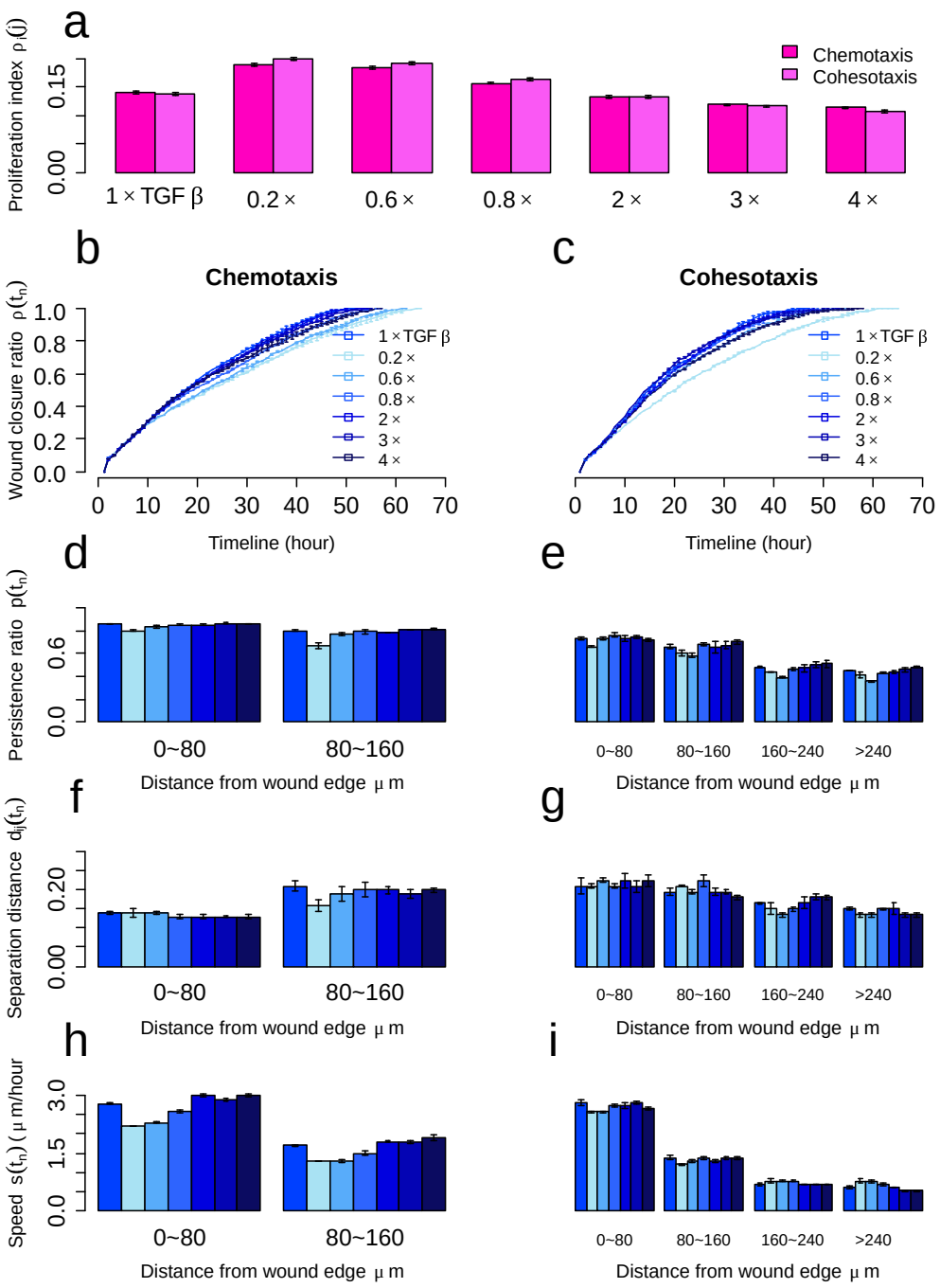

Figure 17. **Effects of altered TGF-β synthesis rates on efficiency of re-epithelialization under chemotaxis and cohesotaxis.** (a) The average proliferation index $\rho_i(j)$ during 13-48 hours with different TGF-β synthesis rates. (b–i) The wound closure ratio $\rho(t_n)$ over time (b, c), the persistence ratio $p(t_n)$ (d, e), the normalized separation distance $d_{i,j}(t_n)$ (f, g), and average migration speed $s(t_n)$ (h, i) of migrating keratinocytes during re-epithelialization with different TGF-β synthesis rates under chemotaxis and cohesotaxis. The error bars depict the standard deviation of three simulation runs.

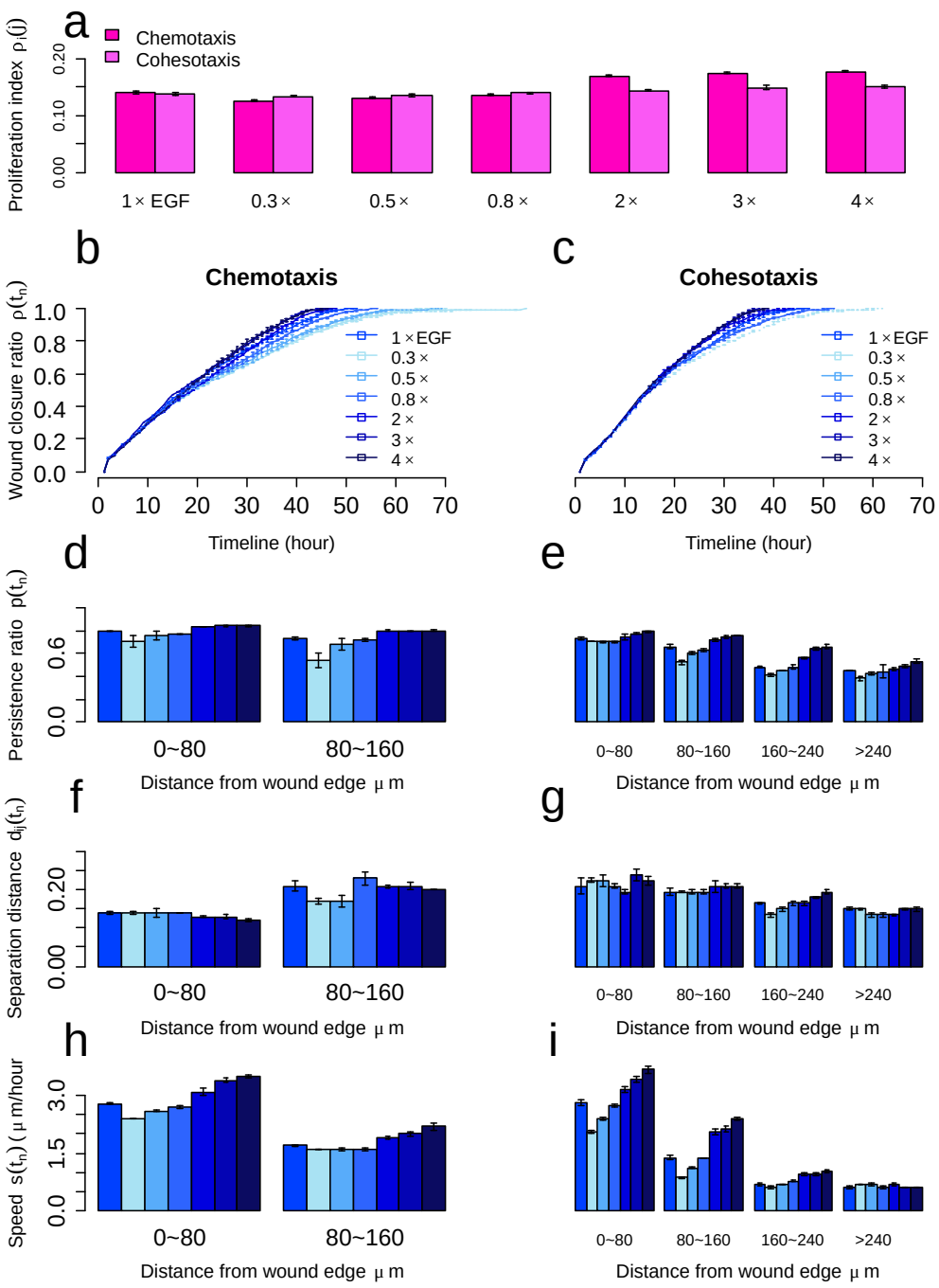

Figure 18. **Effects of altered EGF synthesis rates on efficiency of re-epithelialization under chemotaxis and cohesotaxis.** (a) The average keratinocyte proliferation index $\rho_i(j)$ during 13-48 hours with different EGF synthesis rates. (b–i) The wound closure ratio $\rho(t_n)$ over time (b, c), the persistence ratio $p(t_n)$ (d, e), the normalized separation distance $d_{i,j}(t_n)$ (f, g), and average migration speed $s(t_n)$ (h, i) of migrating keratinocytes during re-epithelialization with different EGF synthesis rates under chemotaxis and cohesotaxis. The error bars depict the standard deviations of three simulation runs.

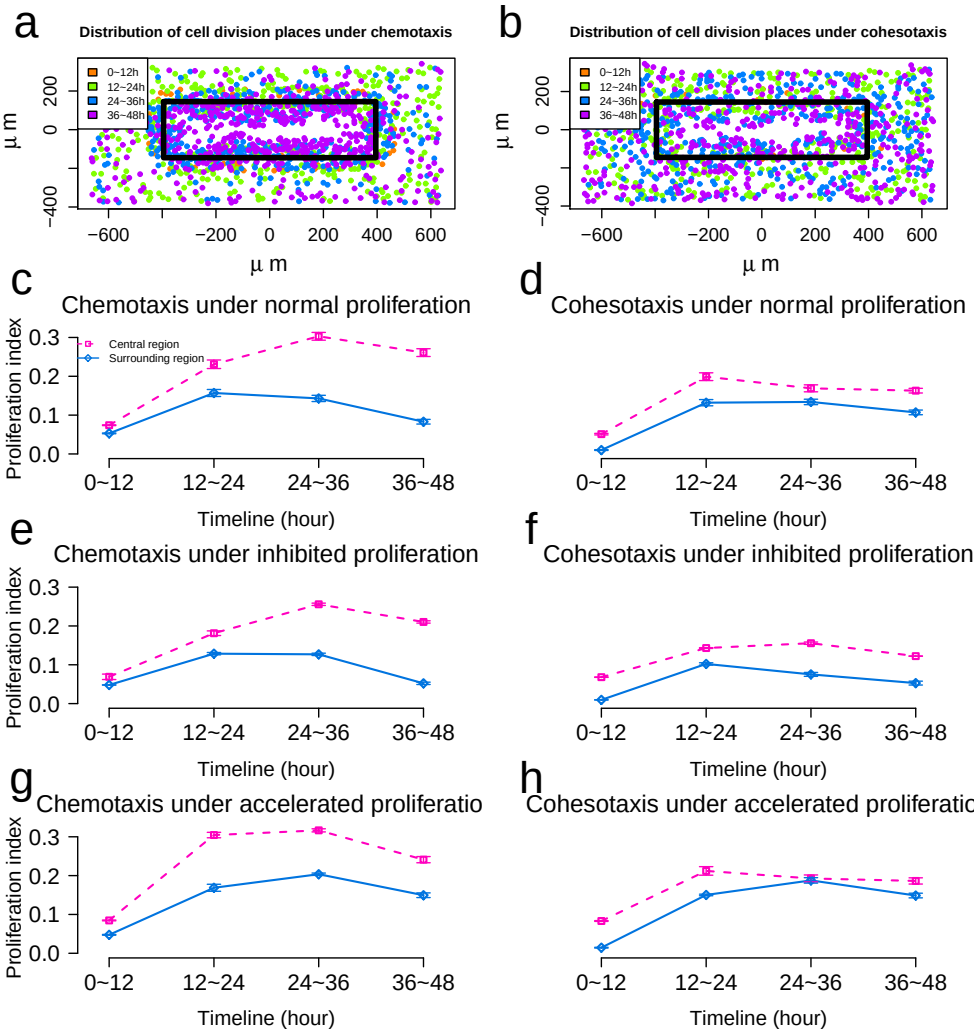

Figure 19. **Spatial-temporal patterns of keratinocyte proliferation under chemotaxis and cohesotaxis.** (a, b) Distributions of dividing keratinocytes under chemotaxis and cohesotaxis. Dividing cells are colored by division time. Orange: 0~12 hours, Green: 12~24 hours, Blue: 24~36 hours, Purple: 36~48 hours, and Black box indicates the initial wound edge. (c, e, g) The proliferation index $\rho_i(j)$ of the central region and the surrounding region over time under chemotaxis, with normal, inhibited (3× synthesis rate of TGF-β), and accelerated keratinocyte proliferation (0.3× synthesis rate of TGF-β), respectively. (d, f, h) The keratinocyte proliferation index $\rho_i(j)$ of the central region and the surrounding region over time under cohesotaxis, with normal, inhibited (3× synthesis rate of TGF-β), and accelerated keratinocyte proliferation (0.3× synthesis rate of TGF-β), respectively. The error bars depict the standard deviations of three simulation runs.

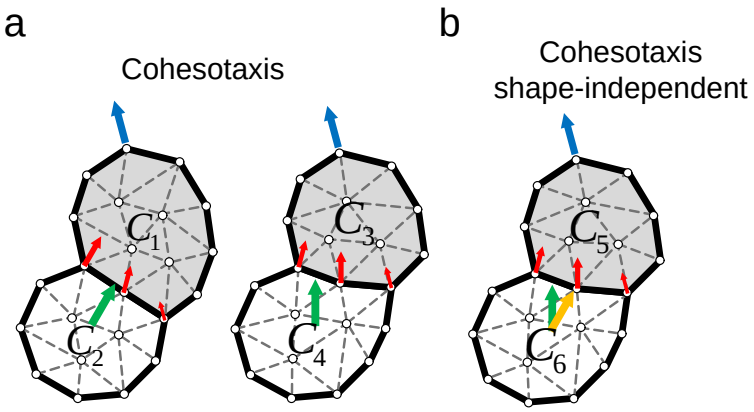

Figure 20. **Shape-independent cohesotaxis mechanism.** (a) The direction of contraction force vectors (red) generated by the migrating cell (direction shown in blue arrows) is shape-dependent. The migration direction (green arrows) of a cell is determined by the sum of contraction force vectors varies and depends on the cell-cell boundary shape because the cell-cell boundary shapes of C_1-C_2 and C_3-C_4 are different, so the migration directions of C_2 and C_4 are also different. (b) In the revised *shape-independent cohesotaxis* mechanism, the migration direction of a cell (yellow arrow) is determined by the vector from its center to the center of its migrating neighbor, which is independent of the shape of the contact surfaces.

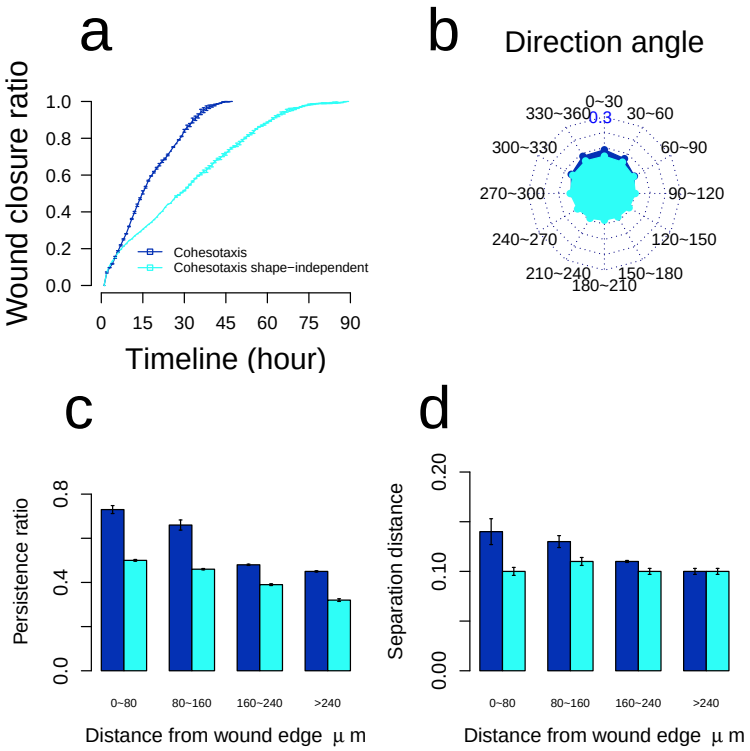

Figure 21. **Transmission of mechanical forces necessary for in-time re-epithelialization is cell-cell contact and cell-shape dependent.** (a) Wound closure ratio over time under the two cohesotaxis mechanisms. (b) The radar chart of the distribution of direction angle of migrating keratinocyte accumulated during the full process of re-epithelialization. The complete angle range (0°,360°) is divided into 12 intervals. Each spoke of the radar chart shows the proportion of direction angle within that specific interval. (c–d) The migration persistence and normalized separation distance of migrating keratinocyte under the two cohesotaxis mechanisms at varying distances from the wound edge during re-epithelialization. The error bars depict the standard deviations of three simulation runs.

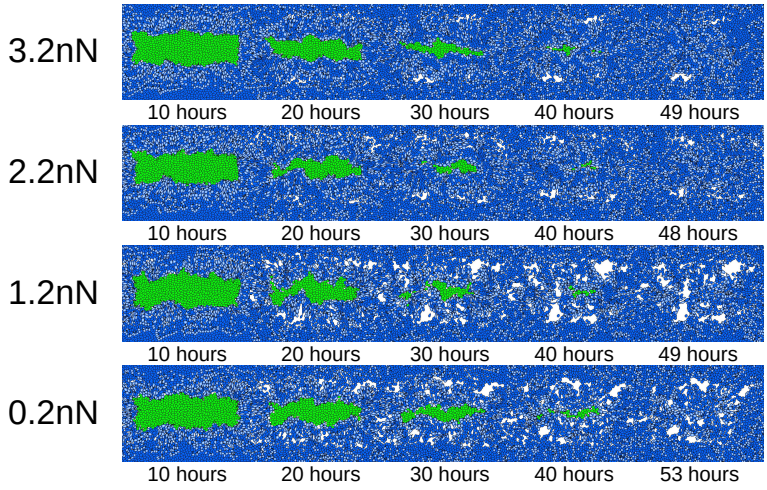

Figure 22. The snapshots of the wound tissue under decreased cell-cell adhesions at different time steps. Blue: keratinocyte; Green: wound; Light blue: migrating keratinocyte at that time step.

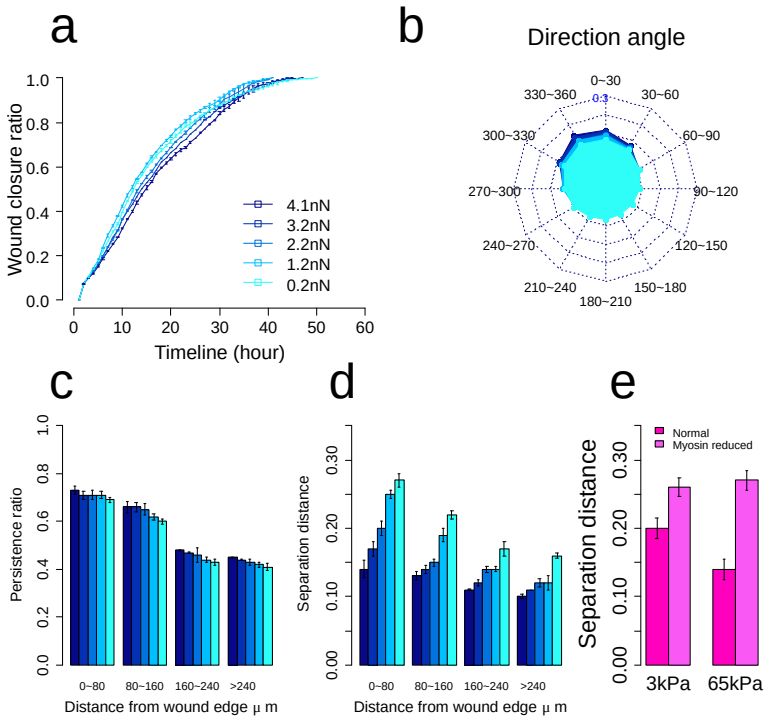

Figure 23. **Decreased cell-cell adhesion reduces cell-cell coordination.** (a) The wound closure ratio over time under decreased cell-cell adhesions. (b) The radar chart of the distribution of direction angle of migrating keratinocyte accumulated during the full process of re-epithelialization under decreased cell-cell adhesions. The complete angle range (0°,360°) is divided into 12 intervals. Each spoke of the radar chart shows the proportion of direction angle within that specific interval. (c–d) The migration persistence and normalized separation distance of migrating keratinocytes under decreased cell-cell adhesions at varying distances from the wound edge during re-epithelialization. The error bars depict the standard deviations of three simulation runs. (e) The normalized separation distance of epithelial cells under decreased cell-cell adhesion due to reduced myosin activity from the *in vitro* study is showed for comparison.

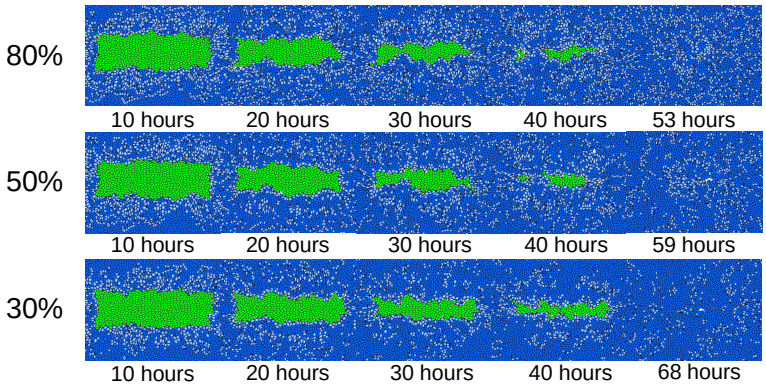

Figure 24. The snapshots of the wound tissue under inhibited signal transmission at different time steps. Blue: keratinocyte; Green: wound; Light blue: migrating keratinocyte at that time step.

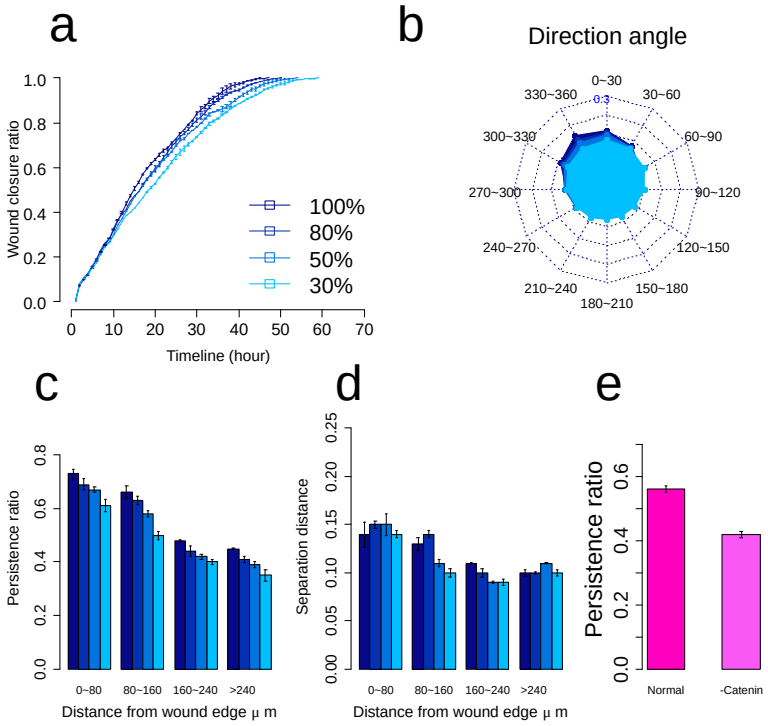

Figure 25. **Inhibition of mechanical signal transmission reduces migration persistence.** (a) The wound closure ratio over time under inhibited signal transmission. (b) The radar chart of the distribution of direction angle of migrating keratinocyte accumulated during the full process of re-epithelialization under inhibited signal transmission. The complete angle range (0°,360°) is divided into 12 intervals. Each spoke of the radar chart shows the proportion of direction angle within that specific interval. (c–d) The migration persistence and normalized separation distance of migrating keratinocytes under inhibited signal transmission at varying distances from the wound edge during re-epithelialization. The error bars depict the standard deviations of three simulation runs. (e) The migration persistence of epithelial cells under inhibited signal transmission due to depletion of αE-catenin from the *in vitro* study is showed for comparison.

CHAPTER 4

THE EFFECTS OF TGF-β SIGNALING ON THE SPATIO-TEMPORAL PATTERN FORMATION DURING TISSUE REGENERATION

4.1 Introduction

Effective skin wound healing is critical for human health as the skin provides the first barrier to the environment. Skin wound healing also provides a model for understanding mechanisms of many human diseases, such as cancer, in which some signaling pathways such as Wnt and Hedgehog are shared with wound healing (104). In addition, both wound healing and tumorigenesis are complex processes involving interactions among many different types of cells, extracellular matrices and diffusible mediators (104). Currently, many molecular and cellular regulatory mechanisms in skin wound healing are still not fully understood. We focus our study on the proliferation phase of skin wound healing. This phase consists of two different but overlapping processes: granulation tissue formation and re-epithelialization. During granulation tissue formation, fibroblasts are activated to synthesize and deposit ECM to fill up the wound space. During re-epithelialization, keratinocytes are activated and migrate over the ECM to close the wound and rebuild the skin barrier (105). TGF-β, an important cytokine in wound healing, has multiple roles in regulating behavior of different cells in the wound healing as well as in other biological processes (106). TGF-β is a potent inducer for the synthesis of the ECM components in fibroblasts during wound healing (107; 108). TGF-β can also stim-

ulate collagen production and matrix modulation (107), which are important for granulation tissue formation. However, TGF-β has a negative role in regulating epidermal proliferation in full-thickness wound healing. While it does facilitate keratinocyte migration by upregulating integrin expression (109), previous studies have shown that TGF-β is a potent inhibitor of epidermal proliferation (110; 111). Taken together, when wound healing processes involve both granulation tissue formation and epidermal re-epithelialization such as those in a full-thickness wound healing, it is often observed that TGF-β plays a positive role in stimulating granulation tissue formation (107; 108), but slows down the re-epithelialization and wound closure (110). Due to the complexity of wound healing process and multiple roles that TGF-β signal plays, the underlying control mechanism for the conflicting roles of TGF-β remains a puzzle. How these two roles can be balanced and regulated to achieve the goal of full-thickness skin wound healing, in which both dermis and epidermis need to be repaired, is incompletely understood. While most mechanistic findings in skin wound healing have been made through in vivo experimental studies, it has been challenging to develop adequate animal models. Many pathways involved in wound healing are essential to the viability of the animal, and mutations to these pathways are often lethal (106). It is also costly to make animal models, and difficult to uniquely perturb the system, which makes it challenging to decipher the complex control mechanisms of the skin wound healing process. Computational modeling of cells and tissues may help to reveal the underlying mechanisms in this complex cellular process.

Several computational models have been developed to study different aspects of this complex process. Reaction-diffusion-based models have been used extensively to study the dynamic

changes of cytokine and cells during wound healing processes. Sherratt and Murray have developed an epidermal wound healing model using the reaction-diffusion equation to study the role of mitosis (112). Haugh also developed a reaction-diffusion model to study receptor-mediated signal transduction and gradient sensing of fibroblasts in dermal wound healing (113). Recently, Menon *et al.* have developed a reaction-diffusion model to study the intercellular interactions between keratinocytes and fibroblasts mediated through cytokine diffusion during wound healing (64). Despite these successful studies, the reaction-diffusion equation based method does not model detailed cellular mechanics. As cells in reaction-diffusion models are treated as diffusible particles suspended in the ECM, the important roles of cellular mechanics in cell proliferation and migration are unaccounted for.

Another type of computational model focuses on the mechanical properties of cells and ECM during wound healing. Dallon *et al.* developed a hybrid approach to study ECM dynamics in wound healing and scar formation (114). In this model, cells are modeled as discrete particles, collagen fibers are modeled using a tensor representation, and cytokines are modeled using reaction-diffusion equation. Cumming *et al.* also used the hybrid modeling framework to study scarring during wound healing (115). Other continuity modeling methods include the mechano-chemical model developed by Murphy *et al.* for studying the interactions between ECM mechanical changes and growth factors (116).

To model detailed cell-cell mechanical interactions and their roles in determining complex cell behavior, more realistic cell models have been developed to analyze complex cellular processes during tissue development. Vertex models have been used to study Drosophila wing

epithelium development (117; 118) as well as wound healing (119; 120). Other modeling techniques include the cellular Potts model (121; 122), the subcellular finite element model (123; 58), and the dissipative particle dynamics simulation method for epithelialization (16). Although these models have been successfully applied to model different cellular processes, none of them can be used to realistically model massive cell migration, which involves extensive mechanical interactions and geometric changes between cells and matrices, and plays critical roles in skin wound healing process.

In this study, we applied dyCelFEM model to study the wound healing process. We first construct intracellular gene regulatory networks to stochastically determine the cell behaviors including growth, division, apoptosis, and migration for each individual keratinocyte and fibroblast. These networks are embedded in each individual cell. We also incorporate intercellular communication via the diffusion of major soluble mediators (PDGF, KGF, and TGF-β) in the ECM and fibrin clot. We build a computational model of the cross-section of a skin tissue. Excisional wounds were created on the *in silico* skin, and the healing processes were simulated. By dynamically tracking behaviors, positions, spatial configurations of cells, and spatial distributions of different mediators over time, we are able to correctly reproduce the formation of granulation tissue and re-epithelialization during wound healing. We then study the effect of TGF-β on dermal and epidermal pattern formation during wound healing. Combining computational simulations and experimental observations, our results suggest a novel mechanism for the inhibition of keratinocyte proliferation and re-epithelialization by TGF-β. Our results suggest that TGF-β can attenuate the strength of PDGF and KGF signals that fibroblasts

and keratinocytes receive by promoting ECM synthesis and deposition. In analogy to electrical circuits, the ECM acts as a resistor for PDGF and KGF signals, and the TGF-β act as a potentiometer that can change the resistivity of the resistor, therefore indirectly regulate the signal patterns and cell behavior. This study exhibits the potential of our method in helping to gain new understanding of the control mechanisms of important multi-cellular processes.

4.2 Tissue regeneration model

4.2.1 Cell, Matrix, and Diffusion Mediators

The simplified model to study skin wound healing include two types of cells, namely keratinocyte and fibroblast. It also includes the ECM and fibrin clot. There are three diffusible mediators: PDGF, KGF, and TGF-β. They are the major factors responsible for intercellular communications.

ECM and fibrin clot. The ECM is the major component in skin dermis. After the infliction of the injury, fibroblast synthesize new collagen to reconstruct the ECM (105). The fibrin clot is a loose matrix formed during blood clot formation at the beginning of wound healing. It provides the matrix for fibroblasts and keratinocytes to migrate into the wound bed. Both the ECM and the fibrin clot act as reservoirs for diffusion mediators, and as a medium allowing cytokines to diffuse and form chemotactic gradients. In our model, the ECM and the fibrin clot are discretized and modeled as virtual cell with elasticity properties. They can be destroyed by the migrating cells and by proteinases released from fibroblasts (124; 125). The fibrin clot can also be destroyed or by proteinases released from both migrating fibroblasts and keratinocytes, and the ECM can be degraded by fibroblasts as a path is cleared for cell

migration (124). ECM can also be synthesized by activated fibroblasts (105), while the fibrin clot can only be degraded.

Fibroblast. Fibroblasts are located in the dermal layer of human skin and play important roles in maintaining skin tissue homeostasis during development. During wound healing, fibroblasts synthesize most of the new ECM and rebuild the damaged dermal connective tissue within wound (105). Fibroblast can be activated by the PDGF released from the platelets in the fibrin clot (108) and subsequently migrate through ECM following the PDGF gradient. In our model, fibroblasts secret MMPs to degrade the ECM and fibrin clot along their path (125).

Keratinocyte. Skin epidermis is composed of keratinocytes. Tight junctions between keratinocytes form the skin epidermal barrier (126). We model the proliferative layer of keratinocytes, which are assumed to be able to proliferate and migrate during the re-epithelialization process. The proliferation and migration of keratinocytes are activated by KGF (108). Upon activation by KGF, keratinocytes migrate following the KGF gradient, but can only migrate laterally over ECM (127). If there is no ECM in its migration direction, keratinocyte will not migrate even if it has been activated by KGF. We assume that keratinocytes secrete the necessary MMPs to break down the fibrin clot along its migration path (128).

We model the cross-section of wounded skin tissue (Figure 26). We constructed the layered structure of the tissue by assigning different cell types at different depths of skin. At the very top of the tissue is the layer of epidermis consisting of proliferative keratinocytes (blue in Figure 26). Below the epidermal layer, the ECM (gray in Figure 26) is the major part of the skin dermis, in which fibroblasts (red in Figure 26) are uniformly distributed and occupy about

10% of total space in dermis. Further below the dermis lies the hypodermal cells (dark gray in Figure 26), which only play mechanical supporting roles, but do not participate in wound healing simulation. We assume the average cell size as 20 μm in diameter (129; 130). And we create a *in silico* wound tissue with the wound area of 0.4 mm wide and 0.38 mm deep in the tissue (green in Figure 26).

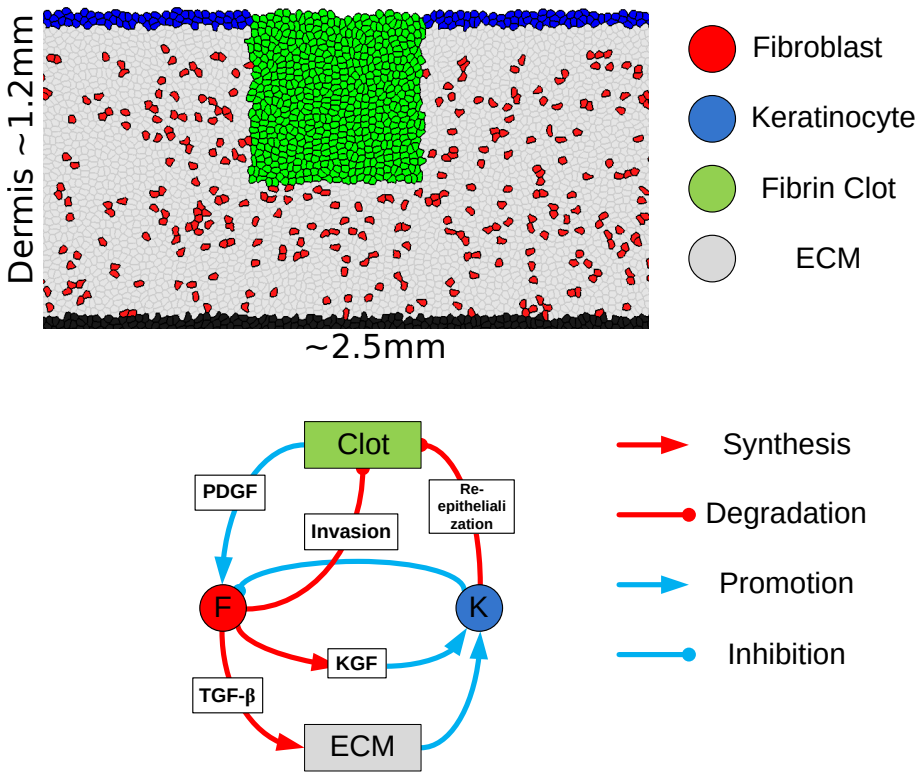

Figure 26. **Tissue model and intercellular signaling network embedded in each cell.** (a) Side view of the skin wound tissue. Blue: Keratinocyte; Green: Fibrin clot; Red: Fibroblast; Gray: ECM. (b) Schematic of the intercellular signaling network.

4.2.2 Intracellular genetic circuits controlling cell behavior

Cell behavior control. We explicitly model the behaviors of each keratinocyte and fibroblast in response to the intercellular signals. The four behavior types include: proliferation, migration, apoptosis, and quiescence. The potentials for keratinocyte and fibroblast to proliferate and migrate are activated by KGF and PDGF, respectively, using Hill equations (Table IV). The proliferation and migration of keratinocytes are activated by KGF with Hill coefficients $g_{GD} = g_M = 1$, and dissociation parameters $K_K^{GD} = K_K^M = 100$, respectively. We assume maximum potentials for proliferation and migration of keratinocyte are $\hat{q}_{GD} = 0.1$ and $\hat{q}_M = 40$, respectively, so that keratinocytes prefer migration to proliferation upon activation. As apoptosis and quiescence are not the focus of this study, we assume a constant potential $q_A = 0.001$ for apoptosis, and $q_Q = 1.0$ for cell quiescence. In case of no extracellular KGF signaling, keratinocyte behavior is dominantly quiescent due to the large q_Q value. But when KGF concentration is large enough, the proliferation and migration will have larger weight. After obtaining the potentials for all four cell behaviors, we calculate the probabilities by normalizing them: $p_1 = p_{GD} = q_{GD}/Z$, $p_2 = p_M = q_M/Z$, $p_3 = p_A = q_A/Z$, and $p_4 = p_Q = q_Q/Z$, where $Z = q_{GD} + q_M + q_A + q_Q$. A Monte Carlo sampling step is implemented to stochastically select the cell behavior based on these probabilities. Specifically, a uniform random number $\mu \in [0, 1]$ is generated at each step, and the cell behavior is determined by the minimum value of $b = 1, 2, 3, 4$ satisfying the inequality: $\sum_{i=1}^{b-1} p_i < \mu \leq \sum_{i=1}^{b}$, in which values of b matches cell behaviors as $b = 1$ for proliferation (growth/division); $b = 2$ for migration; $b = 3$ for apoptosis; and $b = 4$ for quiescence, respectively.

Cell behaviors of fibroblast are similarly controlled using Hill equations (Table IV). The proliferation and migration of fibroblasts are activated by PDGF with Hill coefficients $h_{GD} = 2.0$ and $h_M = 3.0$, and dissociation parameters $K_F^{GD} = 100$ and $K_F^M = 10,000$, respectively. We assume maximum potentials for proliferation and migration of fibroblasts are $\hat{f}_{GD} = 0.05$ and $\hat{f}_M = 1.0$, respectively, so fibroblasts also prefer migration to proliferation upon activation. We also assume a constant potential $f_A = 0.001$ for apoptosis, and $f_Q = 1.0$ for cell quiescence. In case of no extracellular PDGF signaling, fibroblast behavior is also dominantly quiescent due to the large f_Q value. But when PDGF concentration is sufficiently large, the proliferation and migration will have larger weight. After obtaining the potentials, we use the same Monte Carlo approach to stochastically select cell behavior for fibroblasts.

Fibroblast and keratinocyte can not only proliferate and migrate, they can also synthesize and release signaling molecules into the extracellular space to affect the behavior of cells in distance. In this study, we explicitly model the synthesis and degradation reactions of cytokines, as well as the maturation of collagen fibers from procollagen subunits.

PDGF. PDGF is a potent mitogen for fibroblast (131). It also forms a gradient to provide directional cue for fibroblast to migrate (108). PDGF is released from the degranulated platelets inside the fibrin clot (108). At the early stage of wound healing, platelets degranulate and release PDGF, which diffuse through the fibrin clot and ECM to form a PDGF gradient to direct fibroblast migration. Here, we assume that platelets are uniformly distributed in the fibrin clot. As each platelet contains only a fixed amount of PDGF, it can be depleted quickly long before wound is healed.

KGF. KGF is the major growth factor to activate keratinocyte proliferation and migration (108). KGF is mostly released from fibroblast (131), and reaches the epidermis by diffusion to activate keratinocytes. In our model, we assume the synthesis of KGF from fibroblasts are activated by PDGF.

TGF-β. TGF-β has a strong fibrotic role in wound healing (108). It can activate fibroblasts to synthesize a large amount of collagen, the major component of ECM. While TGF-β can be synthesized from multiple sources, including macrophages and fibroblast, most TGF-β is stored in its latent form (132) in the ECM, and becomes activated by MMP carried on fibroblast surfaces (132). Therefore, we modeled active form of TGF-β as generated by PDGF-activated fibroblast.

Procollagen and collagen. Collagen fiber is the major component in the ECM. A key outcome in dermal wound healing is the recovery of the lost mass and structure of the dermal connective tissue by generating new collagen (133). Here, collagen is modeled to be synthesized in two steps from fibroblasts. Activated fibroblast first synthesize and release procollagen, which are then modified and assembled outside of the cell to form mature collagen fibers. The synthesis of procollagen from fibroblast is activated by TGF-β.

4.2.3 Intercellular signaling network

Wound healing requires proper spatio-temporal coordination of behavior of multiple different cell types. Intercellular communication through diffusible cytokines play critical roles in this complex process. We adopt a simplified model that take three key growth factors to represent a spectrum of cytokines in this communication network (Figure 26). Specifically, PDGF released

from platelets and macrophages in the fibrin clot diffuses through the ECM and fibrin clot to form a gradient for activating and recruiting fibroblasts into wound. Activated fibroblasts in turn release KGF and TGF-β, both diffuse through the ECM and the fibrin clot. TGF-β can activate the production of collagen from fibroblast to form granulation tissue and rebuild the ECM. KGF can activate keratinocyte to proliferate and migrate over newly formed granulation tissue to cover the wound. Along the progression of wound healing, the signaling loop of diffusible mediators is gradually attenuated, and eventually turned off when wound is completely healed.

Intercellular communication depends on diffusion of cytokines through the ECM and fibrin clot. Growth factors such as PDGF, KGF, and TGF-β diffuse about two orders of magnitude slower in the ECM than in a solution environment (134), due to the large amount of nonspecific binding and unbinding reactions between growth factors and ECM molecules. We adjust the diffusion coefficients of PDGF, KGF, and TGF-β as shown in Table V. We assume procollagen diffuses much slower than cytokines due to the differences in their molecular weights and structures.

4.2.4 Multi-scale spatio-temporal cell model for tissue regeneration

The tissue regeneration process during wound healing involves cellular processes occurring in multiple spatial and temporal scales. We endow each cell has its own reaction circuits, which makes autonomous cellular decisions based on surrounding environmental diffusing signals. In this study, we integrate intracellular regulatory networks and intercellular signaling networks in a unified model to study the skin wound healing process.

Step 1. Reaction and diffusion. The first step of the integrated modeling is to model the reaction networks in each cell and the following process of molecular diffusion within the tissue. This step is achieved by solving the corresponding differential equations governing cytokine concentration over time as the result of synthesis, degradation, and diffusion. See 3.2.3 for more details of numerical way of solving these differential equations.

Step 2. Stochastically determine the cell behavior. Based on the concentration of cytokines in each cell , the behavior of each keratinocyte and fibroblast is determined stochastically by taking a Monte Carlo sampling step based on the probabilities calculated from the control circuits (mentioned in 4.2.2).

Step 3. Perform the cell motion. For each cell in the tissue, we physically perform the cell behavior determined in Step 2 using the DYCELFEM model. With the solution of the displacement vector of cell positions in response to the behaviors, we can update the spatial position of each cell in the tissue (See more details in 2.3). One iteration of the simulation of the tissue regeneration model is therefore finished. The model goes back to Step 1 to start the next iteration.

4.3 Results

4.3.1 Normal tissue regeneration process

We first study the normal tissue regeneration process using our model. We run 10 independent simulations starting from the same initial wounded tissue shown in Figure 26. Each simulation runs 300 iterations, and each iteration corresponds to 1 hour of biological time, therefore we observed about 12 days for each process of tissue regeneration.

TABLE IV

Cell behavior control.

Fibroblast behavior control			
Cell behavior	Potential	Parameters	Ref.
Proliferation	$f_{GD} = 0.01 + \frac{\hat{f}_{GD} PDGF^{h_{GD}}}{K_F^{GD} + PDGF^{h_{GD}}}$	$\hat{f}_{GD} = 0.05, h_{GD} = 2.0, K_F^{GD} = 100$	This study
Migration	$f_M = 0.01 + \frac{\hat{f}_M PDGF^{h_M}}{K_F^M + PDGF^{h_M}}$	$\hat{f}_M = 1.0, h_M = 3.0, K_F^M = 10000$	This study
Apoptosis	$f_A = 0.001$		This study
Quiescence	$f_Q = 1.0$		This study
Keratinocyte behavior control			
Cell behavior	Potential	Parameters	Ref.
Proliferation	$q_{GD} = 0.001 + \frac{\hat{q}_{GD} KGF^{g_{GD}}}{K_K^{GD} + KGF^{g_{GD}}}$	$\hat{q}_{GD} = 0.1, g_{GD} = 1, K_K^{GD} = 100$	This study
Migration	$q_M = 0.01 + \frac{\hat{q}_M KGF^{g_M}}{K_K^M + PDGF^{g_M}}$	$\hat{q}_M = 40, g_M = 1, K_K^M = 100$	This study
Apopotosis	$q_A = 0.001$		This study
Quiescence	$q_Q = 1.0$		This study

Spatial pattern of the tissue. As shown in Figure 27, the only conditions that keratinocytes need to migrate are ECM and KGF gradient (Figure 27i–l), they start to migrate before granulation tissue is fully formed in the wound space (Figure 27a–d). Therefore, as shown in Figure 27a–d, the keratinocytes are typically migrating and invading the wound space from a position below the wound surface (Figure 28A and B). The simulation results show that the migrating epidermal keratinocytes form a continuous thin sheet of migrating tongue (blue cells in Figure 27a–d and Figure 28A) invading into the fibrin clot (green elements in Figure 27a–d). The epidermal tongue migrates below the top layer of fibrin clot and over the newly formed

ECM elements (granulation tissue) (Figure 28A and B), until the both sides of epidermis merge and the wound closes. The structure of migrating epidermal tongue, and its location under the fibrin clot, has been consistently observed in histological analysis of skin wound healing as shown in Figure 28B. At day 10 post wound, the wound in both computational simulation and *in vivo* skin wound healing experiment have closed (Figure 28C and D). The consistency of the model with *in vivo* experimental observations shows that the major cellular mechanical mechanisms underlying keratinocyte migrations and interactions with ECM and fibrin clot have been correctly encoded in our model.

To analyze the rate of wound healing in our simulations, we calculate the wound sizes at different time points as the distance between the two edges of migrating epidermal tongues at both sides of the wound (red arrows in Figure 27a–c). The wound sizes from 10 simulations of normal tissue regeneration process are shown in Figure 29B. The size of wound continuously decrease from the 400μm at day 0 to 0μm at about day 5 when the wound is closed. The stochastic cell behavior control and reaction noises introduced in wound healing simulation do not affect the wound healing rate significantly. The standard deviation of wound healing time is about 1 day (Figure 29B).

Fibroblasts are synthesizing new procollagen at the same time of migration through the ECM and fibrin clots following PDGF gradient (Figure 27e–h). We assume procollagen molecules are released from the rear side of fibroblasts, then form new ECM elements behind migrating fibroblasts (Figure 27a–d). Interestingly, our results in Figure 27e–h show that although the PDGF gradient is uniform in all directions, the migrating fibroblasts and newly formed ECM

are forming bud-like clustering structures when invading into wound space (Figure 27b and c), instead of uniformly growing from all directions.

To analyze how the wound space is filled up with different cell types and matrix elements over the wound healing process, we calculate the evolution of the total volumes of each different component in the wound space over time, as shown in Figure 29D. We only analyze volume changes within the wound space, which is shown with the black boxes in Figure 27a–d. The results show that volumes of all three major components, ECM, fibroblasts, and keratinocytes, are increasing over time (Figure 27D). The volumes of these components reach the equilibrium at about day 5 post wound, and the original major component fibrin clot in wound bed has been replaced by mostly new ECM in the healed wound. The composition and spatial pattern of these three major components in the healed wound space is similar to unwounded skin, in which epidermal barrier is rebuilt with keratinocytes and dermis is filled up with newly synthesized collagen scattered with fibroblasts (Figure 27d).

Cell proliferation plays an important role in both granulation tissue formation and re-epithelialization. To analyze cell proliferation pattern, we calculate the numbers of proliferating keratinocytes (blue cells in Figure 27a–d) and fibroblasts (red cells in Figure 27a-d) in the whole tissue at different time. The results are shown in Figure 29C. Due to the early PDGF signal, fibroblasts (red line in Figure 29C) are activated to proliferate earlier than keratinocytes (blue line in Figure 29C). Fibroblast proliferation keeps decreasing along with the wound healing process (red lines in Figure 29C). And keratinocyte proliferation is upregulated and reaches the peak at about day 3 post wound, and then starts to decrease (blue lines in Figure 29C).

Spatio-temporal distribution of cytokines. The temporal dynamics of all three major cytokines (PDGF, KGF, and TGF-β) have been shown in Figure 29A as red, blue, and yellow lines, respectively. Consistent with the snapshots of spatio-temporal distributions shown in Figure 27, the PDGF is the earliest signal in the system, which decays over time (red line in Figure 29A). Upon injury, the KGF signal is quickly upregulated by PDGF due to fibroblast activation, and the highest KGF amount in the tissue appears quickly at about 10 hours post wound (blue line in Figure 29A). But interestingly, the peak of keratinocyte proliferation does not come until about day 3 post wound (blue line in Figure 29C). The amount of fibrin clot decreases along with wound healing progress.

We experimentally verified the temporal dynamics of TGF-β and collagen in our model by comparing it to expression data from gene array analysis of TGF-β1, type I and III collagen in a 1mm mouse skin excisional wound (135). The temporal dynamics are shown in Figure 29E. This experimental data shows patterns consistent with results from our computer simulations of wound healing (yellow and gray lines in Figure 29A). The TGF-β densities in both computer simulation and gene array analysis peak at about day 1, and then decrease back to the near pre-wound level at about day 3 (Figure 29A and E). The collagen levels in both *in silico* and gene array analysis show a consistent increase, and both reach the steady level at about day 4 post wound (Figure 29A and E). The consistency between our modeling results and gene array analysis exhibits the predictive power of our model.

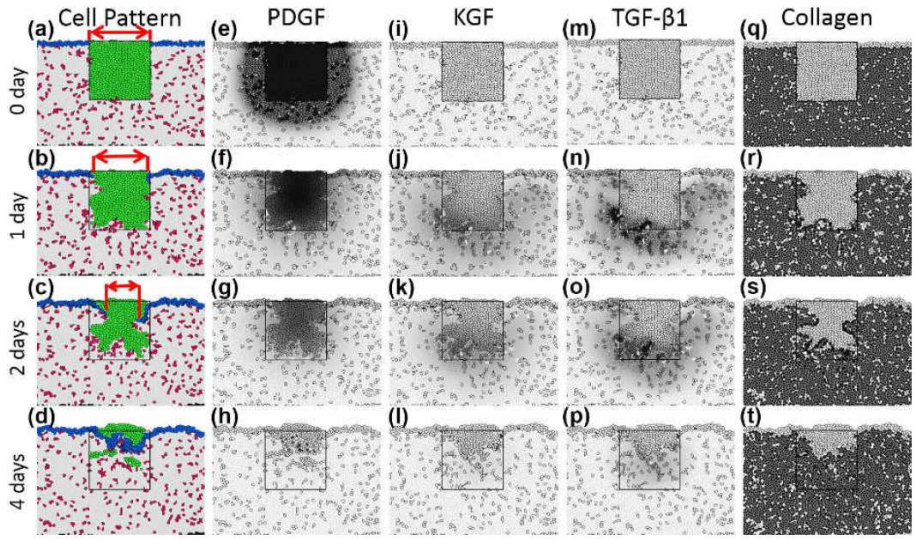

Figure 27. **Spatio-temporal pattern of cells and cytokines in normal tissue regeneration process. Each row shows snapshots at four different time points: at 0, 1, 2, and 4 days post wound, respectively.** (a–d) The cell patterns at different time of simulation. (e–h) The spatio-temporal pattern of PDGF distribution in the tissue. (i–l) The spatio-temporal pattern of KGF distribution in the tissue. (m–p) The spatio-temporal pattern of TGF-β distribution in the tissue. (q–t) The spatio-temporal pattern of collagen distribution in the tissue. The darkness indicates the concentration level of cytokines in the cell.

4.3.2 Spatial mechanism of TGF-β on epidermal proliferation

Proper skin wound healing not only requires proliferation and migration of cells, but also deposition of large amount of ECM. TGF-β has been shown to play important roles in regulating both cell behaviors and ECM synthesis during wound healing (108). And all these dynamic processes usually span large spatial scales, which may significantly affect cell behavior and wound healing outcomes. Most previous studies focused on the effects of TGF-β through the regulation of TGF-β signaling pathway (136; 137), while the effects of spatial distributions of

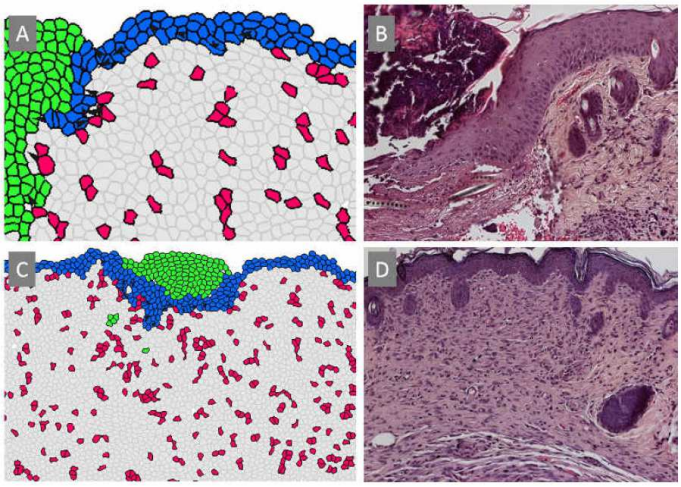

Figure 28. **Spatial pattern of the tissue comparing to histological imaging of normal skin wound healing at day 3 and day 10 post wound.** (A) and (B) show spatial pattern of the tissue from computational simulation (A) and histological imaging of mice skin wound healing model (B) at day 3 post wound. The epidermal layer migrating under the fibrin clot simulated in computational model can also be clearly seen in the experimental histological imaging (B). (C) and (D) show spatial pattern of tissue from computational simulation (C) and histological imaging (D) at day 10 post wound.

cytokines throughout the wound tissue, and the role of ECM in forming the spatial distributions are still largely unknown.

Changing TGF-β synthesis rate significantly alters tissue patterns. We first change the synthesis rate of TGF-β from fibroblast, and study its overall effects on tissue patterns and wound healing processes. And we compare the spatial distribution of TGF-β signal in the wound tissues in different times; we also compare the cellular patterns of healed wounds, temporal dynamics of fibroblasts, keratinocytes, and ECM in wound area, as well as the wound healing rates. The results from 10 times downregulated (from wild type), the wild type, and

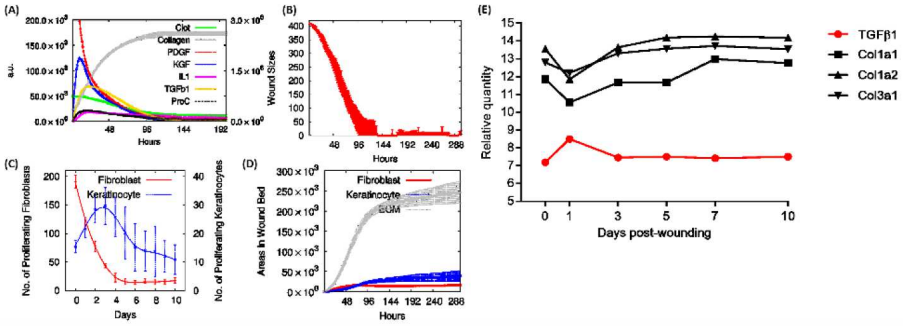

Figure 29. **Temporal pattern of cells and cytokines in normal tissue regeneration process. All mean curves and standard deviations are calculated from 10 runs of simulations.** (A) Dynamic of temporal patterns of the total amount of cytokines (PDGF, KGF, and TGF-β), Procollagen and Collagen, and fibrin clot in the whole tissue. (B) Dynamic of temporal pattern of wound size. It is calculated as the distance between the two migrating tongues at both sides of wound (red lines in Figure 27a–c). (C) Temporal dynamic of number of proliferating keratinocytes (blue) and fibroblasts (red) in the whole tissue. (D) Temporal dynamic of the total volume (area) of each component (keratinocyte, fibroblast, and ECM) in wound space, which is shown with the black boxes in Figure 27. (E) Temporal gene array analysis for both TGF-β and type I and III collagen expressions in a 1 mm mouse skin excisional wound, which show consistent temporal patterns with the temporal dynamics of TGF-β and collagen in our simulation results in (A).

5 times upregulated synthesis rates of TGF-β are shown in Figure 30a–f, Figure 30g–l, and Figure 30m–r, respectively. Figure 30a–c, Figure 30g–i, and Figure 30m–o show the spatial distributions of TGF-β signal at day 1, 2, and 4 post wound in three different TGF-β regulations, respectively. The gray density of each element in the tissue visualizes the corresponding concentration of TGF-β in that element. In comparisons with the normal wild type wound healing case (Figure 30g–i), the results from downregulated TGF-β synthesis have shown significantly reduced signal density in the spatial distributions of TGF-β in the wound tissue (Figure 30a–c), while upregulated TGF-β synthesis has shown significantly increased signal in wound tissue

(Figure 30m–o). In the case of upregulated TGF-β synthesis, both signal strength and the area of coverage are increased (Figure 30m–o). Figure 30d, Figure 30j, and Figure 30p show the tissue patterns of three different TGF-β synthesis rates at day 10 post wound. The black box indicates the area where the initial wound was located. Compared with the wild type wound healing shown in Figure 30j, the dermal repair is significantly compromised in wound healing of downregulated TGF-β, and at the same time the epidermis exhibits hyper-proliferation (Figure 30d). The result is a healed skin wound tissue with hyper-plastic epidermis and largely unrepaired dermis. With increased TGF-β synthesis rate, more ECM is synthesized and deposited into the dermis (Figure 30j and p). In the normal case, both dermal and epidermal volume at 10 days post wound have been recovered to near the pre-wound level. The epidermis in normally healed wound consists of a thin layer of keratinocytes (Figure 30j), similar to the unwounded skin. In the case of upregulated TGF-β, a large amount of ECM is generated in the dermis (Figure 30p), so that the total ECM volume has exceeded that in the unwounded skin (black box in Figure 30p), and at the same time the epidermis is not closed (Figure 30r), because keratinocytes have not sufficiently proliferated (blue lines in Figure 30q) to cover the over-grown granulation tissue.

The tissue regeneration process mainly involves interplay among three major components: fibroblasts, keratinocytes and ECM, as shown in Figure 30e, Figure 30k, and Figure 30q. In normal case, the ECM (the granulation tissue) occupies the most volume in healed wound space, with a thin layer of keratinocytes (re-epithelialized epidermis) on the top of it, and fibroblasts scattered inside it (Figure 30k), which is a configuration close to the composition and structure

of intact skin. However, in abnormal cases, this balance can be disrupted. Hyper-proliferation of keratinocytes and inadequately generated ECM may cause epidermal hyperplasia (138) and compromised dermal repair (Figure 30e). Over-growth of ECM and inhibited keratinocyte proliferation may result in a hyper-trophic scar (139) or unhealed wound (Figure 30q).

The results in Figure 30 show that changes in TGF-β synthesis can dramatically change tissue pattern formation during wound healing without disruptions to the intracellular TGF-β signaling pathways in keratinocytes and fibroblasts. These results suggest that there might be a novel mechanism of behavioral regulation among fibroblasts, keratinocytes, and ECM by TGF-β.

Upregulating TGF-β decreases signal strength and cell activities. In addition to spatial patterns, temporal dynamics of PDGF and KGF also play important roles in regulating cell behaviors. To study how TGF-β can regulate the temporal dynamics of both PDGF and KGF signals during wound healing, we compute (1) the total PDGF and KGF signals in the wound tissue at each time step (Figure 31a and d), (2) the total PDGF and KGF signals that actually reach the target fibroblast and keratinocyte cells at each step (Figure 31b and e), and (3) we correlate the temporal dynamics of PDGF and KGF with dynamics of cell proliferation (Figure 31c and f). The temporal dynamics of the total PDGF and KGF in whole tissue in Figure 31a and d show that both PDGF and KGF concentrations are inversely regulated by TGF-β synthesis rate. When TGF-β is downregulated, the PDGF and KGF concentrations are increased during the time period from day 1 to day 5 post wound, however, when TGF-β

is upregulated, the PDGF and KGF concentrations are decreased during the same time period. Especially, KGF levels are more significantly affected by TGF-β than PDGF does (Figure 31d).

To more specifically correlate the PDGF and KGF dynamics to cell behavior, we further compute the signal strengths that fibroblasts and keratinocytes receives at each time step. Basically, we compute the total local concentration of PDGF and KGF for all fibroblasts and keratinocytes. The results are shown in Figure 31b and e, respectively. Both signals are still inversely regulated by TGF-β, however, the local signal differences are even sharper between different TGF-β regulations, compared with the global signal strengths. Particularly, the KGF signal that keratinocytes receive have been dramatically upregulated in the tissue of downregulated TGF-β (Figure 31e). To determine whether the PDGF and KGF signals are the major driving force for cell proliferation of fibroblasts and keratinocytes, we compute the number of proliferating fibroblasts and keratinocytes at each time point, as shown in Figure 31c and f. The temporal dynamics of fibroblast and keratinocyte proliferation are consistent with the temporal dynamics of PDGF and KGF signals in the local environment of cells (Figure 31b and e), but they do not match the TGF-β dynamics shown in Figure 32a. This is consistent with literature and our model setting that cell proliferation are directly regulated by PDGF and KGF, rather than TGF-β. TGF-β only affects cell behavior by regulating PDGF and KGF signals.

We have shown that both spatial and temporal dynamics of PDGF and KGF can be dramatically regulated by TGF-β synthesis rates. However, TGF-β does not directly regulate PDGF and KGF synthesis in our model. The only component that TGF-β directly regulate is the collagen. Taken together, our results suggest that TGF-β might regulate signal patterns of

PDGF and KGF by regulating ECM density. Therefore, we hypothesize that TGF-β regulates PDGF and KGF signal strengths by changing ECM density and mass in the wound tissue.

Upregulating TGF-β increases distances between cells. To test our hypothesis, we compute the average distances between fibroblasts to their nearest fibrin clots (Figure 32c), and the average distances between keratinocytes to their nearest fibroblasts (Figure 32d), at each time step during the wound healing of three different TGF-β regulations. The distances between fibroblasts and fibrin clots indicate how far the PDGF signals released from fibrin clots have to be transported to reach a fibroblast, and the distances between keratinocytes and fibroblasts indicate how far the KGF signals released from fibroblasts have to be transported before reaching a keratinocyte. If these distances are changed, the strength of signals that cells receive will be changed as well, because the concentrations of cytokines in the local environment of fibroblasts and keratinocytes are inversely related to the diffusion distances from the sources of signaling molecules.

Figure 32c show that the distances between fibroblasts and the fibrin clots is increased when TGF-β is upregulated, and the distances are decreased when TGF-β is downregulated. The same pattern can be observed in the distances between keratinocytes and fibroblasts in Figure 32d. These results show that due to the upregulation of TGF-β (Figure 32a), the ECM production is significantly upregulated (Figure 32b), and therefore, fibroblast and keratinocyte cells surrounded by these newly synthesized ECM can be significantly dispersed in the wound space, which increases the diffusion distances among them. And this effectively attenuates the signal strengths that fibroblasts and keratinocytes eventually receive.

4.4 Conclusion and discussion

Human skin wound healing is a complex cellular process involving fine regulation of behaviors of different types of cells, the synthesis of diffusible mediators and matrix components. TGF-β, as an important cytokine during wound healing, plays critical but conflicting roles during this process. In this study, we applied dyCelFEM to realistically simulate the wound healing process, and help to reveal the control mechanism and understand the role of TGF-β in granulation tissue formation and re-epithelialization.

To realistically control cell behaviors in wound healing, we explicitly model the potentials of four different cell behaviors, namely proliferation (growth and division), migration, apoptosis and quiescence, for each keratinocyte and fibroblast in response to intercellular signals using Hill equations. A Monte Carlo sampling step is implemented to stochastically select the cell behavior based on these potentials. We model the synthesis and degradation of three major growth factors, including PDGF, KGF and TGF-β, to represent the spectrum of important cytokines in wound healing. We model the synthesis of collagen from fibroblasts. We use the differential equation to model chemical reactions occurring in each cell. And we model the diffusion processes of all diffusible mediators through the ECM and fibrin clot based on the finite element mesh, so that the intercellular communication among cells can be constructed. We integrate these different processes using different modeling methods in a unified model to simulate human skin wound healing process. We iteratively perform wound healing cell model in four steps: (1) model intracellular reactions using chemical differential equations, (2) model intercellular communication network using diffusion equation, (3) determine cell behavior

stochastically according to state and local environment of each cell, and (4) perform the cell behavior using the dyCelFEM method. We run 10 cell simulations for each set of wound healing parameter, and collect all intermediate data of cell positions, cytokine concentrations and distributions, cell proliferation and migration states for analysis.

Our results suggest a novel mechanism that TGF-β may indirectly regulate cell behaviors by increasing ECM synthesis rate. By considering the intercellular communication in wound healing as a signal transmission process, and the matrix (ECM and fibrin clot) as the signal carrier, we analyze how TGF-β regulates the wound healing progress by changing the density of the extracellular matrix. All signals such as PDGF, KGF and TGF-β need to diffuse through the wound bed, a space filled with ECM and the fibrin clot, to reach and act on their targets fibroblasts and keratinocytes. Our results show that the strength of signals that fibroblasts and keratinocytes can receive from their local environment can be attenuated by the long-distance transportation through the matrix between the signal sender cells (the PDGF sender fibrin clot and KGF sender fibroblasts) and receiver cells (the PDGF receiver fibroblasts and KGF receiver keratinocytes). The longer the distance that the signals need to be transported, the more significant the signal attenuation/loss can be, and consequently the weaker signals that fibroblasts and keratinocytes will receive. On the opposite, the shorter the distance, the stronger signals that fibroblasts and keratinocytes can receive. Therefore, by regulating the ECM mass, the signal strengths in the wound tissue, and behaviors of cells can all be regulated. As TGF-β is a potent inducer for collagen synthesis, it may strongly regulate and coordinate cell behavior through this new mechanism during wound healing. Based on our simulations

and experiments, we propose this novel mechanism for the inhibition of epidermal proliferation by TGF-β, in which ECM carries diffusible intercellular signals with a fixed resistivity for each cytokine depending on their diffusion coefficients, and TGF-β regulates the ECM resistivity by promoting ECM synthesis.

TABLE V

Mechanical, chemical, and biological parameters used in tissue regeneration model.

Elastic parameters for cells		
Cell type	Young's modulus	Ref.
Keratinocyte	20kPa	(191; 62)
Fibroblast	20kPa	(192)
ECM	20kPa	(193; 194)
Diffusion coefficients of mediators		
Molecular species	Diffusion coefficients	Ref.
PDGF	$2.78\times10^{-8}cm^2s^{-1}$	(64)
KGF	$9.5\times10^{-8}cm^2s^{-1}$	(195)
TGF-β	$2.94\times10^{-9}cm^2s^{-1}$	(181)
Procollagen	$5.0\times10^{-11}cm^2s^{-1}$	This study
Collagen	0	This study
Fibrin clot	0	This study
Intracellular reaction network		
Synthesis of PDGF	$k_s^{PDGF} = 0.005 \times Clot$	This study
Synthesis of procollagen	$k_s^{ProC} = \frac{\hat{k}_s^{ProC} TGF-\beta^{n_{ProC}}}{K_{TGF-\beta,ProC}+TGF-\beta^{n_{ProC}}}$	This study
Synthesis of TGF-β	$k_s^{TGF-\beta} = \frac{\hat{k}_s^{TGF-\beta} PDGF^{n_{TGF-\beta}}}{K_{PDGF,TGF-\beta}+PDGF^{n_{TGF-\beta}}}$	This study
Synthesis of KGF	$k_s^{KGF} = \frac{\hat{k}_s^{KGF} PDGF^{n_{KGF}}}{K_{PDGF,KGF}+PDGF^{n_{KGF}}}$	This study
Degradation of PDGF	$1.668\times10^{-3}min^{-1}$	(64)
Degradation of TGF-β	$2.458\times10^{-4}min^{-1}$	(181)
Degradation of KGF	$4.998\times10^{-3}min^{-1}$	(179)
Maturation of collagen	$1.0min^{-1}$	This study

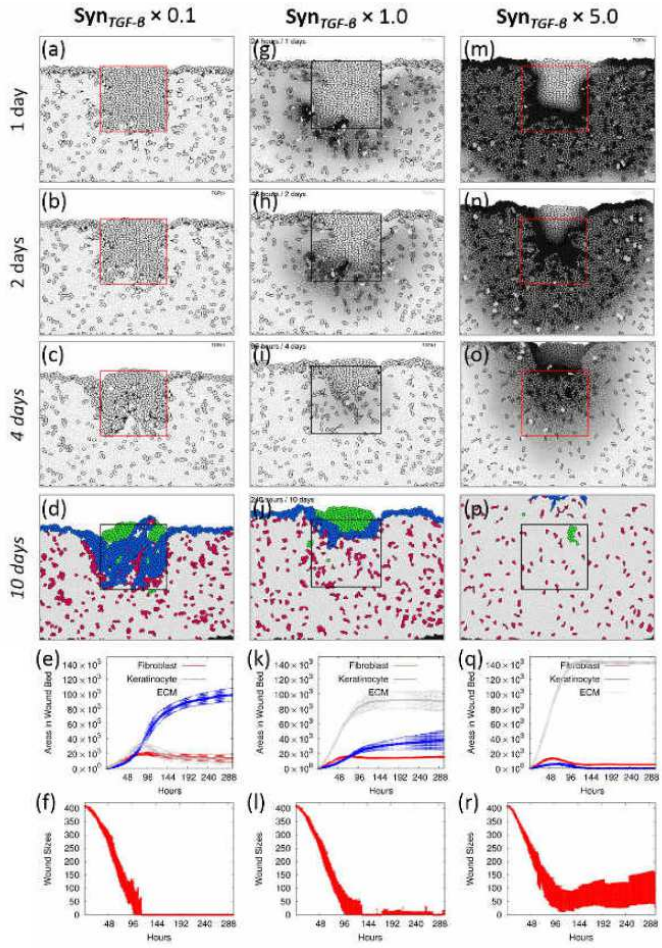

Figure 30. **Effects of TGF-β on tissue pattern.** (a–f) Effects of TGF-β on tissue regeneration with 10 times smaller TGF-β synthesis rate. (a–c) Spatial distributions of TGF-β signal at day 1, 2, and 4 post wound in tissue with 10 times smaller TGF-β synthesis rate. (d) The cellular pattern at day 10 post wound. (e) Temporal dynamics of three major components in wound space. (f) Temporal dynamics of wound size in the tissue with downregulated TGF-β. (g–l) Effects of TGF-β on tissue regeneration with wild type TGF-β synthesis rate. (g–i) Spatial distribution of TGF-β signal at day 1, 2, and 4 post wound in tissue with wild type TGF-β synthesis rate. (j) The cellular pattern at day 10 post wound. (k) Temporal dynamics of three major components in wound space. (l) Temporal dynamics of wound size in the tissue with wild type TGF-β synthesis rate. (m–r) Effects of TGF-β on tissue regeneration with 5 times larger TGF-β synthesis rate. (m–o) Spatial distribution of TGF-β signal at day 1, 2, and 4 post wound in tissue with 5 times larger TGF-β synthesis rate. (p) The cellular pattern at day 10 post wound. (q) Temporal dynamic of three major components in wound space. (r) Temporal dynamic of wound size in the tissue with upregulated TGF-β.

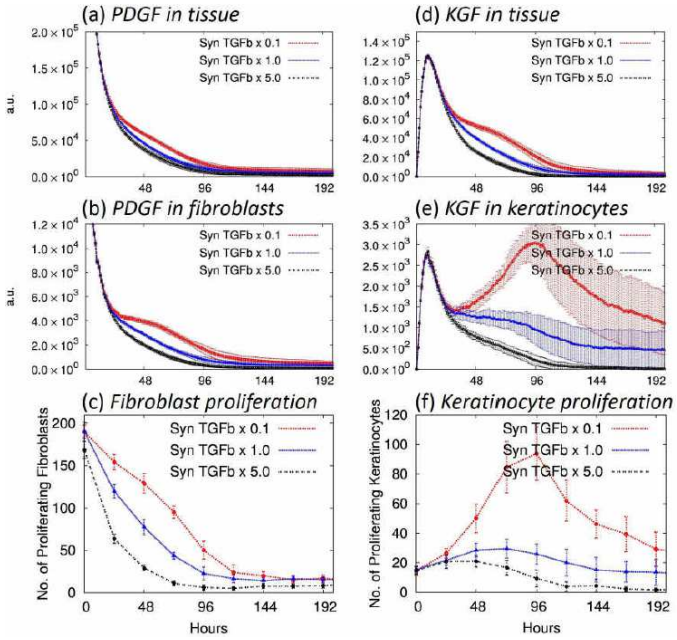

Figure 31. **Temporal dynamics of PDGF, KGF, and cell proliferation of fibroblasts and keratinocytes during tissue regeneration of three TGF-β regulations.** (a) Temporal dynamic of total PDGF in whole tissue. (b) Temporal dynamic of total PDGF in the local environment of fibroblast. (c) Temporal dynamic of total number of proliferating fibroblasts in whole tissue. (d) Temporal dynamic of total KGF in whole tissue. (e) Temporal dynamic of total KGF in the local environment of keratinocyte. (f) Temporal dynamic of total number of proliferating keratinocytes in whole tissue.

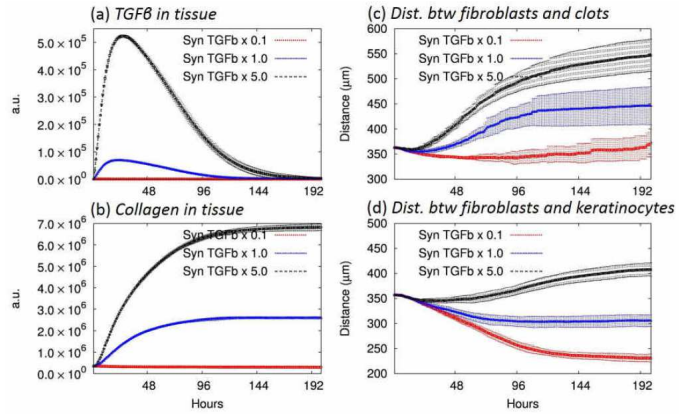

Figure 32. **TGF-β and collagen density in tissue and distances between signal senders and receivers.** (a) Temporal dynamic of TGF-β in whole tissue during tissue regeneration of three different TGF-β regulation. (b) Temporal dynamic of collagen mass in whole tissue during tissue regeneration of three different TGF-β regulation. (c) Temporal dynamic of average distance between fibroblasts and their nearest fibrin clots during tissue regeneration of three TGF-β regulation. (d) Temporal dynamic of average distances between keratinocytes and their nearest fibroblasts during tissue regeneration of three TGF-β regulation.

CHAPTER 5

THE EFFECTS OF ECM GEOMETRY ON CELL MIGRATION AND ELONGATION

5.1 Introduction

Dynamic changes in motility and morphology of individual cell are essential for tissue morphogenesis and development. Such changes are usually achieved through sensing of the environment by living cells. In the past decade, it has been found that the cellular response to environmental signaling is not only through sensing specific ECM ligands chemically, but also through sensing a variety of physical cues generated and acted upon on the adhesive interface between cells and the surrounding extracellular matrix, which provides several physical and geometrical cues necessary for the regulation of these cellular behaviors (140).

Due to the difficulty in reproducing the ECM environment realistically, many studies of cell-ECM communications are based on matrix model using substrate to mimic the ECM. These studies provided useful insights into cell motility and generation of traction force in response to the biophysical cues from the environment in the forms of topography or stiffness of the substrate (141; 142). Upon the application of the traction forces generated by the cell on the ECM, the cell integrins link to the ECM through cytoskeleton to form focal adhesions, which are the hubs of many proteins responsible for signaling transmission and mechanical support (143; 144). The alteration in maturation and turnover of focal adhesions, coupled

with changes in the dynamic of actin filaments have been demonstrated to play important roles in regulating cell migration on substrate (145). Many studies have showed that the changes in cell morphology and cell motility are under the regulation of different cues from the substrate (146; 147; 148; 149; 150). However, while the responses of cells to different ECM spatial arrangements have been characterized extensively, the mechanisms under which cells sense changes in ECM geometry at a sub-cellular level and translate such changes into cellular scale responses are still not well understood (151).

In this study, we apply the DYCELFEM model to investigate the roles of ECM geometry on guiding cell elongation and cell migration, and on regulating the spatial pattern of field of traction forces. Our modeling results are consistent with quantitative data of *in vitro* studies of cell morphology and migration on substrate of different geometry. The overall morphological changes of elongated cell shape on substrate of pattern with increased spacing is reproduced in our simulation. Both experiment and simulation of cell migration show that cell tends to migrate along the direction of the substrate pattern. In addition, we modeled cell migration and cell morphology under the treatment of Y27632, which inhibits the activity of myosin II. Our simulation result along with the *in vitro* study both show that the orientation of cell migration was dramatically reduced. These findings suggest that the focal adhesion induced polarization might be a key factor in guiding oriented cell migration and regulating the changes of cell morphology.

5.2 Cell-ECM model

5.2.1 Geometric model of cell and ECM

In our model, the location of a vertex $\boldsymbol{\nu}_i$ is denoted as $\mathbf{x}_i$. A two-dimensional cell Ω is represented as an oriented polygon composed as a set of boundary vertices $V_{\partial\Omega} \equiv \{\boldsymbol{\nu}_i \in \partial\Omega \subset \mathbb{R}^2\}$, a set of internal vertices V_{Int} and a set of triangular elements $T_\Omega \equiv \{\boldsymbol{\tau}_{i,j,k} : \boldsymbol{\nu}_i, \boldsymbol{\nu}_j, \boldsymbol{\nu}_k \in V_{\partial\Omega} \cup V_{Int}\}$, which are generated using *farthest point sampling* method (Figure 33a, see more details in (32)).

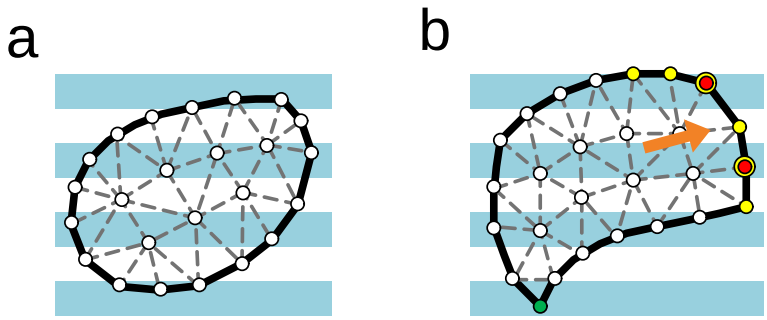

Figure 33. **Geometric model of cell and ECM.** (a) The boundary of each cell is defined by a counter-clock wise oriented polygon containing a number of boundary vertices. Triangular mesh tiling up each cell is generated using the farthest point sampling method based on Delaunay triangulations. ECM is represented as stripes with predefined width. (b) Once the cell determines the direction of polarization (orange arrow), the vertices with normal positively aligned with the polarization direction (yellow) are chosen as the lamellipodal. The lamellipodal vertices which are covered by the ECM stripes (blue) are vertices (red) where protrusive forces are applied on. The vertex having the longest average distance from the lamellipodal (green) is chosen as the uropodal.

5.2.2 Viscoelastic cell model

The cytoskeleton is a polymer scaffold that spans the cytoplasm of the cell. The cytoskeleton network is mainly composed of actin filaments along with accessory proteins, such as myosins, which serve as key components to generate biomechanical forces for cell motility (152). Previous studies on cell mechanics have showed that the actomyosin cytoskeleton of the cell adopts the viscoelastic property (153; 154). Following the previous computational studies (155; 156), we assume that the linear viscoelasticity can adequately describe the mechanical property of the cell during elongation and migration. We use the strain tensor $\boldsymbol{\epsilon}(\mathbf{x})$ to describe the local deformation of the cell at $\mathbf{x}$. It takes the form of $\epsilon_{1,1} = \partial u_1/\partial x_1$, $\epsilon_{2,2} = \partial u_2/\partial x_2$, and $\epsilon_{1,2} = \epsilon_{2,1} = \frac{1}{2}(\partial u_1/\partial x_2 + \partial u_2/\partial x_1)$, where $\mathbf{u}(\mathbf{x}) = (u_1(\mathbf{x}), u_2(\mathbf{x}))^T \subset \mathbb{R}^2$ is the displacement of $\mathbf{x}$.

We use the stress tensor $\boldsymbol{\sigma}$ to represent the forces. $\boldsymbol{\sigma}$ is related to the strain tensor $\boldsymbol{\epsilon}$ through the Maxwell model (materials with viscoelastic properties can be studied using the Maxwell model (157; 158)) $\frac{1}{E}\frac{d\boldsymbol{\sigma}}{dt} + \frac{\boldsymbol{\sigma}}{\eta} = \frac{d\boldsymbol{\epsilon}}{dt}$, where E and η are the elastic modulus and the viscosity coefficient of the cell, respectively. Values of E and η are listed in Table VI.

The strain energy E_Ω associated with the deformation $\mathbf{x} \in \Omega$ is given by $E_\Omega = \frac{1}{2}\int_\Omega (\boldsymbol{\sigma}(\mathbf{x}) + \sigma_a \boldsymbol{\delta}_{ij}(\mathbf{x}))^T \boldsymbol{\epsilon}(\mathbf{x}) d\mathbf{x}$, where σ_a is a homogeneous contractile pressure (159). In addition, the energy due to the focal adhesion between cell and the ECM also contributes to the total energy of the cell, which is given by $\frac{\gamma}{2}\int_\Omega \mathbf{u}(\mathbf{x})^2 d\mathbf{x}$, where γ is the dragging coefficient which is proportional to the strength of focal adhesions (160). Furthermore, the line tension also contributes a local force on the cell boundary. So we introduce the line tension energy term $\int_{\Gamma_\Omega} \boldsymbol{\lambda}\mathbf{u}(\mathbf{x}) d\mathbf{x}$, where

$\boldsymbol{\lambda} = -f_m P_0(\mathbf{x})\kappa(\mathbf{x})\mathbf{n}(\mathbf{x})$, f_m is a contractile force per unit length acting across the cell boundary, $P_0(\mathbf{x})$, $\kappa(\mathbf{x})$, and $\mathbf{n}(\mathbf{x})$ are the boundary length, the curvature and outward unit normal at $\mathbf{x}$, respectively (159).

The overall free energy of the cell can be written as

$$E_\Omega = \frac{1}{2}\int_\Omega (\boldsymbol{\sigma}(\mathbf{x}) + \sigma_a \delta_{ij})^T \boldsymbol{\epsilon}(\mathbf{x}) d\mathbf{x} + \frac{Y}{2}\int_\Omega \mathbf{u}(\mathbf{x})^2 d\mathbf{x} - \int_{\Gamma_\Omega} f_m P_0(\mathbf{x})\kappa(\mathbf{x})\mathbf{n}(\mathbf{x}) d\mathbf{x}. \tag{5.1}$$

The total energy in Eqn Equation 5.1 can be minimized when the cell reaches to its balance state where $\partial E_\Omega(\mathbf{u})/\partial \mathbf{u} = 0$. So for each triangular element $\boldsymbol{\tau}_{i,j,k}$, we minimize the total energy $E_{\boldsymbol{\tau}_{i,j,k}}$ from Eqn Equation 5.1 by deriving $\partial E_{\boldsymbol{\tau}_{i,j,k}}(\mathbf{u}_{\boldsymbol{\tau}_{i,j,k}})/\partial \mathbf{u}_{\boldsymbol{\tau}_{i,j,k}} = 0$ and we obtain the corresponding linear force-balance equation

$$\mathbf{K}_{\boldsymbol{\tau}_{i,j,k}} \mathbf{u}_{\boldsymbol{\tau}_{i,j,k}} = \mathbf{f}_{\boldsymbol{\tau}_{i,j,k}}, \tag{5.2}$$

where $bK_{\boldsymbol{\tau}_{i,j,k}}$, $\mathbf{u}_{\boldsymbol{\tau}_{i,j,k}}$, and $\mathbf{f}_{\boldsymbol{\tau}_{i,j,k}}$ are the stiffness matrix, displacement vector, and integrated force vector of $\boldsymbol{\tau}_{i,j,k}$ (see more details of derivation of Eqn Equation 5.2 in ref (32)).

We can then gather the element stiffness matrices of all triangular elements in all cells and assemble them into one global stiffness matrix $\mathbf{K}$. The linear relationship between the concatenated displacement vector $\mathbf{u}$ of all vertices in all cells and the integrated force vector $\mathbf{f}$ on all vertices is then given by

$$\mathbf{K}\mathbf{u} = \mathbf{f}. \tag{5.3}$$

The change of cell shape at specific time step then can be obtained by solving this linear equation Equation 5.3. For vertex $\boldsymbol{\nu}_i$ at $\mathbf{x}_i$, its new location is then updated as $\acute{\mathbf{x}}_i = \mathbf{x}_i + \mathbf{u}(\boldsymbol{\nu}_i)$.

5.2.3 Focal adhesion between cell and the ECM

Cell adhesion to ECM plays important role in a variety of cellular behaviors ranging from cell migration to proliferation. The most important subcellular structure that mediate the regulation of interactions between cell and the ECM are the focal adhesions. They regulate the communication between the cell and the ECM through the complex of integrins and the fibronectins. They not only work as mechanical junctions that connect cellular cytoskeleton to the ECM, but also as hubs of chemical signaling in many pathways (146). While cell is migrating, the assembly of focal adhesions can be observed on both leading side (lamellipod) and rear side (uropod) of the cell. These focal adhesions anchor the migrating cell on the ECM, link ECM to the actin filaments inside of cell, and activate migration-related signaling molecules such as Rac, Cdc42, and Arp2/3. These proteins then regulate the actin polymerization to drive stabilized cell protrusions on the leading edge. Meanwhile, at the rear of the cell, adhesions to the substrate must disassemble for cells to move on (161). Previous experimental study has showed that the strength of the focal adhesion is directly proportional to the number of bound integrin-ligand bonds between cell and the ECM (162). So we also assume that the dragging coefficient Υ in Eqn Equation 5.1 indicating the strength of focal adhesion is also proportional to the bound integrin ligand. In our model, for each migrating cell, we denote its lamellipod as the vertices whose outward normal is positively aligned with the polarization direction of the cell (yellow vertices in Figure 33b) and denote its uropod as the vertex which has the longest

average distance from the lamellipod vertices (green vertex in Figure 33b). For each vertex $\boldsymbol{v}_i$ in Ω, and covered by the ECM stripes (blue stripes in Figure 33b), we assume there are constant number of integrin ligand, which would bind and unbind with the fibronectin from the ECM. Then we can write the balance in the number of bound and free integrin ligand following the ref (163) as

$$\frac{dR_b}{dt} = k_f n_s R_r - k_r R_b, \tag{5.4}$$

where R_b and R_r are the number of bound and free integrin ligand; k_f is the forward rate constant (rate from free ligand to bound ligand); n_s is an uniform concentration; k_r is the reverse rate (rate from bound ligand to free ligand) depend on the forces applied on $\boldsymbol{v}_i$ following the Bell's equation (164): $k_r = k_{r0} e^{\frac{f_r}{f_0}}$, where f_r is the force applied on $\boldsymbol{v}_i$, and k_{r0} and f_0 are constants. The dragging coefficient Υ_i at $\boldsymbol{v}_i$ is then proportional to the number of bound integrin-ligand R_b. For vertex $\boldsymbol{v}_j$ in the Ω, but not covered by the ECM stripes, there are no integrin-fibronectin complex existed, so there is no focal adhesion. Then we assign a very small constant to its dragging coefficient Υ_j.

5.2.4 Focal adhesion regulated cell polarization

Cell polarization is the basic morphogenetic response to the ECM adhesion. For migratory cells such as fibroblast, polarization determines the unique direction and the leading edge for cell to move in one direction (161). Previous experimental study has demonstrated that the fibroblast polarization process is controlled by focal adhesion mechanosensing (165). The radially spreading cell has dot-like nascent focal adhesions on the boundary. These adhesions gradually grow to elongate and orient in parallel directions as the result of pulling forces on

them. The orientation of these focal adhesions determine the future axis of cell polarization direction. As cell is fully polarized, there are large focal adhesions generated on both lamellipod and uropod (165). In our model, we adopt the strategy of determining the direction of cell polarization based on the spatio-temporal pattern of focal adhesions. Following a previous computational study (166), for any vertex $\boldsymbol{\nu}_i$ in cell Ω, we define three different types of cell adhesion on $\boldsymbol{\nu}_i$ to the ECM: the adhesion point (A), the focal complex (FX), and the focal adhesion (FA). Each adhesion type corresponds to one particular maturation level with particular lifetime and resistance to traction force. A has short lifetime t_A and weak resistance to traction. It can mature into FX under the stimulation of traction force above a threshold R_thr (traction is calculated as $\mathsf{T}_i = \mathsf{Y}_i \mathbf{u}_i$ (159)). FX can also mature into FA under the stimulation of traction force above a threshold T_thr. Both FX and FA have longer lifetime t_FX, t_FA. If $\boldsymbol{\nu}_i$ is not covered by the ECM stripes, it will only remain as A because there is no integrin-fibronectin complex existed to be matured. For the migrating cell Ω, we re-sample its polarization direction after one round of cycling time ($\mathsf{T}_\mathsf{r} + \mathsf{t}_\mathsf{A} + \mathsf{t}_\mathsf{FX} + \mathsf{t}_\mathsf{FA}$, T_r is the adhesion recycling time corresponding to the period after cell translocation (166)) based on the spatial distribution of adhesion type on lamellipod: for each vertex $\boldsymbol{\nu}_i$ on the current lamellipod $\mathbf{V}_l = \{\boldsymbol{\nu}_i\}$ of the migrating cell, the probability $\pi_{\boldsymbol{\nu}_i} = \frac{w_{\boldsymbol{\nu}_i}}{\sum_{\boldsymbol{\nu}_k \in \mathbf{V}_l} w_{\boldsymbol{\nu}_k}}$, where $w_{\boldsymbol{\nu}_i}$ is the weight of $\boldsymbol{\nu}_i$ according to its adhesion type (see Table VI for weight values). Then the probability of the new polarization direction towards $\boldsymbol{\nu}_i$ is sampled according to the probability of $\pi_{\boldsymbol{\nu}_i}$.

5.2.5 Measurements of cell morphology and migration

We introduce four measures, *elongation*, *alignment of traction vector*, *guidance*, and *persistence* to quantify the cell elongation, cell orientation, and cell migration. The *elongation* is defined as the aspect ratio of the cell (short/long axes); The *alignment of traction vector* is defined as T_y/T_x, where (T_x, T_y) is the traction vector; The *guidance* is defined as the percentage of cells that have a trajectory with average angle less than 25° with respect to ECM pattern orientation; The *persistence* is defined as the ratio of the distance between the start and the end locations of cell over the length of the traversed path.

5.2.6 Cell culture

UV micro patterning (159) is used to mimic the linear ECM arrangements. We pattern 0.5–10μm thick collagen lines onto an polyacrylamide elastic substrate, varying the spacing between lines at a subcellular length scale (0–10μm, this width of the stripes is chosen such that adhesion formation and stability are not limited) and varying their orientation with respect to each other. NIH 3T3 cells (fibroblast) are then plated on the substrates. The high resolution, time lapse light microscopy is then used to measure their motility and localization of fluorescently-tagged protein constructs. Cells treated with 20 μM of the ROCK inhibitor Y27632 were incubated in media before imaging.

5.3 Results

5.3.1 Cells are guided in response to ECM geometry

To study the effects of ECM geometry on cell behaviors, we plated cells on substrate coated with fibronectin stripes with fixed width 2μm and spaced varying from 0μm to 10μm. We found

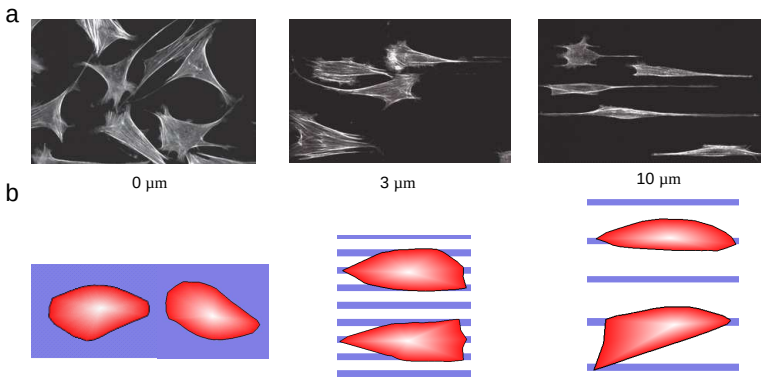

Figure 34. **Cell morphology changes under different ECM geometry.** (a) The observed cell morphology under different ECM geometry (gaps in 0, 3, and 10µm, respectively). (b) The simulated cell morphology under different ECM geometry.

that as the gap distance increased from 0µm to 10µm, the cells exhibit elongated morphology (Figure 34a). The simulated cells using the computational model also exhibit the same elongated morphology (Figure 34b). The results of *elongation* of both experiment and simulation also show the same elongated pattern that the elongation became smaller as the gap distance increased from 0µm to 10µm (Figure 35c and Figure 35d). In addition to the morphology changes, cells aligned their migration direction with the ECM orientation that the trajectory became more parallel to the ECM pattern orientation (Figure 35a and Figure 35b). The orientation of traction stresses also became more parallel to the direction of the pattern as the stripe separation increased (as showed by the *alignment of traction vector* in Figure 35c and Figure 35d). The results of *guidance* showed that there are more cells with migration directionality parallel with the pattern direction (Figure 35c and Figure 35d). The results of *persistence* showed that there

was a slight increase in migration persistence as the gap between stripes increased (Figure 35c and Figure 35d). These measurements from both experimental observation and simulation indicated that cells would exhibit directional migration on the oriented patterns. Remarkably, for all the measurements introduced in this study, cell elongation, traction vector orientation, and migration directionality, showed a monotonic increasing relationship between cell response and pattern spacing.

5.3.2 Myosin II promotes cell elongation and migration orientation

Myosin II plays important roles in mediating cell shapes (167), reinforcing the cytoskeleton to link to the ECM and driving composition in focal adhesion maturation (168; 169). To elucidate its roles in elongation and orientation of cells parallel to the ECM axis, we treated cells with 20μM of the ROCK inhibitor Y27632. Under such treatment, there is a reduce of cellular contractility due to the inhibition of myosin light chain phosphorylation (170). In the viscoelastic model, we reduce the value of σ_a from 2.4kPa to 0.24kPa to mimic the reduce of the myosin-induced contractility. In addition, we reduced the value of adhesion type weight to mimic the perturbation of polarization due to the reduced mechanosensing from focal adhesion (165). Under the myosin inhibition, the cell migration from both observation and simulation are less oriented to the ECM direction comparing with that under control condition (trajectory plots in Figure 36). The measure of guidance from both observation and simulation also showed that the cell migration under the myosin inhibition was less influenced by the pattern direction that the guidance decreased dramatically (guidance plots in Figure 36). These results indicate

that the focal adhesion induced cell polarization is essential for guiding cell migration that the reduce of myosin II will perturb this mechanism.

5.4 Conclusion and discussion

Focal adhesions play important roles in cellular behaviors such as ell migration and cell proliferation and physiological processes such as tissue regeneration and cancer invasion. Focal adhesion is though to play as the hub for both protein signaling and mechanics sensor between cell and the ECM. However, the mechanism that how cells sense and respond to the changes in ECM geometry at subcellular level and translate these geometry cues into cellular scale behaviors are still not well understood. In this study, we develop a viscoelastic model coupling with cell-ECM interactions though the dynamic of focal adhesions to investigate the effects of geometry of ECM on changes in cell morphology and cell migration. *in vitro* experiment is also conducted to test the prediction of our simulation and hypothesis.

To realistically capture the dynamic changes in cell shapes and cell behaviors, we incorporate the viscoelastic property to the cell. A fine triangular mesh tiling the cell domain is constructed for the finite element discretization of viscoelastic energy term. The ECM-mimicking substrate is also explicitly incorporated in our model. The dragging energy between cell and ECM due to the presence of focal adhesion is considered. The dynamic lifetime of focal adhesion formation, maturation, and turnover under the applied traction force is modeled using differential equations over time for each focal adhesion complex on discretized cell vertex. The cell polarization (directly migration) based on the spatial regulation of focal adhesion is stochastically modeled. For the *in vitro* experiment, we use UV micro patterning as the ECM-mimicking substrate and

plate NIH 3T3 cells on the substrate with patterns in different spacing. We also treat Y27632 drug to cells to elucidate the role of myosin II contractility in regulating cell elongation and migration.

Our results suggest the role of ECM geometry on the cell morphology and migration. As the distance between pattern increased, the cell shape elongated, which can be characterized by the long tail dragged by the focal adhesion point on the uropod (Figure 34a and b). In addition, the spatial distribution of focal adhesion also regulates the orientation of cell migration. So the cell tends to migrate along the orientation of the substrate. This is also consistent with previous reports of cells undergoing directional migration in the presence of directional cues from ECM (147; 148; 149). Furthermore, as we reduced the myosin contractility, the migration orientation was also reduced. These observation suggests that there exists a mechanism of the positive loop feedback between myosin and focal adhesion in strengthening cell polarization based on the spatial distribution and maturation level of focal adhesions.

TABLE VI

Geometric, mechanical, chemical, and biological parameters used in cell-ECM model.

Name	description	value	Ref.
r_{cell}	Cell radius	$10\mu m$	(176)
E_{cell}	Cellular Young's modulus	$5.4kPa$	(159)
ν_{cell}	Poisson's ratio	0.43	(159)
σ_a	contractile pressure coefficient	$2.4kPa$	(159)
μ_{cell}	Cellular viscosity	$2kPa \cdot s$	(196; 156)
Υ	Dragging coefficient	$0.2nN \cdot s/\mu m^3$	(153)
γ	Line tension coefficient	$0.7nN/\mu m$	(159)
T_r	Adhesion proteins recycling time	58s	(166)
R_{thr}	Tension threshold	1.0	(166)
T_{thr}	Translocation threshold	2.3	(166)
T_A	Adhesion point lifetime	14s	(166)
T_{FX}	Focal complex lifetime	72s	(166)
T_{FA}	Focal adhesion lifetime	72s	(166)
w_A	Weight of adhesion point for polarization resampling	2	This study
w_{FX}	Weight of focal complex for polarization resampling	5	This study
w_{FA}	Weight of focal adhesion for polarization resampling	10	This study
w_A^r	Reduced weight of adhesion point for polarization resampling under Y27632	1.1	This study
w_A^r	Reduced weight of focal complex for polarization resampling under Y27632	1.4	This study
w_A^r	Reduced weight of focal adhesion for polarization resampling under Y27632	1.9	This study

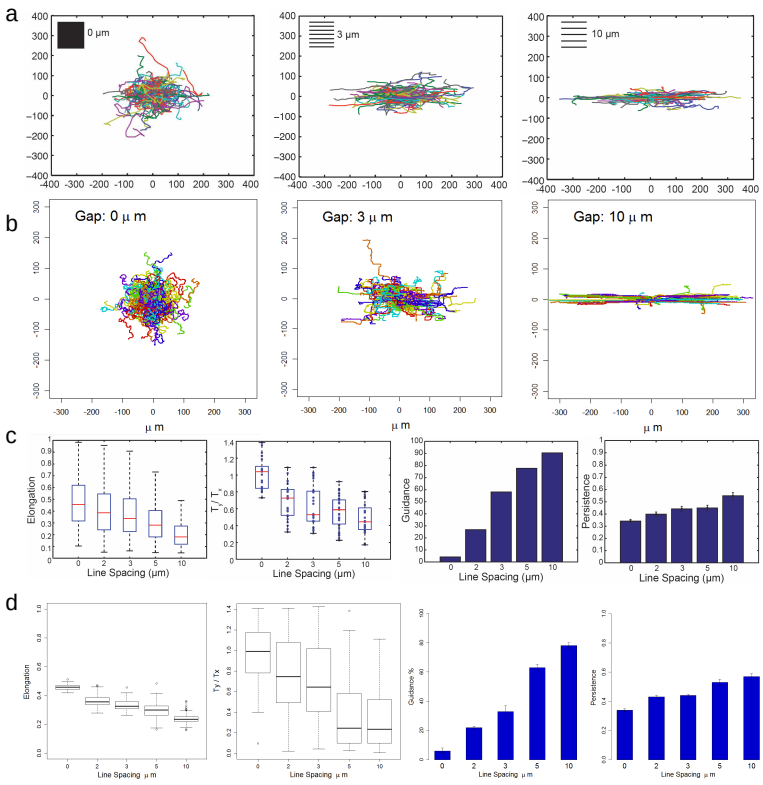

Figure 35. **Cells are guided in response to ECM geometry.** (a) The observed trajectory of cell migration path. (b) The simulated trajectory of cell migration path. (c) The observed elongation, alignment of traction vectors, guidance and persistence of cells on ECM with different geometry. (d) The simulated elongation, alignment of traction vectors, guidance and persistence of cells on ECM with different geometry.

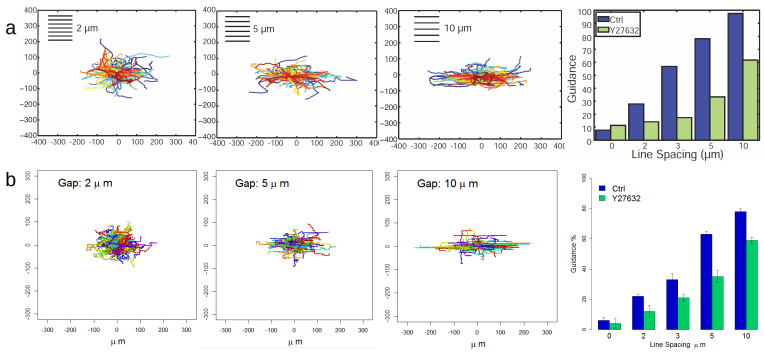

Figure 36. **Cell orientation in response to ECM geometry under inhibition of Myosin II contractility.** (a) The observed trajectory of cell migration path and corresponding guidance with treatment of Y27632. (b) The simulated trajectory of cell migration path and corresponding guidance with treatment of Y27632.

CHAPTER 6

CONCLUSION

6.1 Achievements and Applications

In this thesis, we developed a novel computational cell model called dyCelFEM which has several advancement over existed computational cell models. First, it accounts for detailed changes in cellular shapes and mechanics of a large population of interacting cells. In addition, it can model the full range of cell motion, from free movement of individual cells to large scale of collective cell migration. Furthermore, the transmission of mechanical forces via intercellular adhesion and its rupture is also modeled. The intracellular protein signaling networks could also be embedded in individual cells to control of cell behaviors (see details of embedding signaling network in individual cell in the following three chapters). Overall, the dyCelFEM model is well-suited to study biological processes where migrating cells with dynamic changes in shape and mechanics at large scale are involved. We then applied dyCelFEM to study two specific physiological processes, namely, wound healing (includes two sub-process: re-epithelialization and tissue regeneration) and cell motion on ECM.

6.1.1 Application on re-epithelialization process

We apply the dyCelFEM model to investigate the effects of biochemical and mechanical cues on migration and proliferation of a population of cells during re-epithelialization. Furthermore, we also apply dyCelFEM to study the roles of E-cadherin regulated cell-cell adhesion

on collective cell migration during re-epithelialization. The advancement of dyCelFEM model in studying the biochemical and mechanical signals within collective cell migration during re-epithelialization includes: First, it describes the cell-cell adhesions with more details as polylines (curved edges) but not as monoline (straight-edge). A recent theoretical study (56) has demonstrated that monoline cell model affects the cell motion in cell engulfment and cell invasion due to restricted cell deformation modes while these restriction are not faced by using polyline cell model. Considering that a moving cell often dynamically changes its adhesive structures during migration (55), it is more appropriate to use polyline cell model but not monoline cell model (15; 16; 50) to study the re-epithelialization process. Second, it belongs to the group of finite element cell models (57; 58; 59; 26; 19; 60; 50) which provides realistic descriptions of cell shapes and mechanics. But these finite element method based model focused more on simulating tissue dynamics with small scale of geometric changes. The wound size of re-epithelialization studied by these models is relatively at the same magnitude of the cell diameter (19; 50). Re-epithelialization achieved in these cases are mainly through the line tension at the wound boundary. dyCelFEM model follows the scheme of particle finite element method (30) which can model individual cell moving freely or separate from the main analysis tissue domain. This feature make it more suitable to model re-epithelialization with large wound size which requires large scale of dynamic cell migration and proliferation to achieve wound closure.

Our results suggest biochemical and mechanical cues play different roles in guiding migration of keratinocyte during re-epithelialization. The influence of biochemical cues are restricted to areas close to the wound bed, while mechanical cues influence the skin tissue globally. Fur-

thermore, biochemical cues are better at guiding keratinocyte migration with improved directionality and persistence, while mechanical cues are better at coordinating keratinocyte migration, with improved collective cell migration so keratinocyte can follow their moving neighbors efficiently towards the wound bed. In addition, our results show that the decrease of E-cadherin regulated cell-cell adhesion significantly perturbed the cell-cell coordination and reduced the migration directionality; inhibition of mechanical force transmission through E-cadherin significantly reduced the migration directionality and persistence and prolonged the re-epithelialization process. These findings will help us to gain understanding of the full mechanism of wound healing under regulation of intercellular mechanical forces through E-cadherin. These findings will help us to gain understanding of the full mechanism of wound healing.

6.1.2 Application on tissue regeneration process

we applied DYCELFEM model to study the tissue regeneration process. We first construct intracellular gene regulatory networks to stochastically determine the cell behaviors including growth, division, apoptosis, and migration for each individual keratinocyte and fibroblast. These networks are embedded in each individual cell. We also incorporate intercellular communication via the diffusion of major soluble mediators (PDGF, KGF, and TGF-β) in the ECM and fibrin clot. We build a computational model of the cross-section of a skin tissue. Excisional wounds were created on the *in silico* skin, and the healing processes were simulated. By dynamically tracking behaviors, positions, spatial configurations of cells, and spatial distributions of different mediators over time, we are able to correctly reproduce the formation of granulation tissue and re-epithelialization during wound healing. We then study the effect of TGF-β

on dermal and epidermal pattern formation during wound healing. Combining computational simulations and experimental observations, our results suggest a novel mechanism for the inhibition of keratinocyte proliferation and re-epithelialization by TGF-β. Our results suggest that TGF-β can attenuate the strength of PDGF and KGF signals that fibroblasts and keratinocytes receive by promoting ECM synthesis and deposition. In analogy to electrical circuits, the ECM acts as a resistor for PDGF and KGF signals, and the TGF-β act as a potentiometer that can change the resistivity of the resistor, therefore indirectly regulate the signal patterns and cell behavior. This study exhibits the potential of our method in helping to gain new understanding of the control mechanisms of important multi-cellular processes.

6.1.3 Application on process of cell motion on ECM

We apply the dyCelFEM model to investigate the roles of ECM geometry on guiding cell elongation and cell migration, and on regulating the spatial pattern of field of traction forces. Our modeling results are consistent with quantitative data of *in vitro* studies of cell morphology and migration on substrate of different geometry. The overall morphological changes of elongated cell shape on substrate of pattern with increased spacing is reproduced in our simulation. Both experiment and simulation of cell migration show that cell tends to migrate along the direction of the substrate pattern. In addition, we modeled cell migration and cell morphology under the treatment of Y27632, which inhibits the activity of myosin II. Our simulation result along with the *in vitro* study both show that the orientation of cell migration was dramatically reduced. These findings suggest that the focal adhesion induced polarization might be a key factor in guiding oriented cell migration and regulating the changes of cell morphology.

6.2 Limitations and Future Works

The dyCelFEM model is currently restricted to simulate cell and tissue in two dimension. The model can be further improved to three dimension. The generation of mechanical forces in current model are simplified as the consequence of cell elasticity. This can be improved by incorporating the realistic biophysical mechanism into the body of individual cells. For example, the process of actin polymerization driving cell migration could be explicitly modeled on the membrane of the cell. The cell behaviors in current model can be improved by taking account more factors. For examples, The leading edge of the migrating cell is stiffer than the rear edge. Such different stiffness in cell position can be incorporated to model more realistic cell migration. The viscosity of the cell influence the interstitial pressure which drives cell growth. The effect of viscosity can be incorporated to model more realistic cell growth. The cell apoptosis is a process where cell loses its contractility and collapses eventually. In our model, it can be modeled as a cell shrinkage process which is more realistic. The intercellular chemical signaling network in current model is simple and qualitative. It can be improved by further investigation of literatures on corresponding protein pathways.

APPENDICES

Appendix A

SOFTWARE IMPLEMENTATION OF DYCELFEM

A.1 Introduction

The software implementation of dyCelFEM provides a dedicated interface for setup of the structures of cellular tissue through either a data file or manually input. In addition, the mechanical property of cells such as the cell elasticity can also be set through the interface. It also has the chemical signaling network embedded in individual cells to specifically control the cell behaviors. The numerical component based on the dynamic finite element method is then carried out to simulate the cell motion. The cell geometry under the regulation of predefined mechanisms is then updated.

A.2 Manual of DyCelFEM

dyCelFEM is a compiled application written in C++ and makes use of the library of the Systems Biology Markup Language (SBML) (45). The graphic user interface is written in Qt and supports real-time visualization using OpenGL. To run the program of cellular tissue simulation on dyCelFEM, the input file should contain the the correct geometry structure data of the tissue in a variety of different formats to ensure it can be correctly parsed (Please follow the accepted data formats shown in the online manual http://sts.bioe.uic.edu/CeldyFEM/README.txt). There is also an alternative way to generate a tissue with customized shape by using the user interface panel *New Tissue Diagram*. The different cell types and cytokines controlling cell

Appendix A (Continued)

behaviors can be edited in the user interface panel *Cell Cytokine Manager* including the cell size, cell elasticity, cell-cell adhesion rupture threshold, synthesis rate, diffusion rate, degradation rate of cytokines. The signaling network containing the information of sources of cytokine (the types of cells which release these cytokines), the effect on cell behavior (promoting or inhibiting effect) in terms of scaling factors can be edited in the user interface panel *Network*. After preparing the cellular tissue, defining the cell type and cell behavior, setting the signaling network, and selecting corresponding parameters, the numerically intensive algorithms of dynamic finite element method for calculating cell deformation while in movement, the differential equations for calculating cytokine concentration within the tissue over time, and postprocessing collision detection and topologic refinement of colliding cells are performed at each time step during the simulation. The numerical details of the implementation of these algorithms can be found in reference (32). The user interface facility also encompasses data visualization of the tissue during the simulation. Different modes showing different type of data (the triangular mesh of each cell, the concentration of cytokines in each cell, the cell behavior type of each cell) can be switched for viewing by button-clicking. dyCelFEM facilitates data export through button-click to save to a .df file involving the data of cell geometry, cell mechanics, and cytokine concentration. Details about the applications are given in the online tutorial of dyCelFEM (http://sts.bioe.uic.edu/CeldyFEM/tutorial.php). dyCelFEM is distributed freely and can be downloaded at http://sts.bioe.uic.edu/CeldyFEM/. Windows, OSX and Linux are supported. We expect that the new insight provided by this software will contribute to further studies of cellular tissue processes.

Appendix B

RE-EPITHELIALIZATION MODEL

B.1 The contour plots of concentration of EGF over time

The contour plots of computed EGF concentration from solving Eqn (Equation 3.5) in the wound tissue at different time steps under chemotaxis and cohesotaxis are shown as an example in Figure 37. EGF is synthesized in the wound bed area and diffuse to the areas around the wound bed. As the wound bed is covered by the migrating keratinocytes, EGF concentration decreases and eventually disappears when the wound bed is completely repaired.

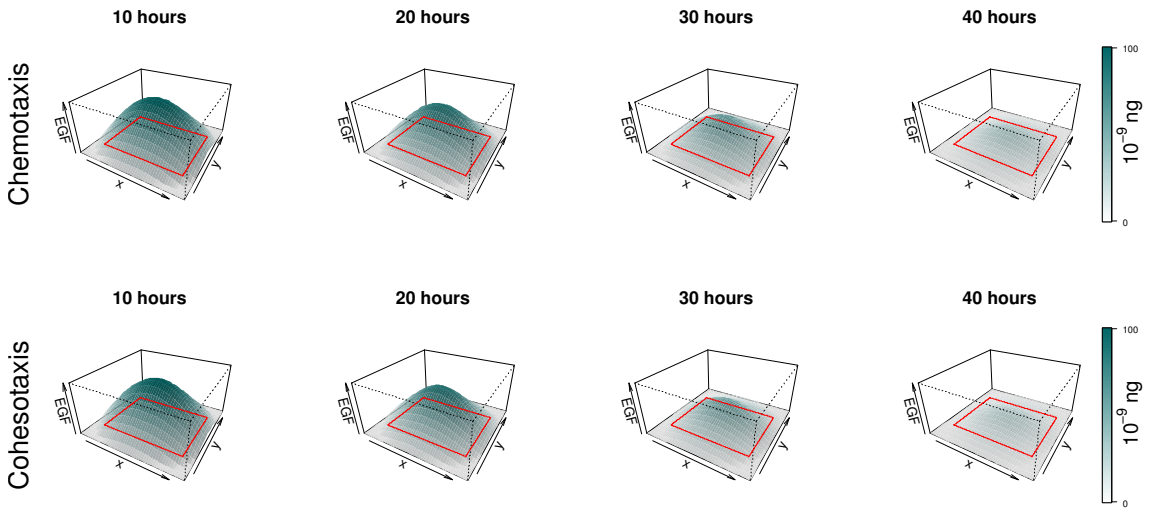

Figure 37. **Contour plots of EGF concentration in the tissue at different time steps under chemotaxis and cohesotaxis.** The red boxes indicate the wound edge at initiate time.

CITED LITERATURE

1. Alberts, B., Bray, D., Lewis, J., Raff, M., Roberts, K., Watson, J. D., and Grimstone, A.: Molecular biology of the cell (3rd edn). Trends in Biochemical Sciences, 20(5):210–210, 1995.

2. Hulpiau, P. and Van Roy, F.: Molecular evolution of the cadherin superfamily. The International Journal of Biochemistry & Cell Biology, 41(2):349–369, 2009.

3. Hynes, R. O.: Integrins: bidirectional, allosteric signaling machines. Cell, 110(6):673–687, 2002.

4. Ehrenhofer-Murray, A. E.: Chromatin dynamics at dna replication, transcription and repair. European Journal of Biochemistry, 271(12):2335–2349, 2004.

5. Görlich, D. and Kutay, U.: Transport between the cell nucleus and the cytoplasm. Annual Review of Cell and Developmental Biology, 15(1):607–660, 1999.

6. Howard, J.: Mechanics of motor proteins and the cytoskeleton. Sinauer Associates Sunderland, 2001.

7. Gunning, P. W., Ghoshdastider, U., Whitaker, S., Popp, D., and Robinson, R. C.: The evolution of compositionally and functionally distinct actin filaments. J Cell Sci, 128(11):2009–2019, 2015.

8. Vedula, S. R. K., Ravasio, A., Lim, C. T., and Ladoux, B.: Collective cell migration: a mechanistic perspective. Physiology, 28(6):370–379, 2013.

9. Arciero, J. C., Mi, Q., Branca, M. F., Hackam, D. J., and Swigon, D.: Continuum model of collective cell migration in wound healing and colony expansion. Biophysical Journal, 100(3):535–543, 2011.

10. Lee, P. and Wolgemuth, C. W.: Crawling cells can close wounds without purse strings or signaling. PLoS Computational Biology, 7(3):e1002007, 2011.

11. Cochet-Escartin, O., Ranft, J., Silberzan, P., and Marcq, P.: Border forces and friction control epithelial closure dynamics. Biophysical Journal, 106(1):65–73, 2014.

12. Chen, N., Glazier, J., Izaguirre, J., and Alber, M.: A parallel implementation of the cellular potts model for simulation of cell-based morphogenesis. Comupter Physics Communications, 176:670–681, 2008.

13. Xu, Z., Chen, N., Kamocka, M., Malgorzata, M., Rosen, E., and M, A.: A multiscale model of thrombus development. Journal of the Royal Society Interface, 5:705–722, 2008.

14. Nagai, T. and Honda, H.: Computer simulation of wound closure in epithelial tissues: Cell–basal-lamina adhesion. Physical Review E, 80(6):061903, 2009.

15. Vitorino, P., Hammer, M., Kim, J., and Meyer, T.: A steering model of endothelial sheet migration recapitulates monolayer integrity and directed collective migration. Molecular and Cellular Biology, 31(2):342–350, 2011.

16. Basan, M., Elgeti, J., Hannezo, E., Rappel, W.-J., and Levine, H.: Alignment of cellular motility forces with tissue flow as a mechanism for efficient wound healing. Proceedings of the National Academy of Sciences, 110(7):2452–2459, 2013.

17. Newman, T.: Modeling multicellular systems using subcellular elements. Mathematical Biosciences and Engineering, 2:613–624, 2005.

18. Rejniak, K.: An immersed boundary framework for modelling the growth of individual cells: an application to the early tumour development. Journal of Theoretical Biology, 247:186–204, 2007.

19. Hutson, M. S., Veldhuis, J., Ma, X., Lynch, H. E., Cranston, P. G., and Brodland, G. W.: Combining laser microsurgery and finite element modeling to assess cell-level epithelial mechanics. Biophysical Journal, 97(12):3075–3085, 2009.

20. Vermolen, F. and Gefen, A.: Semi-stochastic cell-level computational modelling of cellular forces: application to contractures in burns and cyclic loading. Biomechanics and Modeling in Mechanobiology, 14(6):1181–1195, 2015.

21. Graner, F. and Glazier, J.: Simulation of biological cell sorting using a two-dimensional extended potts model. Physical Review Letters, 69:2013–2016, 1992.

22. Schiff, L.: Quantum Mechanics 3rd. New York: McCraw-Hill, 1968.

23. Tayllamin, B., Mendez, S., Moreno, R., Chau, M., and Nicoud, F.: Comparison of body-fitted and immersed boundary methods for biomechanical applications. In: Proceedings of the Fifth European Conference on Computational Fluid Dynamics CFD 2010, pages 1–20, 2010.

24. Vanderlei, B., Feng, J., and Edelstein-Keshet, L.: A computational model of cell polarization and motility coupling mechanics and biochemistry. Multiscale Modeling and Simulation, 9:1420–1443, 2011.

25. Brodland, G. W., Viens, D., and Veldhuis, J. H.: A new cell-based fe model for the mechanics of embryonic epithelia. Computer Methods in Biomechanics and Biomedical Engineering, 10(2):121–128, 2007.

26. Chen, X. and Brodland, G. W.: Multi-scale finite element modeling allows the mechanics of amphibian neurulation to be elucidated. Physical Biology, 5(1):015003, 2008.

27. Santoro, M. M. and Gaudino, G.: Cellular and molecular facets of keratinocyte reepithelization during wound healing. Experimental Cell Research, 304(1):274–286, 2005.

28. Larjava, H., Häkkinen, L., and Koivisto, L.: Re-epithelialization of wounds. Endodontic Topics, 24(1):59–93, 2011.

29. Zienkiewicz, O. C. and Taylor, R. L.: The finite element method: solid mechanics, volume 2. Butterworth-heinemann, 2000.

30. Oñate, E., Idelsohn, S. R., Del Pin, F., and Aubry, R.: The particle finite element methodan overview. International Journal of Computational Methods, 1(02):267–307, 2004.

31. Zhao, J., Naveed, H., Kachalo, S., Cao, Y., Tian, W., and Liang, J.: Dynamic mechanical finite element model of biological cells for studying cellular pattern formation. In Engineering in Medicine and Biology Society (EMBC), 2013 35th Annual International Conference of the IEEE, pages 4517–4520. IEEE, 2013.

32. Zhao, J., Cao, Y., DiPietro, L. A., and Liang, J.: Dynamic cellular finite element method for modeling large scale cell migration and proliferation under the control of mechanical and biochemical cues: A study of re-epithelialization. Submitted, 2016.

33. Moenning, C. and Dodgson, N. A.: Fast marching farthest point sampling for implicit surfaces and point clouds. Computer Laboratory Technical Report, 565:1–12, 2003.

34. Edelsbrunner, H.: Geometry and Topology for Mesh Generation. Cambridge Monographs on Applied and Computational Mathematics. Cambridge University Press, 2001.

35. Fung, Y.-C.: Foundations of solid mechanics. Prentice Hall, 1965.

36. Peskin, C. S.: The immersed boundary method. Acta numerica, 11:479–517, 2002.

37. Feng, K. and Shi, Z.: Mathematical Theory of Elastic Structures. Springer Berlin Heidelberg, 2013.

38. Kachalo, S., Naveed, H., Cao, Y., Zhao, J., and Liang, J.: Mechanical model of geometric cell and topological algorithm for cell dynamics from single-cell to formation of monolayered tissues with pattern. PloS ONE, 10(5):e0126484, 2015.

39. Smutny, M., Cox, H., Leerberg, J., Conti, M., and et al.: Myosin ii isoforms identify distinct functional modules that support integrity of the epithelial zonula adherens. Nature Cell Biology, 12:696–702, 2010.

40. Ananthakrishnan, R. and Ehrlicher, A.: The forces behind cell movement. International Journal of Biological Sciences, 3(5):303–317, 2007.

41. Chu, Y.-S., Thomas, W. A., Eder, O., Pincet, F., Perez, E., Thiery, J. P., and Dufour, S.: Force measurements in e-cadherin–mediated cell doublets reveal rapid adhesion strengthened by actin cytoskeleton remodeling through rac and cdc42. The Journal of Cell Biology, 167(6):1183–1194, 2004.

42. James, D. L. and Pai, D. K.: Bd-tree: output-sensitive collision detection for reduced deformable models. ACM Transactions on Graphics (TOG), 23(3):393–398, 2004.

43. Sulaiman, H. A., Othman, M., Ismail, M., Said, M., Alice, M., Ramlee, A., Misran, M., Bade, A., and Abdullah, M. H.: Distance computation using axis aligned bounding box (aabb) parallel distribution of dynamic origin point. International Conference on Microelectronics, 2013:1–6, 2013.

44. Bern, M., Eppstein, D., and Gilbert, J.: Provably good mesh generation. Journal of Computer and System Sciences, 48(3):384–409, 1994.

45. Bornstein, B. J., Keating, S. M., Jouraku, A., and Hucka, M.: Libsbml: an api library for sbml. Bioinformatics, 24(6):880–881, 2008.

46. Schultz, G. S. and Wysocki, A.: Interactions between extracellular matrix and growth factors in wound healing. Wound Repair and Regeneration, 17(2):153–162, 2009.

47. Werner, S. and Grose, R.: Regulation of wound healing by growth factors and cytokines. Physiological Reviews, 83(3):835–870, 2003.

48. Takei, T., Han, O., Ikeda, M., Male, P., Mills, I., and Sumpio, B. E.: Cyclic strain stimulates isoform-specific pkc activation and translocation in cultured human keratinocytes. Journal of Cellular Biochemistry, 67(3):327–337, 1997.

49. Sarrazy, V., Billet, F., Micallef, L., Coulomb, B., and Desmoulière, A.: Mechanisms of pathological scarring: role of myofibroblasts and current developments. Wound Repair and Regeneration, 19(s1):s10–s15, 2011.

50. Brugués, A., Anon, E., Conte, V., Veldhuis, J. H., Gupta, M., Colombelli, J., Muñoz, J. J., Brodland, G. W., Ladoux, B., and Trepat, X.: Forces driving epithelial wound healing. Nature Physics, 10(9):683–690, 2014.

51. Maruthamuthu, V., Sabass, B., Schwarz, U. S., and Gardel, M.: Cell-ecm traction force modulates endogenous tension at cell–cell contacts. Proceedings of the National Academy of Sciences, 108(12):4708–4713, 2011.

52. Tambe, D. T., Hardin, C. C., Angelini, T. E., Rajendran, K., Park, C. Y., Serra-Picamal, X., Zhou, E. H., Zaman, M. H., Butler, J. P., Weitz, D. A., et al.: Collective cell guidance by cooperative intercellular forces. Nature Materials, 10(6):469–475, 2011.

53. Monine, M. I. and Haugh, J. M.: Cell population-based model of dermal wound invasion with heterogeneous intracellular signaling properties. Cell Adhesion Migration, 2(2):137–146, 2008.

54. Ziraldo, C., Mi, Q., An, G., and Vodovotz, Y.: Computational modeling of inflammation and wound healing. Advances in Wound Care, 2(9):527–537, 2013.

55. Keren, K., Pincus, Z., Allen, G. M., Barnhart, E. L., Marriott, G., Mogilner, A., and Theriot, J. A.: Mechanism of shape determination in motile cells. Nature, 453(7194):475–480, 2008.

56. Perrone, M. C., Veldhuis, J. H., and Brodland, G. W.: Non-straight cell edges are important to invasion and engulfment as demonstrated by cell mechanics model. Biomechanics and Modeling in Mechanobiology, 15(2):405–418, 2016.

57. Chen, H. H. and Brodland, G. W.: Cell-level finite element studies of viscous cells in planar aggregates. Journal of Biomechanical Engineering, 122(4):394–401, 2000.

58. Viens, D. and Brodland, G. W.: A three-dimensional finite element model for the mechanics of cell-cell interactions. Journal of Biomechanical Engineering, 129(5):651–657, 2007.

59. Brodland, G. W., Viens, D., and Veldhuis, J. H.: A new cell-based fe model for the mechanics of embryonic epithelia. Computer Methods in Biomechanics and Biomedical Engineering, 10(2):121–128, 2007.

60. Conte, V., Ulrich, F., Baum, B., Muñoz, J., Veldhuis, J., Brodland, W., and Miodownik, M.: A biomechanical analysis of ventral furrow formation in the drosophila melanogaster embryo. PLoS One, 7(4):e34473, 2012.

61. Zielinski, R., Mihai, C., Kniss, D., and Ghadiali, S.: Finite element analysis of traction force microscopy: Influence of cell mechanics, adhesion, and morphology. Journal of Biomechanical Engineering, 135(7):071009, 2013.

62. Lulevich, V., Yang, H.-y., Rivkah, I., and Liu, G.-y.: Single cell mechanics of keratinocyte cells. Ultramicroscopy, 110(12):1435–1442, 2010.

63. Collet, J.-P., Shuman, H., Ledger, R. E., Lee, S., and Weisel, J. W.: The elasticity of an individual fibrin fiber in a clot. Proceedings of the National Academy of Sciences, 102(26):9133–9137, 2005.

64. Menon, S. N., Flegg, J. A., McCue, S. W., Schugart, R. C., Dawson, R. A., and McElwain, D. S.: Modelling the interaction of keratinocytes and fibroblasts during normal and abnormal wound healing processes. Proc. R. Soc. B., 279(1741):3329–3338, 2012.

65. Cao, Y., Naveed, H., Liang, C., and Liang, J.: Modeling spatial populaiton dynamics of stem cell lineage in wound healing and cancerogenesis. Conf Proc IEEE Eng Med Biol Soc, 2013.

66. Southgate, J., Hutton, K., Thomas, D., and Trejdosiewicz, L. K.: Normal human urothelial cells in vitro: proliferation and induction of stratification. Laboratory Investigation: A Journal of Technical Methods and Pathology, 71(4):583–594, 1994.

67. Michelson, P. H., Tigue, M., Panos, R. J., and Sporn, P. H.: Keratinocyte growth factor stimulates bronchial epithelial cell proliferation in vitro and in vivo. American Journal of Physiology-Lung Cellular and Molecular Physiology, 277(4):L737–L742, 1999.

68. Ateshian, G. A., Morrison, B., Holmes, J. W., and Hung, C. T.: Mechanics of cell growth. Mechanics Research Communications, 42:118–125, 2012.

69. Lichtner, R. B., Menrad, A., Sommer, A., Klar, U., and Schneider, M. R.: Signaling-inactive epidermal growth factor receptor/ligand complexes in intact carcinoma cells by quinazoline tyrosine kinase inhibitors. Cancer Research, 61(15):5790–5795, 2001.

70. Ning, M., Shui, M., Khan, B., Waqqar, B., Benson, B., Lacey, M., David, L., Knox, M., Susan, J., et al.: Effects of keratinocyte growth factor on the proliferation and radiation survival of human squamous cell carcinoma cell lines in vitro and in vivo. International Journal of Radiation Oncology Biology Physics, 40(1):177–187, 1998.

71. Nakazawa, K., Yashiro, M., and Hirakawa, K.: Keratinocyte growth factor produced by gastric fibroblasts specifically stimulates proliferation of cancer cells from scirrhous gastric carcinoma. Cancer Research, 63(24):8848–8852, 2003.

72. Pollard, T. D. and Borisy, G. G.: Cellular motility driven by assembly and disassembly of actin filaments. Cell, 112(4):453–465, 2003.

73. Danuser, G., Allard, J., and Mogilner, A.: Mathematical modeling of eukaryotic cell migration: Insights beyond experiments. Annual Review of Cell and Developmental Biology, 29:501–528, 2013.

74. Mogilner, A. and Oster, G.: Cell motility driven by actin polymerization. Biophysical Journal, 71(6):3030–3045, 1996.

75. Prass, M., Jacobson, K., Mogilner, A., and Radmacher, M.: Direct measurement of the lamellipodial protrusive force in a migrating cell. The Journal of Cell Biology, 174(6):767–772, 2006.

76. Salo, T., Mäkelä, M., Kylmäniemi, M., Autio-Harmainen, H., and Larjava, H.: Expression of matrix metalloproteinase-2 and-9 during early human wound healing. J. Technical Methods and Pathology, 70(2):176–182, 1994.

77. Ng, M. R., Besser, A., Danuser, G., and Brugge, J. S.: Substrate stiffness regulates cadherin-dependent collective migration through myosin-ii contractility. The Journal of Cell Biology, 199(3):545–563, 2012.

78. Safferling, K., Sütterlin, T., Westphal, K., Ernst, C., Breuhahn, K., James, M., Jäger, D., Halama, N., and Grabe, N.: Wound healing revised: a novel reepithelialization mechanism revealed by in vitro and in silico models. The Journal of Cell Biology, 203(4):691–709, 2013.

79. Laplante, A. F., Germain, L., Auger, F. A., and Moulin, V.: Mechanisms of wound reepithelialization: hints from a tissue-engineered reconstructed skin to long-standing questions. The FASEB Journal, 15(13):2377–2389, 2001.

80. Strogatz, S. H.: Nonlinear dynamics and chaos: With applications to physics, biology, chemistry and engineering. Perseus Publishing, 2006.

81. Roca-Cusachs, P., Sunyer, R., and Trepat, X.: Mechanical guidance of cell migration: lessons from chemotaxis. Current Opinion in Cell Biology, 25(5):543–549, 2013.

82. Petrie, R. J., Doyle, A. D., and Yamada, K. M.: Random versus directionally persistent cell migration. Nature Reviews Molecular Cell Biology, 10(8):538–549, 2009.

83. Cannistraro, V., Glekas, G., Rao, C., and Ordal, W.: Cellular stoichiometry of the chemotaxis proteins in bacillus subtilis. Journal of Bacteriology, 193:3220–3227, 2011.

84. Vedel, S., Tay, S., Johnston, D. M., Bruus, H., and Quake, S. R.: Migration of cells in a social context. Proceedings of the National Academy of Sciences, 110(1):129–134, 2013.

85. Kirfel, G., Rigort, A., Borm, B., Schulte, C., and Herzog, V.: Structural and compositional analysis of the keratinocyte migration track. Cell Motility and the Cytoskeleton, 55(1):1–13, 2003.

86. Gibbs, S., Silva Pinto, A. N., Murli, S., Huber, M., Hohl, D., and Ponec, M.: Epidermal growth factor and keratinocyte growth factor differentially regulate epidermal migration, growth, and differentiation. Wound Repair and Regeneration, 8(3):192–203, 2000.

87. Pasonen-Seppänen, S., Karvinen, S., Törrönen, K., Hyttinen, J. M., Jokela, T., Lammi, M. J., Tammi, M. I., and Tammi, R.: Egf upregulates, whereas tgf-β downregulates, the hyaluronan synthases has2 and has3 in organotypic keratinocyte cultures: correlations with epidermal proliferation and differentiation. Journal of Investigative Dermatology, 120(6):1038–1044, 2003.

88. Lee, S. H., Lee, J. H., and Cho, K. H.: Effects of human adipose-derived stem cells on cutaneous wound healing in nude mice. Annals of Dermatology, 23(2):150–155, 2011.

89. Garlick, J. A.: Engineering skin to study human disease–tissue models for cancer biology and wound repair. In Tissue Engineering II, pages 207–239. Springer, 2007.

90. Carmona-Fontaine, C., Matthews, H. K., Kuriyama, S., Moreno, M., Dunn, G. A., Parsons, M., Stern, C. D., and Mayor, R.: Contact inhibition of locomotion in vivo controls neural crest directional migration. Nature, 456:957–961, 2008.

91. Niewiadomska, P., Godt, D., and Tepass, U.: De-cadherin is required for intercellular motility during drosophila oogenesis. The Journal of Cell Biology, 144(3):533–547, 1999.

92. Macpherson, I., Hooper, S., Serrels, A., McGarry, L., Ozanne, B., Harrington, K., Frame, M., Sahai, E., and Brunton, V.: p120-catenin is required for the collective invasion of squamous cell carcinoma cells via a phosphorylation-independent mechanism. Oncogene, 26(36):5214–5228, 2007.

93. Shewan, A. M., Maddugoda, M., Kraemer, A., Stehbens, S. J., Verma, S., Kovacs, E. M., et al.: Myosin 2 is a key rho kinase target necessary for the local concentration of e-cadherin at cell–cell contacts. Molecular Biology of the Cell, 16(10):4531–4542, 2005.

94. Borghi, N., Sorokina, M., Shcherbakova, O. G., Weis, W. I., Pruitt, B. L., Nelson, W. J., and Dunn, A. R.: E-cadherin is under constitutive actomyosin-generated tension that is increased at cell–cell contacts upon externally applied stretch. Proceedings of the National Academy of Sciences, 109(31):12568–12573, 2012.

95. Benjamin, J. M., Kwiatkowski, A. V., Yang, C., Korobova, F., Pokutta, S., Svitkina, T., Weis, W. I., and Nelson, W. J.: αe-catenin regulates actin dynamics independently of cadherin-mediated cell–cell adhesion. The Journal of Cell Biology, 189(2):339–352, 2010.

96. Hori, K., Ding, J., Marcoux, Y., Iwashina, T., Sakurai, H., and Tredget, E. E.: Impaired cutaneous wound healing in transforming growth factor-β inducible early gene1 knockout mice. Wound Repair and Regeneration, 20(2):166–177, 2012.

97. Al-Mulla, F., Leibovich, S. J., Francis, I. M., and Bitar, M. S.: Impaired tgf-β signaling and a defect in resolution of inflammation contribute to delayed wound healing in a female rat model of type 2 diabetes. Molecular BioSystems, 7(11):3006–3020, 2011.

98. Turk, H. F., Monk, J. M., Fan, Y.-Y., Callaway, E. S., Weeks, B., and Chapkin, R. S.: Inhibitory effects of omega-3 fatty acids on injury-induced epidermal growth factor receptor transactivation contribute to delayed wound healing. American Journal of Physiology-Cell Physiology, 304(9):C905–C917, 2013.

99. Harms, B. D., Bassi, G. M., Horwitz, A. R., and Lauffenburger, D. A.: Directional persistence of egf-induced cell migration is associated with stabilization of lamellipodial protrusions. Biophysical Journal, 88(2):1479–1488, 2005.

100. Twiss, F. and de Rooij, J.: Cadherin mechanotransduction in tissue remodeling. Cellular and Molecular Life Sciences, 70(21):4101–4116, 2013.

101. Vitorino, P. and Meyer, T.: Modular control of endothelial sheet migration. Genes & Development, 22(23):3268–3281, 2008.

102. Cai, D., Chen, S.-C., Prasad, M., He, L., Wang, X., Choesmel-Cadamuro, V., Sawyer, J. K., Danuser, G., and Montell, D. J.: Mechanical feedback through e-cadherin promotes direction sensing during collective cell migration. Cell, 157(5):1146–1159, 2014.

103. Chernyavsky, A. I., Arredondo, J., Marubio, L. M., and Grando, S. A.: Differential regulation of keratinocyte chemokinesis and chemotaxis through distinct nicotinic receptor subtypes. Journal of Cell Science, 117(23):5665–5679, 2004.

104. Arwert, E. N., Hoste, E., and Watt, F. M.: Epithelial stem cells, wound healing and cancer. Nature Reviews Cancer, 12(3):170–180, 2012.

105. Epstein, F. H., Singer, A. J., and Clark, R. A.: Cutaneous wound healing. New England Journal of Medicine, 341(10):738–746, 1999.

106. Bierie, B. and Moses, H. L.: Tumour microenvironment: Tgfβ: the molecular jekyll and hyde of cancer. Nature Reviews Cancer, 6(7):506–520, 2006.

107. Quaglino Jr, D., Nanney, L., Kennedy, R., and Davidson, J.: Transforming growth factor-beta stimulates wound healing and modulates extracellular matrix gene expression in pig skin. i. excisional wound model. Laboratory Investigation; A Journal of Technical Methods and Pathology, 63(3):307–319, 1990.

108. Barrientos, S., Stojadinovic, O., Golinko, M. S., Brem, H., and Tomic-Canic, M.: Growth factors and cytokines in wound healing. Wound Repair and Regeneration, 16(5):585–601, 2008.

109. Zambruno, G., Marchisio, P. C., Marconi, A., and Vaschieri, C.: Transforming growth factor-/l modulates# 1 and/5 integrin receptors and induces the de novo expression of the ctv/36 heterodimer in normal human keratinocytes: Implications for wound healing. The Journal of Cell Biology, 129(3):853–865, 1995.

110. Sellheyer, K., Bickenbach, J. R., Rothnagel, J. A., Bundman, D., Longley, M. A., Krieg, T., Roche, N. S., Roberts, A. B., and Roop, D. R.: Inhibition of skin development by overexpression of transforming growth factor beta 1 in the epidermis of transgenic mice. Proceedings of the National Academy of Sciences, 90(11):5237–5241, 1993.

111. Wang, X.-J., Greenhalgh, D. A., Bickenbach, J. R., Jiang, A., Bundman, D. S., Krieg, T., Derynck, R., and Roop, D. R.: Expression of a dominant-negative type ii transforming growth factor β (tgf-β) receptor in the epidermis of transgenic mice blocks tgf-β-mediated growth inhibition. Proceedings of the National Academy of Sciences, 94(6):2386–2391, 1997.

112. Sherratt, J. A. and Murray, J.: Models of epidermal wound healing. Proceedings of the Royal Society of London B: Biological Sciences, 241(1300):29–36, 1990.

113. Haugh, J. M.: Deterministic model of dermal wound invasion incorporating receptor-mediated signal transduction and spatial gradient sensing. Biophysical Journal, 90(7):2297–2308, 2006.

114. Dallon, J. C., Sherratt, J. A., and Maini, P. K.: Modeling the effects of transforming growth factor-β on extracellular matrix alignment in dermal wound repair. Wound Repair and Regeneration, 9(4):278–286, 2001.

115. Cumming, B. D., McElwain, D., and Upton, Z.: A mathematical model of wound healing and subsequent scarring. Journal of the Royal Society Interface, 7(42):19–34, 2010.

116. Murphy, K. E., McCue, S. W., and McElwain, D.: Clinical strategies for the alleviation of contractures from a predictive mathematical model of dermal repair. Wound Repair and Regeneration, 20(2):194–202, 2012.

117. Nagai, T., Kawasaki, K., and Nakamura, K.: Vertex dynamics of two-dimensional cellular patterns. Journal of the Physical Society of Japan, 57(7):2221–2224, 1988.

118. Farhadifar, R., Röper, J.-C., Aigouy, B., Eaton, S., and Jülicher, F.: The influence of cell mechanics, cell-cell interactions, and proliferation on epithelial packing. Current Biology, 17(24):2095–2104, 2007.

119. Nagai, T. and Honda, H.: Wound healing mechanism in epithelial tissues cell adhesion to basal lamina. WSEAS Transactions on Biology and Biomedicine, 6(3):111–116, 2006.

120. Fletcher, A. G., Osborne, J. M., Maini, P. K., and Gavaghan, D. J.: Implementing vertex dynamics models of cell populations in biology within a consistent computational framework. Progress in Biophysics and Molecular Biology, 113(2):299–326, 2013.

121. Marée, A. F., Grieneisen, V. A., and Hogeweg, P.: The cellular potts model and biophysical properties of cells, tissues and morphogenesis. In Single-cell-based models in biology and medicine, pages 107–136. Springer, 2007.

122. Merks, R. M., Perryn, E. D., Shirinifard, A., and Glazier, J. A.: Contact-inhibited chemotaxis in de novo and sprouting blood-vessel growth. PLoS Computational Biology, 4(9):e1000163, 2008.

123. Honda, H., Tanemura, M., and Yoshida, A.: Differentiation of wing epidermal scale cells in a butterfly under the lateral inhibition model-appearance of large cells in a polygonal pattern. Acta Biotheoretica, 48(2):121–136, 2000.

124. Murphy, G. and Gavrilovic, J.: Proteolysis and cell migration: creating a path? Current Opinion in Cell Biology, 11(5):614–621, 1999.

125. Page-McCaw, A., Ewald, A. J., and Werb, Z.: Matrix metalloproteinases and the regulation of tissue remodelling. Nature Reviews Molecular Cell Biology, 8(3):221–233, 2007.

126. Furuse, M., Hata, M., Furuse, K., Yoshida, Y., Haratake, A., Sugitani, Y., Noda, T., Kubo, A., and Tsukita, S.: Claudin-based tight junctions are crucial for the mammalian epidermal barrier a lesson from claudin-1–deficient mice. The Journal of Cell Biology, 156(6):1099–1111, 2002.

127. O'Toole, E.: Extracellular matrix and keratinocyte migration. Clinical and Experimental Dermatology, 26(6):525–530, 2001.

128. Steffensen, B., Häkkinen, L., and Larjava, H.: Proteolytic events of wound healing coordinated interactions among matrix metalloproteinases (mmps), integrins, and extracellular matrix molecules. Critical Reviews in Oral Biology & Medicine, 12(5):373–398, 2001.

129. Barrandon, Y. and Green, H.: Cell size as a determinant of the clone-forming ability of human keratinocytes. Proceedings of the National Academy of Sciences, 82(16):5390–5394, 1985.

130. Watt, F. M., Jordan, P. W., and O'Neill, C. H.: Cell shape controls terminal differentiation of human epidermal keratinocytes. Proceedings of the National Academy of Sciences, 85(15):5576–5580, 1988.

131. Li, W., Fan, J., Chen, M., Guan, S., Sawcer, D., Bokoch, G. M., and Woodley, D. T.: Mechanism of human dermal fibroblast migration driven by type i collagen and platelet-derived growth factor-bb. Molecular Biology of the Cell, 15(1):294–309, 2004.

132. Yu, Q. and Stamenkovic, I.: Cell surface-localized matrix metalloproteinase-9 proteolytically activates tgf-β and promotes tumor invasion and angiogenesis. Genes & Development, 14(2):163–176, 2000.

133. Clark, R., Nielsen, L. D., Welch, M. P., and McPherson, J. M.: Collagen matrices attenuate the collagen-synthetic response of cultured fibroblasts to tgf-beta. Journal of Cell Science, 108(3):1251–1261, 1995.

134. Albro, M. B., Nims, R. J., Cigan, A. D., Yeroushalmi, K. J., Alliston, T., Hung, C. T., and Ateshian, G. A.: Accumulation of exogenous activated tgf-β in the superficial zone of articular cartilage. Biophysical Journal, 104(8):1794–1804, 2013.

135. Chen, L., Arbieva, Z. H., Guo, S., Marucha, P. T., Mustoe, T. A., and DiPietro, L. A.: Positional differences in the wound transcriptome of skin and oral mucosa. BMC Genomics, 11(471):1–15, 2010.

136. Heldin, C.-H., Miyazono, K., and Ten Dijke, P.: Tgf-β signalling from cell membrane to nucleus through smad proteins. Nature, 390(6659):465–471, 1997.

137. Shi, Y. and Massagué, J.: Mechanisms of tgf-β signaling from cell membrane to the nucleus. Cell, 113(6):685–700, 2003.

138. Chan, J. R., Blumenschein, W., Murphy, E., Diveu, C., Wiekowski, M., Abbondanzo, S., Lucian, L., Geissler, R., Brodie, S., Kimball, A. B., et al.: Il-23 stimulates epidermal hyperplasia via tnf and il-20r2–dependent mechanisms with implications for psoriasis pathogenesis. The Journal of Experimental Medicine, 203(12):2577–2587, 2006.

139. Colwell, A. S., Phan, T.-T., Kong, W., Longaker, M. T., and Lorenz, P. H.: Hypertrophic scar fibroblasts have increased connective tissue growth factor expression after transforming growth factor-β stimulation. Plastic and Reconstructive Surgery, 116(5):1387–1390, 2005.

140. Guilak, F., Cohen, D. M., Estes, B. T., Gimble, J. M., Liedtke, W., and Chen, C. S.: Control of stem cell fate by physical interactions with the extracellular matrix. Cell Stem Cell, 5(1):17–26, 2009.

141. Rape, A. D., Guo, W.-h., and Wang, Y.-l.: The regulation of traction force in relation to cell shape and focal adhesions. Biomaterials, 32(8):2043–2051, 2011.

142. Nikkhah, M., Edalat, F., Manoucheri, S., and Khademhosseini, A.: Engineering microscale topographies to control the cell–substrate interface. Biomaterials, 33(21):5230–5246, 2012.

143. Wehrle-Haller, B.: Structure and function of focal adhesions. Current Opinion in Cell Biology, 24(1):116–124, 2012.

144. Carisey, A. and Ballestrem, C.: Vinculin, an adapter protein in control of cell adhesion signalling. European Journal of Cell Biology, 90(2):157–163, 2011.

145. Gardel, M. L., Schneider, I. C., Aratyn-Schaus, Y., and Waterman, C. M.: Mechanical integration of actin and adhesion dynamics in cell migration. Annual Review of Cell and Developmental Biology, 26:315–333, 2010.

146. Chen, C. S., Alonso, J. L., Ostuni, E., Whitesides, G. M., and Ingber, D. E.: Cell shape provides global control of focal adhesion assembly. Biochemical and Biophysical Research Communications, 307(2):355–361, 2003.

147. Théry, M., Racine, V., Piel, M., Pépin, A., Dimitrov, A., Chen, Y., Sibarita, J.-B., and Bornens, M.: Anisotropy of cell adhesive microenvironment governs cell internal organization and orientation of polarity. Proceedings of the National Academy of Sciences, 103(52):19771–19776, 2006.

148. Sheets, K., Wunsch, S., Ng, C., and Nain, A. S.: Shape-dependent cell migration and focal adhesion organization on suspended and aligned nanofiber scaffolds. Acta biomaterialia, 9(7):7169–7177, 2013.

149. Watt, F. M. and Huck, W. T.: Role of the extracellular matrix in regulating stem cell fate. Nature Reviews Molecular Cell Biology, 14(8):467–473, 2013.

150. Leong, C., Vedula, S., Lim, C., and Ladoux, B.: Geometrical constraints and physical crowding direct collective migration of fibroblasts. Communicative & Integrative Biology, 6(2):e23197, 2013.

151. Liu, W. F. and Chen, C. S.: Cellular and multicellular form and function. Advanced Drug Delivery Reviews, 59(13):1319–1328, 2007.

152. Park, S., Koch, D., Cardenas, R., Käs, J., and Shih, C.: Cell motility and local viscoelasticity of fibroblasts. Biophysical Journal, 89(6):4330–4342, 2005.

153. Rubinstein, B., Fournier, M. F., Jacobson, K., Verkhovsky, A. B., and Mogilner, A.: Actin-myosin viscoelastic flow in the keratocyte lamellipod. Biophysical Journal, 97(7):1853–1863, 2009.

154. Ladoux, B., Mège, R.-M., and Trepat, X.: Front–rear polarization by mechanical cues: From single cells to tissues. Trends in Cell Biology, 26(6):420–433, 2016.

155. Dokukina, I. V. and Gracheva, M. E.: A model of fibroblast motility on substrates with different rigidities. Biophysical Journal, 98(12):2794–2803, 2010.

156. Barnhart, E., Lee, K.-C., Keren, K., Mogilner, A., and Theriot, J.: An adhesion-dependent switch between mechanisms that determine motile cell shape. PLoS Biol, 9(5):e1001059, 2011.

157. Schoner, J. L., Lang, J., and Seidel, H.-P.: Measurement-based interactive simulation of viscoelastic solids. In Computer Graphics Forum, volume 23, pages 547–556. Wiley Online Library, 2004.

158. Schwartz, J.-M., Denninger, M., Rancourt, D., Moisan, C., and Laurendeau, D.: Modelling liver tissue properties using a non-linear visco-elastic model for surgery simulation. Medical Image Analysis, 9(2):103–112, 2005.

159. Oakes, P. W., Banerjee, S., Marchetti, M. C., and Gardel, M. L.: Geometry regulates traction stresses in adherent cells. Biophysical Journal, 107(4):825–833, 2014.

160. Banerjee, S. and Marchetti, M. C.: Contractile stresses in cohesive cell layers on finite-thickness substrates. Physical Review Letters, 109(10):108101, 2012.

161. Ridley, A. J., Schwartz, M. A., Burridge, K., Firtel, R. A., Ginsberg, M. H., Borisy, G., Parsons, J. T., and Horwitz, A. R.: Cell migration: integrating signals from front to back. Science, 302(5651):1704–1709, 2003.

162. Gallant, N. D., Michael, K. E., and García, A. J.: Cell adhesion strengthening: contributions of adhesive area, integrin binding, and focal adhesion assembly. Molecular Biology of the Cell, 16(9):4329–4340, 2005.

163. DiMilla, P., Barbee, K., and Lauffenburger, D.: Mathematical model for the effects of adhesion and mechanics on cell migration speed. Biophysical Journal, 60(1):15–37, 1991.

164. Bell, G. I.: Models for the specific adhesion of cells to cells. Science, 200(4342):618–627, 1978.

165. Prager-Khoutorsky, M., Lichtenstein, A., Krishnan, R., Rajendran, K., Mayo, A., Kam, Z., Geiger, B., and Bershadsky, A. D.: Fibroblast polarization is a matrix-rigidity-dependent process controlled by focal adhesion mechanosensing. Nature Cell Biology, 13(12):1457–1465, 2011.

166. Stéphanou, A., Mylona, E., Chaplain, M., and Tracqui, P.: A computational model of cell migration coupling the growth of focal adhesions with oscillatory cell protrusions. Journal of Theoretical Biology, 253(4):701–716, 2008.

167. Rozbicki, E., Chuai, M., Karjalainen, A. I., Song, F., Sang, H. M., Martin, R., Knölker, H.-J., MacDonald, M. P., and Weijer, C. J.: Myosin-ii-mediated cell shape changes and cell intercalation contribute to primitive streak formation. Nature Cell Biology, 17(4):397–408, 2015.

168. Pasapera, A. M., Schneider, I. C., Rericha, E., Schlaepfer, D. D., and Waterman, C. M.: Myosin ii activity regulates vinculin recruitment to focal adhesions through fak-mediated paxillin phosphorylation. The Journal of Cell Biology, 188(6):877–890, 2010.

169. Geiger, B. and Yamada, K. M.: Molecular architecture and function of matrix adhesions. Cold Spring Harbor Perspectives in Biology, 3(5):a005033, 2011.

170. Rees, R. W., Ralph, D. J., Royle, M., Moncada, S., and Cellek, S.: Y-27632, an inhibitor of rho-kinase, antagonizes noradrenergic contractions in the rabbit and human penile corpus cavernosum. British Journal of Pharmacology, 133(4):455–458, 2001.

171. Bischofs, I., Safran, S., and Schwarz, U.: Elastic interactions of active cells with soft materials. Physical Review E, 69(2):021911, 2004.

172. Sedef, M., Samur, E., and Basdogan, C.: Real-time finite-element simulation of linear viscoelastic tissue behavior based on experimental data. Computer Graphics and Applications, IEEE, 26(6):58–68, 2006.

173. Wottawah, F., Schinkinger, S., Lincoln, B., Ananthakrishnan, R., Romeyke, M., Guck, J., and Käs, J.: Optical rheology of biological cells. Physical Review Letters, 94(9):098103, 2005.

174. Varani, J., Perone, P., Deming, M. O., Warner, R. L., Aslam, M. N., Bhagavathula, N., Dame, M. K., and Voorhees, J. J.: Impaired keratinocyte function on ma-

trix metalloproteinase-1 (mmp-1) damaged collagen. Arch. Dermatological Res., 301(7):497–506, 2009.

175. Nickoloff, B., Mitra, R., Riser, B., Dixit, V., and Varani, J.: Modulation of keratinocyte motility. correlation with production of extracellular matrix molecules in response to growth promoting and antiproliferative factors. Am. J. Pathol., 132(3):543–551, 1988.

176. Watt, F. M. and Green, H.: Involucrin synthesis is correlated with cell size in human epidermal cultures. The Journal of Cell Biology, 90(3):738–742, 1981.

177. Cooper, G. and Hausman, R.: The Cell: A Molecular Approach. ASM Press, 2004.

178. Tozluoğlu, M., Tournier, A. L., Jenkins, R. P., Hooper, S., Bates, P. A., and Sahai, E.: Matrix geometry determines optimal cancer cell migration strategy and modulates response to interventions. Nature Cell Biology, 15(7):751–762, 2013.

179. Bader, R. A., Herzog, K. T., and Kao, W. J.: A study of diffusion in poly (ethyleneglycol)-gelatin based semi-interpenetrating networks for use in wound healing. Polymer Bulletin, 62(3):381–389, 2009.

180. Thorne, R. G., Hrabětová, S., and Nicholson, C.: Diffusion of epidermal growth factor in rat brain extracellular space measured by integrative optical imaging. Journal of Neurophysiology, 92(6):3471–3481, 2004.

181. Murphy, K. E., Hall, C. L., Maini, P. K., McCue, S. W., and McElwain, D. S.: A fibrocontractive mechanochemical model of dermal wound closure incorporating realistic growth factor kinetics. Bulletin of Mathematical Biology, 74(5):1143–1170, 2012.

182. GRØN, B., Stoltze, K., Andersson, A., and Dabelsteen, E.: Oral fibroblasts produce more hgf and kgf than skin fibroblasts in response to co-culture with keratinocytes. Apmis, 110(12):892–898, 2002.

183. Kurobe, M., Furukawa, S., and Hayashi, K.: Synthesis and secretion of an epidermal growth factor (egf) by human fibroblast cells in culture. Biochemical and Biophysical Research Communications, 131(3):1080–1085, 1985.

184. Wang, R., Ghahary, A., Shen, Q., Scott, P. G., Roy, K., and Tredget, E. E.: Hypertrophic scar tissues and fibroblasts produce more transforming growth factor-β1 mrna and

protein than normal skin and cells. Wound Repair and Regeneration, 8(2):128–137, 2000.

185. Payne, W., Wright, T., Ko, F., Wheeler, C., Wang, X., and Robson, M.: Bacterial degradation of growth factors. J Appl Res, 3:35–40, 2003.

186. Brown, K. D., Friedkin, M., and Rozengurt, E.: Colchicine inhibits epidermal growth factor degradation in 3t3 cells. Proceedings of the National Academy of Sciences, 77(1):480–484, 1980.

187. Yang, L., Qiu, C. X., Ludlow, A., Ferguson, M. W., and Brunner, G.: Active transforming growth factor-β in wound repair: determination using a new assay. The American Journal of Pathology, 154(1):105–111, 1999.

188. Lauffenburger, D. A. and Horwitz, A. F.: Cell migration: a physically integrated molecular process. Cell, 84(3):359–369, 1996.

189. Ibaraki, N., Lin, L.-R., and Reddy, V. N.: Effects of growth factors on proliferation and differentiation in human lens epithelial cells in early subculture. Investigative Ophthalmology & Visual Science, 36(11):2304–2312, 1995.

190. Hebert, T. L., Wu, X., Yu, G., Goh, B. C., Halvorsen, Y.-D. C., Wang, Z., Moro, C., and Gimble, J. M.: Culture effects of epidermal growth factor (egf) and basic fibroblast growth factor (bfgf) on cryopreserved human adipose-derived stromal/stem cell proliferation and adipogenesis. Journal of Tissue Engineering and Regenerative Medicine, 3(7):553–561, 2009.

191. Berdyyeva, T. K., Woodworth, C. D., and Sokolov, I.: Human epithelial cells increase their rigidity with ageing in vitro: direct measurements. Physics in Medicine and Biology, 50(1):81–92, 2005.

192. Haga, H., Sasaki, S., Kawabata, K., Ito, E., Ushiki, T., and Sambongi, T.: Elasticity mapping of living fibroblasts by afm and immunofluorescence observation of the cytoskeleton. Ultramicroscopy, 82(1):253–258, 2000.

193. Petrie, R. J., Gavara, N., Chadwick, R. S., and Yamada, K. M.: Nonpolarized signaling reveals two distinct modes of 3d cell migration. The Journal of Cell Biology, 197(3):439–455, 2012.

194. Achterberg, V. F., Buscemi, L., Diekmann, H., Smith-Clerc, J., Schwengler, H., Meister, J.-J., Wenck, H., Gallinat, S., and Hinz, B.: The nano-scale mechanical properties of the extracellular matrix regulate dermal fibroblast function. Journal of Investigative Dermatology, 134(7):1862–1872, 2014.

195. Wearing, H. J. and Sherratt, J. A.: Keratinocyte growth factor signalling: a mathematical model of dermal–epidermal interaction in epidermal wound healing. Mathematical Biosciences, 165(1):41–62, 2000.

196. Thoumine, O. and Ott, A.: Time scale dependent viscoelastic and contractile regimes in fibroblasts probed by microplate manipulation. Journal of Cell Science, 110(17):2109–2116, 1997.

VITA

NAME: Jieling Zhao

EDUCATION:

- B.S., Applied Mathematics, Beijing Normal University, Beijing, China, 2008
- Ph.D., Bioinformatics, University of Illinois at Chicago, Chicago, Illinois, 2016

RESEARCH EXPERIENCE

- Research Assistant, Advisor: Dr. Jie Liang, Department of Bioengineering, University of Illinois at Chicago, 2009–2016
  - **Wound healing**: Develop the dynamic cellular finite element model (dyCelFEM) to study the effects of biochemical and mechanical signals on spatio-temporal pattern of skin wound healing.
  - **Cell-ECM communication**: Apply dyCelFEM to investigate the mechanical and geometric properties of ECM on regulating cell migration and elongation.
  - **Functional pocket of enzyme**: Apply homologous model and computational geometry model to study the accuracy of recapture of functional pocket of comparative enzyme structure.

PUBLICATION

- **Jieling Zhao**, Youfang Cao, Luisa A. DiPietro, Jie Liang, Dynamic cellular finite element method for modeling large scale cell migraiton and proliferation under the control of

mechanical and biochemical cues: A study of re-epithelialization, 2016, Submitted to Journal of Royal Society Interface.

- Sema Kachalo, Hammad Naveed, Youfang Cao, **Jieling Zhao**, Jie Liang, Mechanical Model of Geometric Cell and Topological Algorithm for Cell Dynamics from Single-Cell to Formation of Monolayered Tissues with Pattern, 2015, PLoS ONE, 10(5): e0126484.
- Sara Camp, Ermelindo Ceco, Carrie Evenoski, Sergei Danilov, Tong Zhou, Eddie Chiang, Liliana Moreno, Brandon Mapes, **Jieling Zhao**, Gamze Gursoy, Mary Brown, Djanybek Adyshev, Shahid Siddiqui, Hector Quijada, Saad Sammani, Eleftheria Letsiou, Laleh Saadat, Mohammed Yousef, Ting Wang, Jie Liang, Joe Garcia, Unique toll-like receptor 4 activation by NAMPT/PBEF induces NFκB signaling and inflammatory lung injury, 2015, Sci. Rep., 5: 13135.
- **Jieling Zhao**, Hammad Naveed, Sema Kachalo, Youfang Cao, Jie Liang, Dynamic mechanical finite element model of biological cells for studying cellular pattern formation, 2013, Conf. Proc. IEEE Eng. Med. Biol. Soc., 4517-4520.
- **Jieling Zhao**, Joe Dundas, Sema Kachalo, Zheng Ouyang, Jie Liang, Accuracy of functional surfaces on comparatively modeled protein structures, 2011, J. Struc. Func. Genom., 12(2):97-107.